THE UNIVERSITY *of* EDINBURGH

This thesis has been submitted in fulfilment of the requirements for a postgraduate degree (e.g. PhD, MPhil, DClinPsychol) at the University of Edinburgh. Please note the following terms and conditions of use:

This work is protected by copyright and other intellectual property rights, which are retained by the thesis author, unless otherwise stated.
A copy can be downloaded for personal non-commercial research or study, without prior permission or charge.
This thesis cannot be reproduced or quoted extensively from without first obtaining permission in writing from the author.
The content must not be changed in any way or sold commercially in any format or medium without the formal permission of the author.
When referring to this work, full bibliographic details including the author, title, awarding institution and date of the thesis must be given.

IRCI-Free MIMO SAR

Mohammed A. AlShaya

A thesis submitted for the degree of Doctor of Philosophy.
The University of Edinburgh.
2020

Abstract

This thesis presents new configurations that (i) utilise the available bandwidth to the maximum efficiency in multiple subband multiple-input multiple-output (MIMO) synthetic aperture radar (SAR) and (ii) employ all of the phase centres in orthogonal waveform encoding MIMO SAR. These configurations enable us to image a wider swath with a higher cross-range resolution compared to the conventional orthogonal waveform encoding MIMO SAR. Two different multiple subband MIMO SAR configurations are proposed. The first one makes use of multiple contiguous narrow receiving beams with different phase centres which permits the use of a pulse repetition frequency (PRF) lower than the total Doppler bandwidth. Echoes corresponding to different transmitted subband waveforms are processed jointly without separating them at the receiver using a bank of bandpass filers (BPFs) to utilise the bandwidth to the maximum efficiency (i.e. there is no need to add guard bands between the adjacent subband spectra). Digital beamforming (DBF) on receive in elevation is proposed to mitigate the effect of interbeams overlapping on the azimuth ambiguity characteristics. The second proposed multiple subband MIMO SAR configuration has an advantage over the first in that the beamwidths of all transmitters and receivers are the same. The beams simultaneously illuminate the same imaging area which overcome the receiving interbeams overlapping problem without employing DBF on receive in elevation. This reduces the implementation complexity. The proposed orthogonal waveform encoding MIMO SAR configuration employs multiple contiguous azimuth beams. It uses all of the phase centres including the spatially overlapping ones to reduce the minimum operating PRF that should be satisfied to avoid aliasing in the azimuth dimension. The received signals in all proposed configurations are processed as the solution to system identification problems using the principle of displaced phase centres (DPC). This, in turn, facilitates the use of linear frequency modulated (LFM) waveforms for transmission and, hence, gains all the inherent benefits of these waveforms. The impulse response in the range dimension is identified using a proposed frequency domain system identification (FDSI) estimation algorithm instead of a matched filter. The length of the transmitted waveform is not a function of the channel impulse response length in the range dimension which makes the proposed algorithm suitable for a stripmap SAR application. The estimated range profile obtained using the FDSI-based algorithm has ideally a zero sidelobes level which is the property interrange cell interference (IRCI) free.

Lay Abstract

Synthetic aperture radar (SAR) imaging such as TerraSar-X has an advantage over the optical instrument in a way that it can form the image regardless of the weather conditions (i.e. during night and cloudy weather). It has many potential applications in remote sensing (i.e. climate change monitoring) and mapping the surfaces of planets from the satellites. In this thesis, different SAR configurations are proposed in a way that multiple transmitters and receivers are better utilised to improve the resolution of the formed image.

Declaration of originality

I hereby declare that the research recorded in this thesis and the thesis itself was composed and originated entirely by myself in the institute for digital communications (IDCOM) at the school of engineering at the University of Edinburgh.

Mohammed A. AlShaya , July 2020

Acknowledgements

I would like first to express my gratitude to my supervisor, Professor Bernie Mulgrew who guided me along my PhD journey. In addition, I would like to express my warm gratitude to Dr Mehrdad Yaghoobi for his useful suggestions and constructive discussions. Finally and most importantly, my sincere gratitude is given to my parents and my wife, Aljohara, for their constant support and encouragement.

Contents

List of figures

List of tables

Abbreviations and Notation

Abbreviations and acronyms

SAR	Synthetic aperture radar
IRCI	Interrange cell interference
SISO	Single-input single-output
SIMO	Single-input multiple-output
MIMO	multiple-input multiple-output
BPF	Bandpass filter
PRF	Pulse repetition frequency
LFM	Linear frequency modulated
FDSI	Frequency domain system identification
MISO	Multiple-input single-output
DPC	Displaced phase centre
PRI	Pulse repetition interval
CW	Continuous wave
FMCW	Frequency modulated continuous wave
SRP	Sweep repetition period
MTD	Moving target detection
AoA	Angle of arrival
AoD	Angle of departure
PARP	Peak to average power ratio
DBF	Digital beamforming
ISAR	Inverse synthetic aperture radar
LPF	Lowpass filter
ADC	analogue to digital converter
FFT	Fast Fourier transform
LO	Local oscillator
SNR	Signal to noise ratio
PSF	Point spread function
CP	Cyclic prefix

OFDM	Orthogonal frequency division multiplexing
RCS	Radar cross-section
DFT	Discrete Fourier transform
SPCMB	Single-phase centre multiple beam
DPCMB	Displaced phase centre multiple beam
SPCT-DPCR	Single phase centre on transmit and displaced phase centre on receive
WTNR	Wide-transmit narrow-receive
NTNR	Narrow-transmit narrow-receive
HRWS	High resolution wide swath
GMTI	Ground moving target indication
STAP	Space-time adapted processing
TDMA	Time division multiple access
CDMA	Code division multiple access
FDMA	Frequency division multiple access
RCMC	Range cell migration correction
AASR	Azimuth ambiguity to signal ratio
IBS	Interbeams suppression
MF	Matched filter
EPC	Effective phase centre
LCMV	Linearly constrained minimum variance
RD	Range-Doppler
STSOW	Short-term shift orthogonal waveforms

Notation

a/A	Upper and lower case mathtype letters denote a scaler
$\mathbf{a}$	bold lower case mathtype letters denote a vector
$\mathbf{A}$	bold upper case mathtype letters denote a matrix
$\mathbf{A}^N$	A matrix of dimension $N \times 1$
$\mathcal{R}$	Set of real numbers
$< A >_n$	A modulo n
$(.)^T$	Transpose operator
$(.)^H$	Hermitian operator
$\mathrm{E}(.)$	Expectation operator
$\hat{(.)}$	Estimated value
$\mathrm{diag}(\mathbf{a})$	A matrix with the vector $\mathbf{a}$ as the main diagonal
$\mathcal{C}$	The field of complex numbers
f	Frequency in Hz
$\mathbf{F}$	Discrete Fourier transform matrix
F_c	Carrier frequency in Hz
t	Slow time
η	Fast time
$x(t)$	Transmitted waveform
$y(t)$	Received signal
h	The channel impulse response
τ	Delay
$w_n(t)$	Additive white noise at the $n\mathrm{th}$ receiver
M	Number of transmit antennas
N	Number of receive antennas
$a(\theta)$	Array manifold vector
B_d	Doppler bandwidth

Chapter 1
Introduction

1.1 Problem Description and Motivation

Synthetic aperture radar (SAR) imaging is used to obtain a reflectivity map of a particular scene [1]. It has the advantage over the optical instrument in that it can construct the image (i.e. reflectivity map) regardless of the weather conditions. The range profile, which is the impulse response along the direction of the antenna boresight, in SAR consists of a large number of scattering points. Therefore, the estimated range profile is required to be of a high range resolution with low sidelobe levels so that scattering points with a low reflectivity are not masked by bright scattering points. Interrange cell interference (IRCI) is a term used in the literature [2] [3] [4] to describe the sidelobes effects of a scattering point on the adjacent range cells which increases proportionally with the number of range cells [2].

Conventional single-input single-output (SISO) SAR involves a tradeoff between obtaining the desired wide swath width and high cross-range resolution. As a result, single-input multiple-output (SIMO) SAR and multiple-input multiple-output (MIMO) SAR are proposed in the literature [5][6][7] to resolve this contradicting requirement. Two different types of MIMO SAR are considered in the thesis, namely, multiple subband MIMO SAR and orthogonal waveform encoding MIMO SAR.

According to the literature [8] [9], most of the multiple subband MIMO SAR algorithms employ a bank of bandpass filters (BPFs) to separate the echoes corresponding to each transmitted subband waveform. The leakage among the spectra of the transmitted subband waveforms degrades the performance of the estimated range profile. Accordingly, a guard band must be added between the spectra of the adjacent subband waveforms which affects the bandwidth utilisation efficiency.

Orthogonal waveform encoding MIMO SAR simultaneously emits multiple orthogonal waveforms into the area to be imaged and the echoes due to the different transmitted waveforms can be separated at the receiver by employing different matched filters. This can be used, with

further processing, to reduce the minimum pulse repetition frequency (PRF) required to avoid aliasing in the azimuth dimension. This is due to the extra phase centres introduced by the use of multiple transmitters along with multiple receiving channels. The phase centres in the conventional orthogonal waveform encoding MIMO SAR, for the case that the same antenna arrays are used for transmission and reception, are not fully exploited because the spatially overlapped ones carry the same information (i.e. share the same Doppler bandwidth) [10].

Recently, there has been a considerable interest in remote sensing to enhance the high resolution wide swath (HRWS) imaging capacity of SAR systems [11] [12]. Therefore, it is aimed in this thesis to address and minimise the effects of the IRCI in the formed SAR image, fully utilise the bandwidth in multiple subband MIMO SAR to maximum efficiency and more effectively use the phase centres introduced by orthogonal waveform encoding MIMO SAR.

1.2 Organisation

The thesis covers two different types of MIMO SAR, namely, multiple subband MIMO SAR (Chapter 3, Chapter 4 and Chapter 5) and orthogonal waveform encoding MIMO SAR (Chapter 6). The following provides a brief description of the chapters:

Chapter 2 provides the literature review and principles needed for the rest of the chapters. It addresses the main challenge of the conventional SISO SAR, which is the contradicting requirement between obtaining the desired wide swath and high cross-range resolution and how SIMO SAR and MIMO SAR configurations are utilised to overcome such tradeoff. In addition, a brief description of different types of SIMO SAR and MIMO SAR is provided. Different techniques of range profile estimation are described and the relative weaknesses and strengths are discussed in the context of SAR imaging applications. Finally, a preliminary study on system identification formulation of MIMO radar is provided. The results of this study were published in [13].

Chapter 3 presents the first technical chapter in which a bandpass filters based multiple subband MIMO SAR is proposed. Two SAR modes of operation are considered, namely, stripmap SAR and sliding spotlight SAR. In this chapter, the received signals of the MIMO SAR is formulated as system identification problems which is then used to estimate the impulse response in the range dimension using the proposed FDSI-based estimation algorithm. Moreover, the resulted azimuth ambiguity from using a PRF lower than the Doppler bandwidth is removed using a set

of spatial filters and azimuth deramping for the case of sliding spotlight SAR. The results of this chapter were published in [14] and [15].

Chapter 4 is the second technical chapter in which a new multiple subband IRCI-free MIMO SAR configuration is proposed to obtain an HRWS imaging. The beams of the transmitters in the proposed configuration are wide and multiple contiguous receiving subbeams with different phase centres and squint angles are utilised in the azimuth direction. In addition, the synthesis of wide transmitting beams from a narrow antenna beam is described in order to attain the desired SNR and use the same antenna for transmission and reception. The proposed configuration is IRCI-free although no guard bands are added between the adjacent spectra of transmitting subband waveforms which allows us to utilise the available bandwidth to maximum efficiency. The length of the waveform is not a function of the channel impulse response length in the range dimension, which makes the proposed configuration suitable for stripmap mode of operation. Moreover, the azimuth ambiguity characteristics of the proposed configuration is analysed and digital beamforming (DBF) on receive in elevation is proposed in order to mitigate the effect of interbeams overlapping. Finally, a PRF lower than the total Doppler bandwidth is used to obtain an HRWS imaging without experiencing azimuth ambiguities. It is due to the multiple narrow azimuth beams formed on receiving. The results of this chapter were published in [16] and [17].

Chapter 5 is the third technical chapter in which the multiple subband MIMO SAR configuration proposed in Chapter 4 is extended in a way that the beamwidths of the transmitters and receivers are the same and they simultaneously illuminate the same imaging area which overcomes the receiving interbeams overlapping without the need of DBF on receive in elevation. In addition, echoes corresponding to all transmitted subband waveforms are processed jointly at the receiver without separating them using a bank of BPFs. This allows the utilisation of the available bandwidth to maximum efficiency. A PRF lower than the Doppler bandwidth is used to obtain an HRWS imaging and the resulted azimuth ambiguities are removed using a set of spatial filters applied on the received signals formulated as MISO system identification problems. The results of this chapter were submitted in [18].

Chapter 6 presents the fourth technical chapter in which a new orthogonal waveform encoding MIMO SAR is proposed to map wider image swaths with higher cross-range resolution as compared with the conventional MIMO SAR. The proposed configuration utilises all the phase centres including the spatially overlapping ones which allows to use a lower operating PRF

as compared to the conventional MIMO SAR. It is due to the multiple contiguous azimuth beams which makes the echoes, whose effective phase centres are overlapped, occupy different Doppler bandwidths. The waveforms used for transmission consist of a sequence of LFM waveforms which share the same bandwidth and have the same centre frequency. The estimated range profile is free from interrange cell interference (IRCI) which is a result of using an FDSI-based estimation algorithm instead of matched filters. Echoes corresponding to different phase centres are separated at the receiver using DBF on receive in elevation. The results of this chapter are published in [19] and [20].

Finally, the thesis is concluded in Chapter 7. In addition, possible future work is discussed.

1.3 Publications

Conference Papers:

- M. AlShaya, M. Yaghoobi and B. Mulgrew, "Frequency Domain System Identification for High Resolution IRCI-Free Collocated MIMO Radar," *2018 15th European Radar Conference (EuRAD)*, Madrid, 2018, pp. 134-137.

- M. AlShaya, M. Yaghoobi and B. Mulgrew, "Frequency Domain System Identification for Wide Swath High Resolution IRCI-Free MIMO SAR," *2019 IEEE Radar Conference (RadarConf)*, Boston, MA, USA, 2019, pp. 1-6.

- M. AlShaya, M. Yaghoobi and B. Mulgrew, "Stepped Frequency IRCI-Free Sliding Spotlight MIMO SAR," *2019 16th European Radar Conference (EuRAD)*, PARIS, France, 2019, pp. 73-76.

- M. AlShaya, M. Yaghoobi, and B. Mulgrew, "Multiple-Beam IRCI-Free MIMO SAR," in *Proc. Int. Radar Conf. (RADAR)*, Toulon, France, 2019.

- M. AlShaya, M. Yaghoobi, and B. Mulgrew, "Resolution Enhancement in High Resolution Wide Swath MIMO SAR," in *2020 IEEE International Radar Conference*, Washington DC, 2020.

Journal Papers:

- M. AlShaya, M. Yaghoobi and B. Mulgrew, "High-Resolution Wide-Swath IRCI-Free MIMO SAR," in *IEEE Transactions on Geoscience and Remote Sensing*, vol. 58, no. 1, pp. 713-725, Jan. 2020.
- M. AlShaya, M. Yaghoobi, and B. Mulgrew, "Ultra High Resolution Wide Swath MIMO SAR," in *in IEEE Journal of Selected Topics in Applied Earth Observations and Remote Sensing*, vol. 13, pp. 5358-5368, 2020, doi: 10.1109/JSTARS.2020.3021914.

Undergoing Review Papers:

- M. AlShaya, M. Yaghoobi, and B. Mulgrew, "IRCI-Free Multiple-Subband MIMO SAR," in *in IET Radar, Sonar & Navigation*, (Undergoing Review).

Chapter 2
Background and Literature Review

This chapter provides the basic background and principles required for the rest of the chapters of the thesis. In addition, it gives a review of the work done in the literature in the field of multiple-input multiple-output (MIMO) synthetic aperture radar (SAR).

The first section of this chapter discusses the basic principles of radar and the second section gives the concept of MIMO radar. The third section provides the principles of SAR along with different modes of operation. In addition, it describes different methods for range profile estimation in the context of single-input single-output (SISO) SAR. The fourth and fifth sections discuss different types of single-input multiple-output (SIMO) SAR and MIMO SAR. The section after this, provides a preliminary study on system identification formulation of MIMO radar. The last section summarises the chapter.

2.1 Radar Principle

Radar is an electromagnetic sensor system used in both civilian and military sectors to detect and estimate the parameters of different targets (i.e. objects). It was first used just prior to the second world war [21]. Radar systems can be classified in accordance to the the waveforms transmitted and locations of the transmitter and receiver as will be explained next [22].

2.1.1 Radar Classifications Based on The Transmitted Waveform

Radar systems can be classified in accordance the type of the transmitted waveform into the following:

- Pulsed Radar: in which the transmitted waveform is a series of pulses as shown in Fig.2.1. The velocity (v) and range (R) of the target can be estimated by measuring the Doppler shift (f_d) of the echo and the delay (τ_d) between the transmitted pulse and the corresponding echo, respectively. The following can be used for the target velocity and range

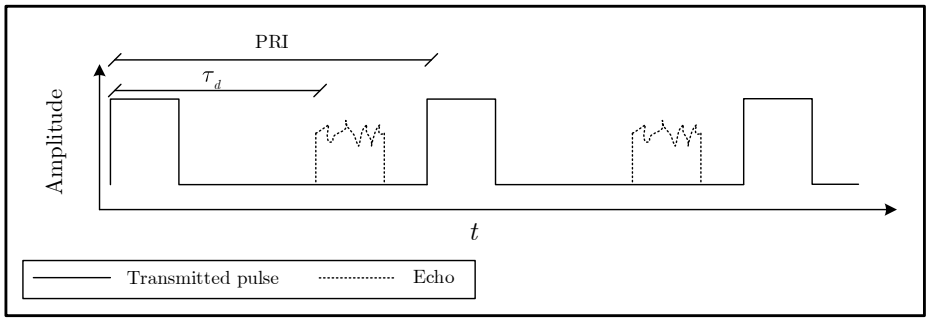

Figure 2.1: *Transmitted and return pulses in pulsed radar. PRI denotes pulse repetition interval.*

estimation:

$$R = \frac{c\tau_d}{2} \tag{2.1}$$

$$v = \frac{\lambda f_d}{2} \tag{2.2}$$

where c and λ denote the speed of light and wavelength, respectively. It should be pointed out that any waveform such as linear frequency modulated (LFM) or phase coded modulation waveforms can be used in the pulse transmission. Pulsed radar is considered throughout the thesis.

- Continuous Wave (CW) Radar: in which, as the name indicates, the waveform is transmitted continuously. The range of the target in CW radar cannot be estimated for the case when the transmitted signal is unmodulated unlike the case of the velocity (v) estimation which can be performed by measuring the Doppler shift of the echoes. A frequency modulated continuous wave (FMCW) radar is introduced to estimate the range by observing the delay between the current frequency modulation of the transmitted signal and the corresponding frequency modulation of the echoes as shown in Fig.2.2.

2.1.2 Radar Classifications Based on The Transmitter and Receiver Locations

Radar systems can be classified in accordance to the transmitter and receiver locations into the following:

- Monostatic radar: in which the transmitter and receiver are colocated as shown in Fig.2.3.

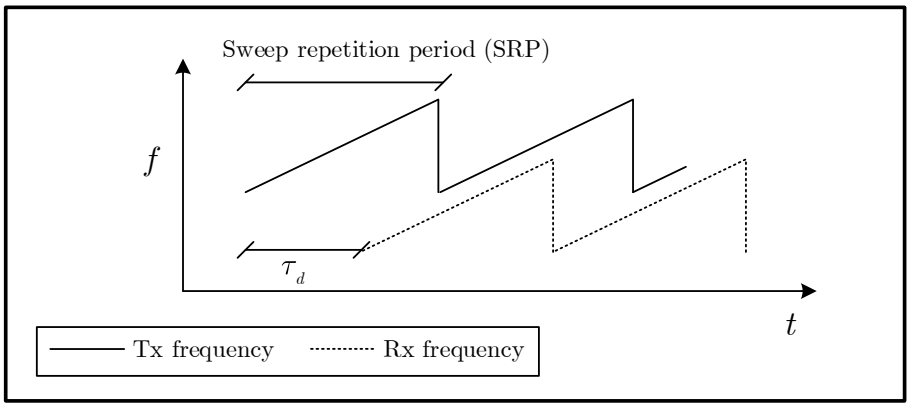

Figure 2.2: *Frequency modulation variation in FMCW radar.*

In this configuration, the time delay between the transmitter and the target is the same as the one between the target and the receiver. In addition, the angle of departure (φ) is the same as the angle of arrival (θ). Monostatic radar is considered throughout the thesis.

- Bistatic Radar: in which the transmitter and receiver are well-separated as shown in Fig.2.4 and the time delay between the transmitter and the target may not be the same as the one between the target and receiver which makes the target localisation not as simple as the one in monostatic radar. In this configuration, the target can be localised by solving the bistatic triangle [21]. In addition, bistatic radar can be generalised into multistatic radar when the number of transmitter and/or receiver is greater than one. Multistatic radar outperforms monostatic radar in detecting targets with stealth technology [23]. Bistatic radar is considered only in the preliminary study in Section 2.6.

2.2 MIMO Radar

The MIMO concept has been recently introduced into the field of radar [24][25]. MIMO radar can be viewed as a general case of a phased array radar for the case when the transmit antenna elements emit linearly independent waveforms. Echoes corresponding to the transmitted waveforms can be extracted at the receiver using a bank of matched filter.

MIMO radar can be categorised based on the locations of the antenna arrays into the following [22]:

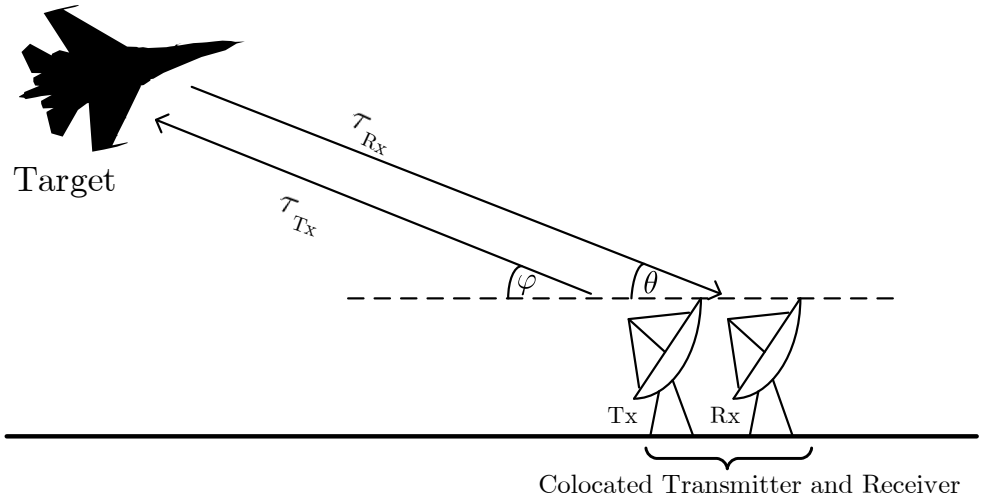

Figure 2.3: *Monostatic radar configuration in which $\tau_{Tx} = \tau_{Rx}$ and $\varphi = \theta$. τ_{Tx} denotes the delay between the transmitter and target, τ_{Rx} denotes the delay between the receiver and target, φ, and θ are the angles of departure and arrival, respectively.*

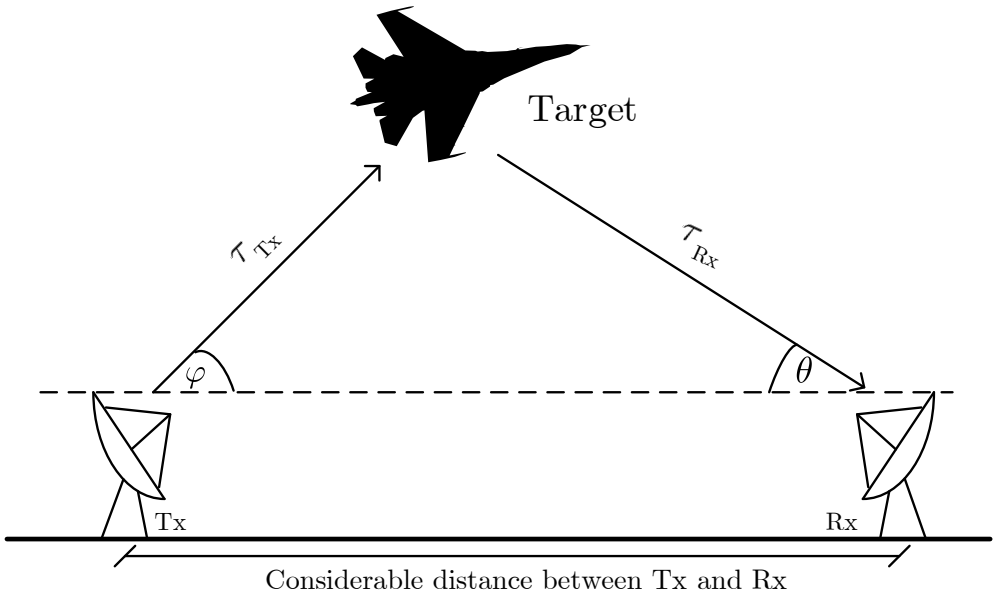

Figure 2.4: *Bistatic radar configuration. τ_{Tx} denotes the delay between the transmitter and target, τ_{Rx} denotes the delay between the receiver and target, φ, and θ are the angles of departure and arrival, respectively.*

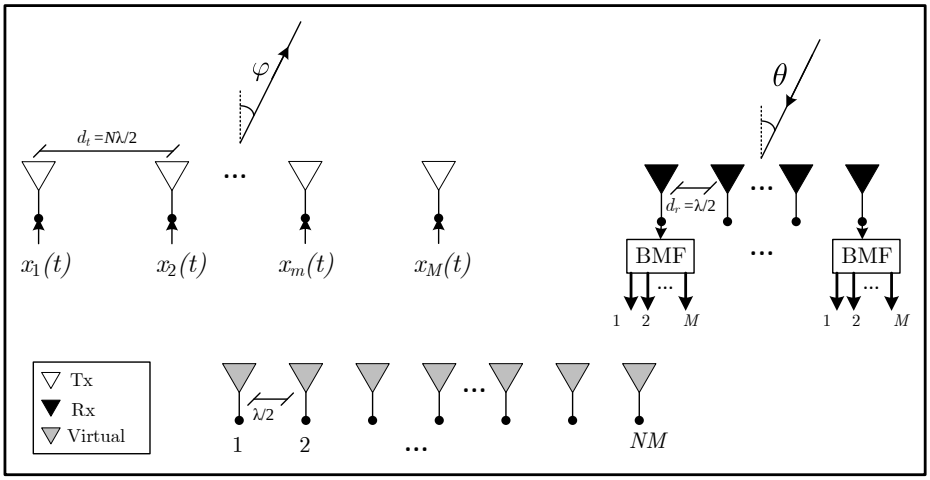

Figure 2.5: *Virtual array construction in colocated MIMO radar. N denotes the number of receiving antennas, λ is the wavelength, d_t, and d_r denote the separation between the adjacent transmitting antennas and receiving antennas, respectively. BMF stands for bank of matched filters.*

- Distributed MIMO radar [26][27]: in which widely separated antennas are employed to make use of the spatial diversity, which mitigates the effect of the received power fluctuations "scintillations" and improves the performance of moving target detection (MTD) [28]. The fluctuations of the energy reflected from a target depend on the range and direction of the target as it is composed of many scatterers [29]. Therefore, when the transmitting antennas are placed far apart in space, different aspects of the target can be obtained which reduces the effect of scintillations.

- Colocated MIMO radar [30][31]: in which the transmitters and receivers are closely spaced arrays such that the angle of arrival (AoA) is the same as the angle of departure (AoD). As the transmitting waveforms are orthogonal, a virtual array can be constructed to improve the spatial resolution as shown in Fig.2.5 for the case when ($\theta = \varphi$). In addition, this configuration has shown to offer direct applicability of adaptive array processing algorithms [32][33][34], higher sensitivity to detecting targets of low velocities [35], parameters identification with better performance [36][37][32] and higher resolution [38][24].

2.2.1 Signal Model

Consider a narrowband MIMO radar system with an array of M antenna elements at the transmitter and an array of N antenna elements at the receiver as shown in Fig.2.5. A set of M orthogonal waveforms $x_m(t), (\forall m = 1, 2, , ..., M)$ are emitted through the transmitting array. The baseband received signal at the nth receive antenna reflected from a target located at the position (φ, θ) can be expressed as

$$y_n(t) = \sum_{m=1}^{M} \sum_{l=0}^{L-1} \sigma_l e^{-j2\pi F_c \tau_l} e^{-j2\pi F_c \gamma_m} e^{-j2\pi F_c \beta_n} x_m(t - \tau_l - \gamma_m - \beta_n) + w_n(t) \qquad (2.3)$$

where τ_l and σ_l denote the delay and the radar cross section (RCS) of the scattering point located at the lth range cell, respectively. L is the total number of range cells in the range profile, F_c denotes the carrier frequency in Hz and $w_n(t)$ denotes the nth receive antenna noise which is assumed to be zero mean complex Gaussian noise. γ_m and β_n denote the time delay differences between the mth transmit antenna to the transmitting array reference point (i.e. first transmit antenna) and from the nth receive antenna to the receiving array reference point (i.e. first receive antenna), respectively, and can be expressed as follows:

$$\gamma_m = \frac{m d_t \sin(\varphi)}{c} \qquad , m = 1, 2, ..., M \qquad (2.4)$$

$$\beta_n = \frac{n d_r \sin(\theta)}{c} \qquad , n = 1, 2, ..., N \qquad (2.5)$$

where d_t denotes the separation between the adjacent transmitting antennas, d_r is the separation between the adjacent receiving antennas, φ, and θ denote the angle of departure and angle of arrival, respectively. The received signal in (2.3) can be rewritten under the assumption that the baseband signal $x_m(t - \tau_l)$ does not change significantly as it travels across the array [39] as follows:

$$y_n(t) \approx \sum_{m=1}^{M} \sum_{l=0}^{L-1} \sigma_l e^{-j2\pi F_c \tau_l} x_m(t - \tau_l) e^{-j2\pi F_c \gamma_m} e^{-j2\pi F_c \beta_n} + w_n(t) \qquad (2.6)$$

2.2.2 Virtual Array Concept

In each receiving antenna, the echoes corresponding to the orthogonal transmitted waveforms can be extracted using a bank of matched filters. The received signal in (2.6) for the case of

colocated MIMO radar ($\varphi = \theta$) can be expressed as the following:

$$y_n(t) = \sum_{m=1}^{M} \sum_{l=0}^{L-1} \sigma_l e^{-j2\pi F_c \tau_l} x_m(t - \tau_l) e^{-j2\pi f_v((n+\alpha m))} + w_n(t) \tag{2.7}$$

where $f_v = \frac{d_r}{\lambda} \sin(\theta)$ and $\alpha = \frac{d_t}{d_r}$. Consider the case when $\alpha = N$ as shown in Fig.2.5, the $(N \times M)$ signals extracted from (2.7) $(\forall n = 0, 1, ..., N-1)$ using a bank of matched filters (BMF) can be viewed as the signals received by a virtual array with $(N \times M)$ elements. The $(N \times M)$ degrees of freedom are obtained with only $N + M$ physical array elements. The relation between the functions that characterise the locations of the transmitting array $g_T(\mathbf{x})$, receiving array $g_R(\mathbf{x})$ and virtual array $g_v(\mathbf{x})$ can be expressed as [35]

$$g_v(\mathbf{x}) = (g_T * g_R)(\mathbf{x}) \tag{2.8}$$

$$g_T(\mathbf{x}) = \sum_{m=1}^{M} \delta(\mathbf{x} - \mathbf{x}_{T,m}) \tag{2.9}$$

$$g_R(\mathbf{x}) = \sum_{n=1}^{N} \delta(\mathbf{x} - \mathbf{x}_{R,n}) \tag{2.10}$$

where $*$ denotes convolution, $\mathbf{x}_{T,m} \in \mathcal{R}^3$ and $\mathbf{x}_{R,m} \in \mathcal{R}^3$ are the locations of the $m\text{th}$ transmitting antenna and $n\text{th}$ receiving antenna, respectively. Using the concept of the virtual array, additional spatial sampling can be obtained which improves the spatial resolution.

The core issue in MIMO radar is to come up with orthogonal waveforms that meet the following criteria as reported in [40]:

1. The waveforms should be as orthogonal as possible despite their time delays.
2. The waveforms should have a constant envelop in the frequency domain to maximise the signal to noise ratio.
3. The waveforms should have low peak to average power ratio (PAPR) to maximise the efficiency of the transmitter modules.
4. The waveforms should share the same frequency band with the same bandwidth so that the range resolution is not reduced.

The fourth criterion can be relaxed for the case of colocated MIMO Radar in such a way that the transmitting waveforms do not share the same frequency band and a single waveform can

be formed at the receiver by the use of digital beamforming (DBF). This is possible because all targets radar cross section coefficients between the transmit and receive antennas are the same [40].

2.3 SAR Principle

SAR imaging has the advantage over the optical instrument in a way that it can construct the image regardless of the weather conditions (i.e. during night and cloudy weather). The extremely long aperture in SAR system, which is impractical to build, is created by exploiting the relative motion between the antenna in SAR system and the imaging scene [41].

2.3.1 SAR Modes

The long synthetic aperture in SAR system is usually implemented by placing the radar on a moving platform (i.e. airplane or satellite) from which the scene to be imaged is illuminated continuously with the emitted radar pulses. The echoes corresponding to the emitted radar pulses are received in sequence and processed coherently to form the image [41]. The synthetic aperture can be implemented in a different way in which the radar is stationary by utilising the movement of the target to be imaged. This implementation is called inverse SAR (ISAR) [42]. Conventional SISO SAR has a tradeoff between the desired wide swath width and high cross-range resolution. Accordingly, SIMO SAR [43] and MIMO SAR [5][6][7] have been proposed in the literature to overcome this contradiction. In this section, the following basic SAR modes will be briefly described:

- Stripmap mode.
- Spotlight mode.
- Sliding spotlight mode.

2.3.1.1 Stripmap SAR

A SAR system in this mode, which is mounted on a moving platform (i.e. airplane or satellite) with a side-looking antenna, travels along the y-axis at a velocity of v_p as shown in Fig.2.6. A series of pulses are emitted by the radar and their corresponding echoes are recorded. The point

target P in Fig.2.7 enters the radar beam when the SAR system is located at position A and exits the beam when the SAR system is at point C. A representation of the 2-D recorded raw data matrix is shown in Fig.2.8 where it is clear that the trajectory of the point scatterer changes with each transmitted pulse. The first dimension of the recorded data matrix known as fast time defines the time duration for operation of each pulse and corresponds to the sampled signal in the range dimension (i.e. the range orthogonal to the flight path). The second dimension of the data matrix known as slow time defines the time at which pulses are transmitted along the flight path (i.e. azimuth dimension). The synthetic aperture length L_s is determined by calculating the distance between point A and point C. The distance between the SAR system and the point target P is the closest and denoted by R_0 when the SAR system is located at point B. The instantaneous slant range between the SAR system and the point target can be expressed as a function of the slow time η and approximated using a Taylor series expansion to the second order as follows [44]:

$$\begin{aligned} R(\eta) &= \sqrt{R_0^2 + (v_p\eta)^2} \\ &\approx R_0 + \frac{(v_p\eta)^2}{2R_0} \end{aligned} \tag{2.11}$$

The 3-dB beamwidths of the mainlobe in the azimuth (i.e. cross-range) and elevation directions can be expressed as follows [45]:

$$\theta_{az,\text{3dB}} = \frac{0.886\lambda}{L_a} \tag{2.12}$$

$$\theta_{el,\text{3dB}} = \frac{0.886\lambda}{H_a} \tag{2.13}$$

where L_a denotes the antenna length in azimuth, H_a is the antenna height in elevation, and λ is the carrier wavelength. The ground swath width W_g and beam footprint length L_b can be approximated as follows [45]:

$$W_g \approx \frac{0.886\lambda R_0}{H_a \cos(\theta_i)} \tag{2.14}$$

$$L_b \approx \frac{0.886\lambda R_0}{L_a} \tag{2.15}$$

where θ_i denotes the incident angle. The Doppler bandwidth B_d in stripmap SAR can be

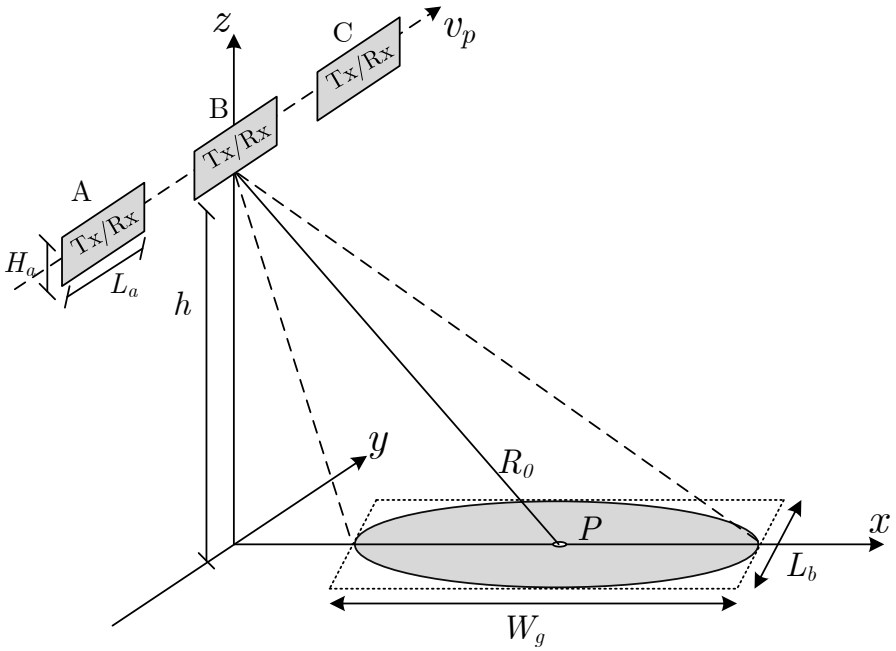

Figure 2.6: *Stripmap SAR configuration. L_a denotes the antenna length in azimuth, H_a is the antenna height in elevation, h denotes the platform height, P is a point target located at the swath centre, R_0 denotes the minimum distance to the swath centre, v_p is the platform velocity, W_g, and L_b are the ground swath width and beam footprint length, respectively.*

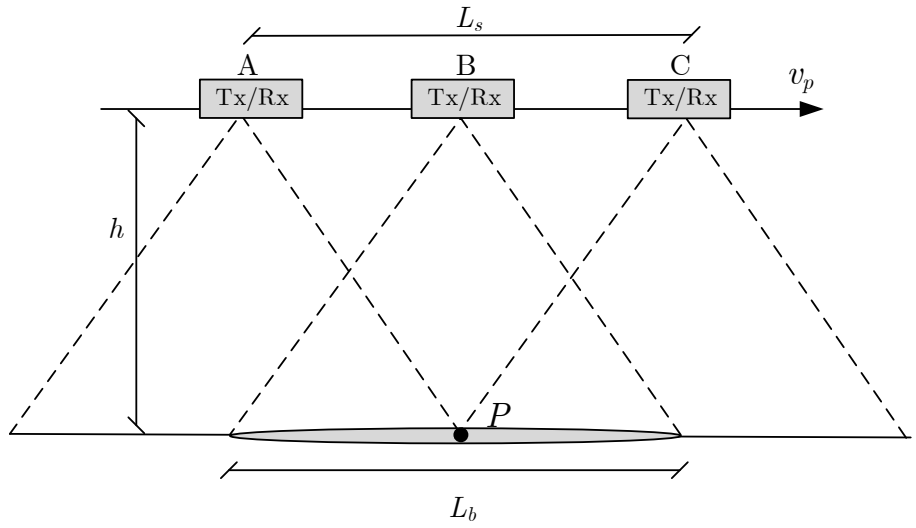

Figure 2.7: *Elevation view of stripmap SAR configuration. P is a point target located at the swath centre, v_p is the platform velocity, h denotes the platform height, L_b, and L_s denote the beam footprint length and synthetic aperture length, respectively.*

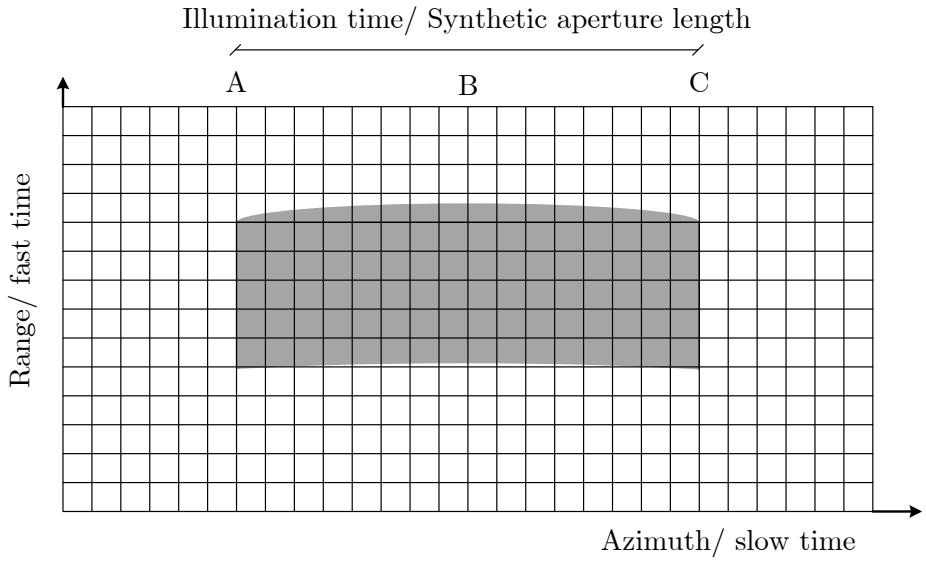

Figure 2.8: *A representation of the 2-D recorded raw data matrix.*

calculated as follows for the case of boresight direction [43]:

$$B_d \approx \frac{2v_p}{L_a} \approx \frac{v_p}{\Delta_{cr}} \tag{2.16}$$

where Δ_{cr} denotes the cross-range resolution. The pulse repetition frequency (PRF), $f_p = \frac{1}{T_r}$ where T_r denotes the pulse repetition interval (PRI), must be larger than the Doppler bandwidth in order to avoid aliasing in the Doppler spectrum, but increasing f_p arbitrarily may result in range ambiguities as T_r needs to satisfy the following condition:

$$2T_r > \frac{W_g \sin(\theta_i)}{c} \tag{2.17}$$

where c denotes the speed of light. The following condition must be satisfied to avoid ambiguities in both azimuth and range dimensions [46]:

$$\frac{v_p}{\Delta_{cr}} < f_p < \frac{c}{2W_g \sin(\theta_i)} \tag{2.18}$$

In (2.18), one can see that increasing W_g results in a coarser cross-range resolution Δ_{cr} for a given f_p, while a finer cross-range resolution leads to a decrease in the swath width W_g. Accordingly, it is not possible to improve both of the swath width and the cross-range resolution at the same time. This tradeoff is addressed in the literature by introducing SIMO SAR and MIMO SAR. Throughout the thesis, MIMO SAR configuration will be considered.

2.3.1.2 Spotlight SAR

The radar beam in spotlight SAR is steered towards the centre of the imaging scene during the illumination time as shown in Fig.2.9. This implies that the scene to be imaged is always illuminated by the radar beam which makes the synthetic aperture length longer than the one in stripmap SAR. As a result, the cross-range resolution is much higher than the one in stripmap SAR and it is a function of the data acquisition length unlike the case of the stripmap SAR in which the cross-range resolution is a function of the antenna beamwidth [44]. However, the azimuth width (i.e. imaging scene area) is limited as it is a function of the antenna beamwidth unlike the case of the stripmap SAR in which the azimuth width is a function of the data acquisition length.

Due to the continuous steering of the antenna beam in the spotlight SAR, the Doppler centroid is

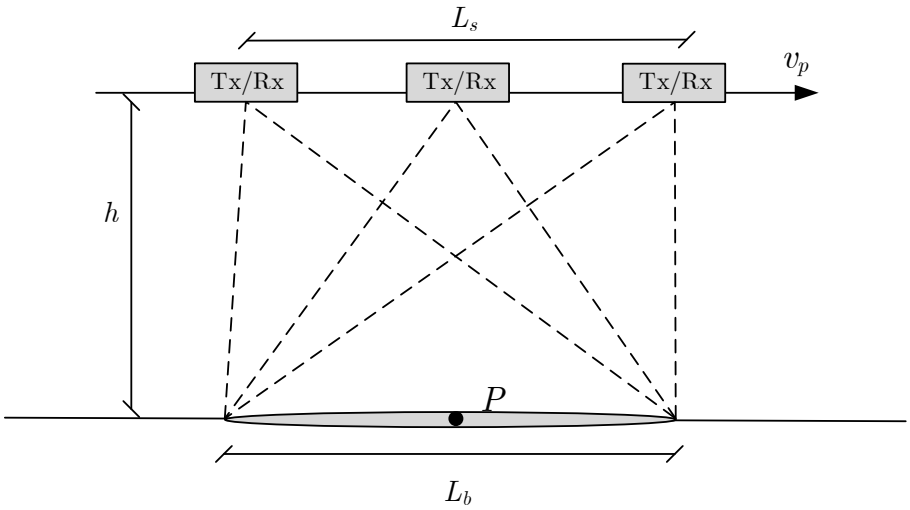

Figure 2.9: *Spotlight SAR configuration. P is a point target located at the swath centre, v_p is the platform velocity, h denotes the platform height, L_b, and L_s denote the beam footprint length and synthetic aperture length, respectively.*

time-varying unlike the case of of the stripmap SAR in which the Doppler centroid is constant. The azimuth frequency course as function of slow time of different scatterers of the two SAR modes are shown in Fig.2.10. Table 2.1 summarises a comparison between spotlight SAR and stripmap SAR [44].

Attribute	Spotlight SAR	Stripmap SAR
Antenna Steering	Real-time steering towards the centre of the imaging scene.	Fixed beam
Synthetic aperture	It is the same for all scatterers in the scene.	Scatterers located at different azimuth locations have different synthetic apertures.
Cross-range resolution	Function of the data acquisition length.	Function of the antenna beamwidth.
Imaging azimuth width	Function of the antenna beamwidth.	Function of the data acquisition length.
Doppler centroid	Time-varying	Constant
Overall Doppler bandwidth	$B_d + B_a$	B_d

Table 2.1: *A comparison between spotlight SAR and stripmap SAR*

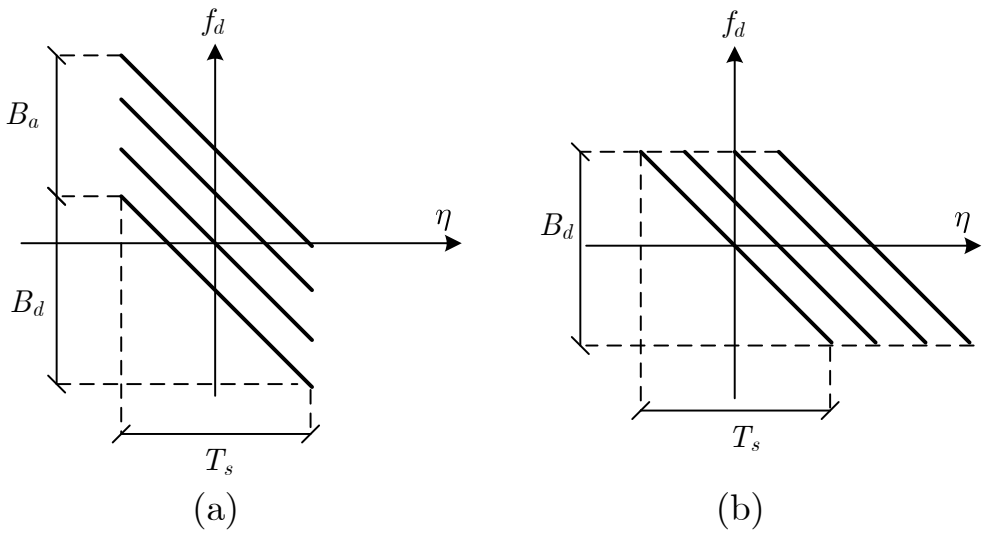

Figure 2.10: *Azimuth frequency of four scatterers as a function of slow time in (a)Spotlight SAR and (b)Stripmap SAR. f_d denotes the Doppler frequency, η is the slow time, T_s denotes the synthetic aperture time, B_d, and B_a are the Doppler bandwidth of a single scatterer and the extra bandwidth resulted from having a time-varying Doppler centroid, respectively.*

2.3.1.3 Sliding Spotlight SAR

Sliding spotlight SAR offers a tradeoff between the long illumination swath of the stripmap SAR and the high cross-range resolution of the spotlight SAR [47]. This mode of operation provides better azimuth resolution than the stripmap mode and longer imaging azimuth width than the spotlight mode by steering the radar beams during the illumination time towards a point located beyond the centre of the imaging scene as shown in Fig.2.11. Sliding spotlight mode has been successfully used in synthetic aperture radar imaging satellite TerraSar-X [48].

The azimuth bandwidth for a single point target in the sliding spotlight can be expressed as the following [49]:

$$B_D = \frac{2v_p}{L_a A} \tag{2.19}$$

where v_p is the platform velocity, L_a is the length of the radar antenna and A is the sliding factor defined as the ratio between the radar platform velocity and the velocity of the antenna

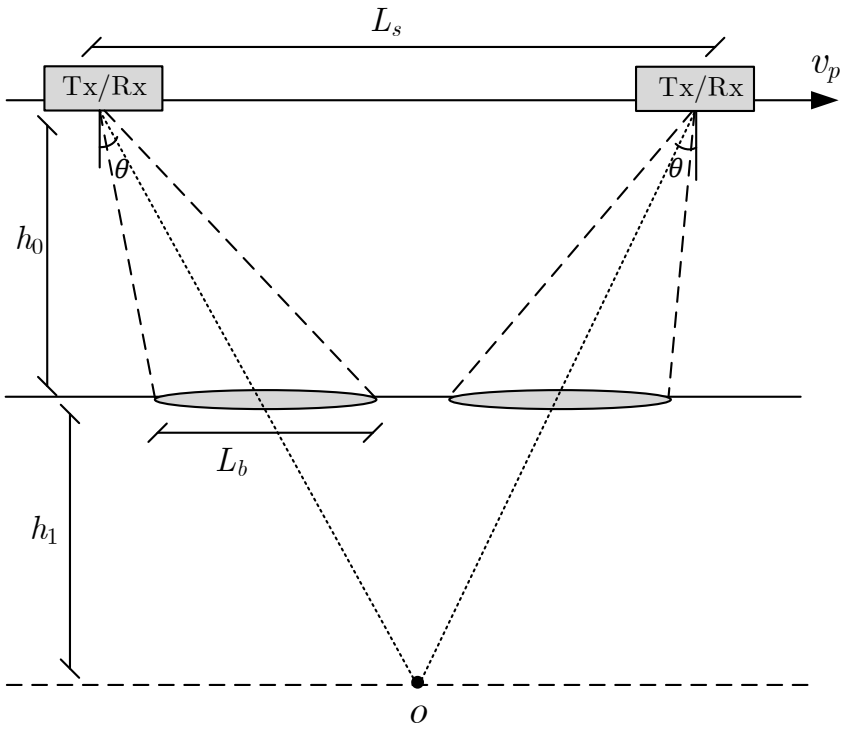

Figure 2.11: *Sliding spotlight SAR configuration. h_0 denotes the platform height, h_1 is the shortest distance between the scene and the focus point, v_p denotes the platform velocity. L_s and L_b denote the synthetic aperture length and antenna footprint length on the ground, respectively.*

beams movement on the ground which can be expressed as follows:

$$A = \frac{h_1}{h_1 + h_0} = \frac{v_f}{v_p} \tag{2.20}$$

where h_0 denotes the platform height, h_1 is the shortest distance between the scene and the focus point, v_p, and v_f denote the platform velocity and the velocity of the antenna beam movement on the ground, respectively. The overall azimuth signal bandwidth for the illuminated swath can be expressed as the following:

$$B_{overall} = \frac{2v_p}{L_a} + \frac{2v_p}{L_a}\frac{L_s}{L_b}(1 - A) \tag{2.21}$$

where L_s and L_b denote the synthetic aperture length and antenna footprint length on the ground, respectively.

2.3.2 Range Profile Estimation Methods

The SAR imaging system basically measures and processes the returns from the ground clutter which can be used to form the image. The range profile in SAR consists of a large number of scattering points rather than a small number as in the case of the classic radar mode (i.e. which is primarily used for detection and tracking). Accordingly, it is desirable to have a high range resolution with low sidelobe levels in the estimated SAR range profile so that the scattering points with low reflectivity are not overwhelmed with bright scattering points. The effects of the sidelobes of a scattering point on the adjacent range cells is known as interrange cell interference (IRCI) which increases proportionally with the number of range cells and weak scatterers could be masked by the strong ones accordingly [2]. Four different range profile estimation methods, namely, stretch processing, matched filter, cyclic prefix (CP) based orthogonal frequency division multiplexing (OFDM), and system identification are briefly explained next.

2.3.2.1 Stretch Processing

The stretch processing also known as deramp compression processing is commonly used in the conventional SISO SAR and SIMO SAR because of its implementation simplicity to process a high bandwidth LFM waveform. The stretch processing reduces the sampling frequency as the baseband frequency offset is directly proportional to the scatterer range [50]. The process of stretch processing is illustrated in Fig.2.12 in which the received signal is mixed with a

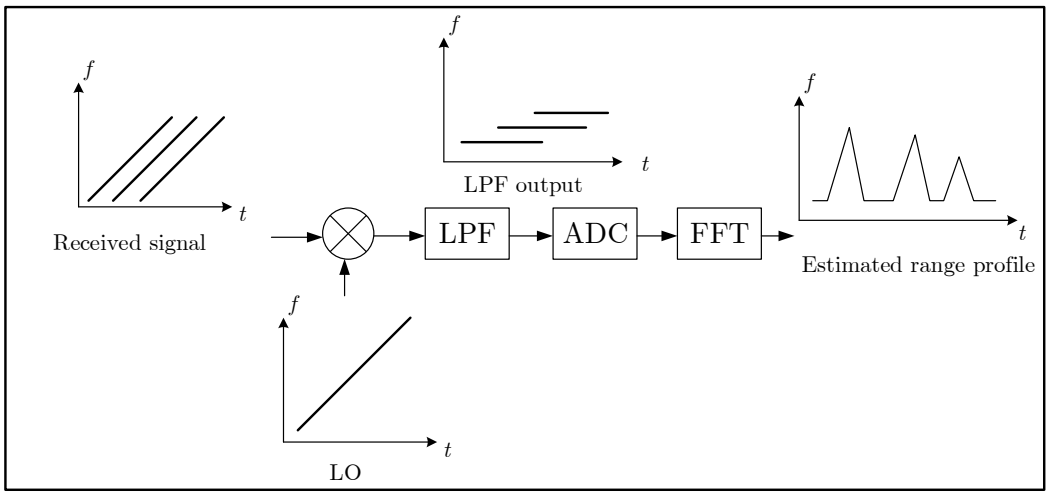

Figure 2.12: *Representation of stretch processing*

reference signal generated by a local oscillator (LO) [51]. The scatterer with a larger delay is associated with a higher residual frequency (i.e. beat frequency f_b). Next, the output of the mixer goes through a lowpass filter (LPF) and then is digitised using an analogue to digital converter (ADC). Finally, the fast Fourier transform (FFT) of the digitised signal is computed to obtain the estimated range profile (i.e. compressed output).

The relationship between the delay of the target and the beat frequency can be derived from the geometry of the deramp range compression shown in Fig.2.13 as the following:

$$f_b = \frac{B}{\Delta t}\tau_d \tag{2.22}$$

where B is the bandwidth over which the reference signal is swept, τ_d, and Δt denotes the scatterer delay and the listening time over which the returns are expected, respectively. It should be noted that it is not possible to use stretch processing with waveforms other than LFM waveform which is the main drawback but there is some effort in the literature to allow the use of a non-linear LFM waveform [52].

2.3.2.2 Matched Filter

The matched filter is a special type of filter which is widely used in radar signal processing. The impulse response of the matched filter is determined in a way to maximise the signal to noise

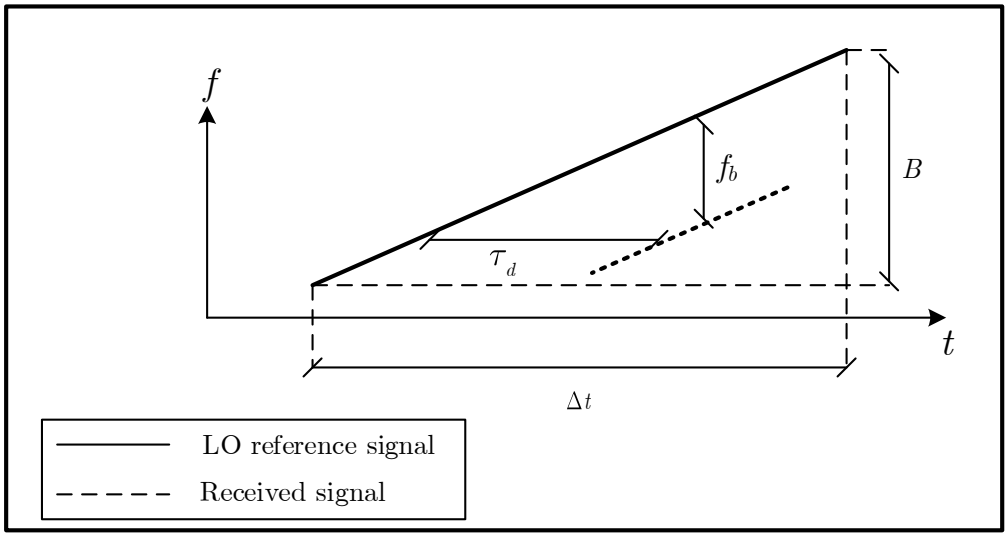

Figure 2.13: *Deramp range compression geometry. f_b denotes the beat frequency, B is the bandwidth over which the reference signal is swept, τ_d, and Δt denotes the scatterer delay and the listening time over which the returns are expected.*

ratio (SNR) of a single target in white Gaussian noise. Therefore, the detection probability is maximised [53]. The impulse response of the matched filter $h_{MF}[n] = x[-n]$ is a conjugated and time reversed copy of the transmitted signal $x[n]$. In other words, the output of the matched filter is simply a deconvolution of the received and transmitted signals which can be expressed as follows:

$$\hat{h}[n] = \sum_{k=-\infty}^{\infty} y[k] h_{MF}[n-k] \tag{2.23}$$

where $\hat{h}[n]$ is the estimated range profile, $y[n]$ denotes the received signal. The performance of the matched filter is determined by its auto-correlation function (i.e. point spread function (PSF)) and the output peak SNR of the matched filter is independent of the transmitted waveform and can be expressed as the following for the case when the noise is additive white Gaussian of zero mean and power spectral density of $N_0/2$ [54]:

$$\text{SNR} = \frac{2E}{N_0} \tag{2.24}$$

where E denotes the energy of the input signal. The fact that any transmitted waveform can be utilised in the matched filter (i.e. the SNR is a function only of the waveform energy and noise power) makes it widely used in MIMO SAR to separate the echoes corresponding to each

transmitted orthogonal waveform by passing the received signal through a bank of matched filters [55].

It is worth pointing out that the matched filter is optimal for detection which is not the case in SAR imaging as it is desired to estimate the range profile from the received signal which is a superposition of a large number of scattering points returns. As a result, the matched filter might not be optimal (i.e. the matched filter provides the maximum SNR for the case of a single scatterer in white Gaussian noise).

2.3.2.3 Cyclic Prefix Based Orthogonal Frequency Division Multiplexing (CP-OFDM)

A CP-OFDM waveform has been used in communications systems [56][57]. It has the advantage that the intersymbol interference (ISI) channel can be converted into multiple ISI-free subchannels under the assumption that sufficient cyclic prefix is used. Inspired by the communications systems, a CP-based OFDM waveform is proposed in SAR systems [2][4] to estimate the range profile in a way that the sidelobes level is ideally zero which is the property of IRCI-free. It should be noted that the IRCI-free property in SAR systems is analogous to the ISI-free property in the communications systems in a way that each range cell of the range profile is considered as a single path in the communication channel.

The use of the cyclic prefix allows the approximation of the interaction between the transmitting signal and the range impulse response as a circular convolution [58]. For the sake of simplicity, the estimation of the range profile will be described for the case when the azimuth time η is zero. The baseband discrete time received signal can be expressed as the following [2]:

$$u[n] = \sum_{l=0}^{L-1} h[l]s[n-l] + w[n], \quad n = 0, 1, ..., N + 2L - 3 \tag{2.25}$$

where L and N denote the length of the range profile to be estimated and the number of subcarriers used in the OFDM, respectively. $h[l]$ is the impulse response to be estimated, $w[n]$ denotes the additive white Gaussian noise and $s[n]$ is the transmitted sequence with CP. It should be noted that the transmitted signal with CP is $\mathbf{s} = [s[0], s[1], ..., s[N + L - 2]]^T$, where $[s[0], ..., s[L-2]]^T = [s[N], ..., s[N + L - 2]]^T$. The vector $[s[0], s[1], ..., s[N-1]]^T$ is the inverse discrete Fourier transform (IDFT) of N subcarriers whose complex weight is defined by $[S[0], S[1], ..., S[N-1]]^T$. On receive, the first and last $L-1$ samples are removed [40]

and the received signal can be expressed in a matrix form as the following:

$$\begin{aligned}\mathbf{u} &= [u[L-1], u[L], ..., u[N+L-1]]^T \\ &= \mathbf{H}\acute{\mathbf{s}} + \mathbf{w}\end{aligned} \tag{2.26}$$

where $\acute{\mathbf{s}} = [s[L-1], s[L], ..., s[N+L-2]]^T$,$\mathbf{w} = [w[L-1], w[L], ..., w[N+L-1]]$ and $\mathbf{H}$ is an $N \times N$ cyclic, square and Toeplitz matrix that consists of cyclically shifted copies of the N dimensional vector $\mathbf{h}_p$

$$\mathbf{h}_p = \left[h[0], h[1], ..., h[L-1], \underbrace{0, ..., 0}_{N-L}\right]^T \tag{2.27}$$

Next, The OFDM demodulator performs a discrete Fourier transform (DFT) on the vector $\mathbf{u}$ defined in (2.26) and the impulse response can be estimated in the frequency domain as the following [4]:

$$\hat{H}_p(k) = \frac{U(k)}{\acute{S}(k)} \tag{2.28}$$

The range profile can be then obtained by applying an N-point DFT. It is worth pointing out that the length of the pulsewidth in CP-based OFDM SAR should be at least equal to the length of the channel to be estimated which is not practical in some applications such as stripmap SAR. The authors in [3] proposed an algorithm to make most of the cyclic prefix zeros to solve the problem of energy efficiency but introduced a tradeoff between having a constant modulus waveforms in the frequency domain and low peak to average power ratio (PAPR) waveforms.

2.3.2.4 System Identification

In this section, the received signal of the conventional SISO SAR is formulated as a system identification problem. Next, a frequency domain system identification (FDSI) based algorithm [59] is described to estimate the impulse response in the range dimension instead of a matched filer. The estimated range profile using the FDSI-based algorithm has ideally zero sidelobes level. The algorithm proposed in [59][60] is independent of the waveform transmitted and the length of the waveform transmitted is not a function of the channel impulse response to be estimated which makes it suitable for stripmap SAR. It should be noted that the noise suppression capability is improved when the waveform length is greater than the channel to be estimated as stated in [59].

The baseband received signal at the receiver can be expressed as

$$y(t,\eta) = \sum_{l=0}^{L-1} \sigma_l e^{-j2\pi F_c \tau_l(\eta)} x(t - \tau_l(\eta)) + w(t) \tag{2.29}$$

where t and η denote the fast time and slow time, respectively. F_c denotes the carrier frequency in Hz, $x(t)$ is the transmitted waveform, σ_l is the radar cross-section (RCS) of the scattering point located at the lth range cell of the swath, $\tau_l(\eta)$ is the round trip delay of the lth scattering point, and $w(t)$ is additive white noise generated by the receiver.

The received signal in (2.29) is sampled from the range cell that corresponds to the near range to the range cell that corresponds to the far range with a sampling frequency of $f_s = 1/T_s$. The signals are also sampled in the azimuth dimension with a sampling frequency of $f_p = \mathrm{PRF}$, which is the pulse repetition frequency. The discrete time version of the received signal can be expressed as follows:

$$z[n_t, n_a] = \sum_{l=0}^{L-1} h[l, n_a] x[n_t - l] + w[n_t] \qquad 0 \le n_t \le K + L - 1 \tag{2.30}$$

where,

$$\begin{aligned} h[l, n_a] =& \sigma_l e^{-j2\pi F_c \tau_l(n_a)} \\ =& \sigma_l e^{j\phi_l(n_a)} \end{aligned} \tag{2.31}$$

K is the length of the waveform transmitted, n_t, and n_a are the range and azimuth time indices, respectively.

The estimation of the impulse response in the range dimension will be described for a given azimuth bin (i.e. a single pulse). The received signal in (2.30) can be written in a matrix form for a given azimuth bin (n_a) as

$$\begin{aligned} \mathbf{z}[n_a] =& \left[z[0, n_a], z[1, n_a], ..., z[K + L - 1, n_a]\right]^T \\ =& \mathbf{X}\mathbf{h}[n_a] + \mathbf{w}[n_a] \end{aligned} \tag{2.32}$$

where,

$$\mathbf{h}[n_a] = \big[h[0,n_a], h[1,n_a], ..., h[L-1,n_a]\big]^T, \tag{2.33}$$

$$\mathbf{w}[n_a] = \big[w[0,n_a], w[1,n_a], ..., w[K+L-1,n_a]\big]^T, \tag{2.34}$$

the matrix $\mathbf{X}$ is of dimension $(K+L-1)\times L$ which can be expressed as follows:

$$\mathbf{X} = \begin{bmatrix} x[0] & 0 & \dots & \dots & 0 \\ x[1] & x[0] & & & 0 \\ \vdots & x[1] & \ddots & & \vdots \\ x[K-1] & \vdots & \vdots & \ddots & 0 \\ 0 & x[K-1] & & & x[0] \\ 0 & 0 & \ddots & \vdots & x[1] \\ \vdots & \vdots & & \ddots & \vdots \\ 0 & 0 & \dots & 0 & x[K-1] \end{bmatrix} \tag{2.35}$$

The matrix $\mathbf{X}$ can be made circulant and accordingly, the channel impulse response $\mathbf{h}$ in (2.32) is zero padded by $(K-1)$ as follows:

$$\mathbf{z}[n_a] = \mathbf{X}_C \underbrace{\begin{bmatrix} \mathbf{h}[n_a] \\ \mathbf{0}_{(K-1)} \end{bmatrix}}_{\mathbf{h}_p[n_a]} + \mathbf{w}[n_a] \tag{2.36}$$

The channel impulse response can be estimated as follows:

$$\hat{\mathbf{h}}_p[n_a] = \mathbf{X}_C^{-1}\mathbf{z}[n_a] \tag{2.37}$$

The estimation in (2.37) can be performed easily in the frequency domain by exploiting the discrete Fourier transform (DFT) structure of $\mathbf{X}_C$ after being decomposed as follows:

$$\mathbf{X}_C = \mathbf{F}\mathrm{diag}\{\mathcal{X}\}\mathbf{F}^H \tag{2.38}$$

where $\mathcal{X}$ is the Fourier transform of the first row of the matrix $\mathbf{X}_C$ and $\mathbf{F}$ is the DFT matrix. It should be noted that the last $(K-1)$ elements of $\hat{\mathbf{h}}_p$ should be forced to be zero, which can be

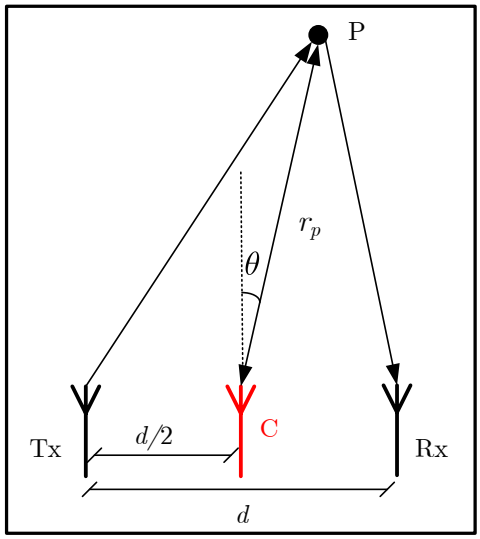

Figure 2.14: *The PCA geometry. Tx, Rx, C, P denote, respectively, the positions of the transmitter, receiver, virtual phase centre and single scatterer. θ denotes the bearing of the scatterer.*

seen as a noise removal step.

It is worth pointing out that the Doppler shift effect due to the platform motion, which can be represented as a stretching or a compression of the signal in time [61], is addressed in [58]. It is concluded that the Doppler shift effect on the range profile estimation using the FDSI-based algorithm is negligible in comparison with the matched filter and will not affect the performance of the estimation under typical operating conditions for many SAR systems.

2.3.3 The Principle of Displaced Phase Centre (DPC)

The principle of displaced phase centre (DPC) can be introduced by first considering the geometry of phase centre approximation (PCA) shown in Fig.2.14 in which Tx is the position of the transmitter at a given azimuth time and Rx denotes the position of the receiver at the instant of the reception of the echo from a scatterer located at P. The concept of the PCA is to replace the true bistatic location by a virtual monostatic one located midway between the transmitter and receiver as shown in Fig.2.14. The PCA holds when $(d^2/(4r_p) \ll \lambda)$ where d denotes the separation between the transmitter and receiver and λ is the wavelength [41].

The principle of DPC is used in the context of multi-aperture SAR configuration [43] which

consists of a receiver n separated by Δx_n from the transmitter. The azimuth impulse response $h_{az,n}(\eta)$ for a point scatterer at the azimuth time $\eta = 0$, slant range R for a carrier wavelength λ can be expressed as the following under the assumption of a straight sensor trajectory [43]:

$$h_{az,n}(\eta, \Delta x_n) = e^{-j\frac{2\pi}{\lambda}\left(\sqrt{R^2+(v_p\eta)^2}+\sqrt{R^2+(v_p\eta-\Delta x_n)^2}\right)} \tag{2.39}$$

where v_p denotes the platform velocity. Quadratic approximation of (2.39) can be expressed as the following [43]:

$$h_{az,n}(\eta, \Delta x_n) \approx e^{-j\frac{4\pi}{\lambda}R} e^{-j\frac{\pi \Delta x_n^2}{2\lambda R}} e^{-j\frac{2\pi v_p^2(\eta-(\Delta x_n/(2v_p))^2)}{\lambda R}} \tag{2.40}$$

$$\approx h_{az}(\eta - (\Delta x_n/(2v_p)) e^{-j\frac{\pi \Delta x_n^2}{2\lambda R}} \tag{2.41}$$

where $h_{az}(\eta)$ denotes the monostatic azimuth impulse response. The multi-aperture point scatterer azimuth response is a time delayed version of the monostatic response in addition to a constant phase shift as expressed in (2.41). The relationship, in the azimuth frequency domain, between the multi-aperture response $H_{az,n}(f_a)$ and monostatic response $H_{az}(f_a)$ can be described by the filter $H_n(f_a)$ as expressed below:

$$H_{az,n}(f_a) = H_n(f_a) H_{az}(f_a) \tag{2.42}$$

where,

$$H_n(f_a) = e^{-j\frac{\pi \Delta x_n^2}{2\lambda R}} e^{-j\frac{\pi \Delta x_n}{v_p} f_a} \tag{2.43}$$

The principle of DPC will be used throughout the thesis.

2.3.4 Image Formation Algorithms

Several image formation algorithms are proposed in the literature and each has its advantages and disadvantages. Some of the algorithms are range-Doppler algorithm (RDA) [62], wavenumber domain algorithm [41], and chirp scaling (CS) algorithm [63]. RDA has the simplicity of one-dimensional operations although it operates in range and azimuth frequency domain, which makes it an efficient imaging technique. In addition, it solves the problems of azimuth focusing and range cell migration correction (RCMC). However, it has some of the disadvantages such as the requirement of an interpolator for the RCMC. Wavenumber domain algorithm has the advantage of dealing directly with the natural polar coordinate system but it

requires an interpolator to match the range-dependent RCMC parameter variations [41]. CS algorithm was developed in a way to eliminate the need for an interpolator for the RCMC. It is based on the scaling principle in which a frequency modulation is applied to a chirp-encoded signal. CS algorithm is used throughout the thesis due to its computational simplicity [41]. A full description of CS algorithm is provided next.

2.3.4.1 Chirp Scaling Algorithm

The received signal defined in (2.30) will be used to describe the image formation algorithms. The first phase function of the chirp scaling algorithm equalises all range migration trajectories to a reference range r_{ref} by multiplying (2.30) in the range-Doppler domain with the following:

$$\begin{aligned} z_s(n_t, f_a) &= z(n_t, f_a) H_{\text{CS},1}(n_t, f_a) \\ &= z(n_t, f_a) \exp\left[j\pi k(f_a; r_{\text{ref}}) a(f_a) \big(n_t T_s - \frac{2R(f_a; r_{\text{ref}})}{c}\big)^2 \right] \end{aligned} \tag{2.44}$$

where,

$$R(f_a; r_{\text{ref}}) = \frac{r_{\text{ref}}}{\beta(f_a)} = r_{\text{ref}}(1 + a(f_a)), \tag{2.45}$$

$$\frac{1}{k(f_a; r_{\text{ref}})} = \frac{1}{k_r} - \frac{2\lambda r_{\text{ref}}(\beta^2(f_a) - 1)}{c^2 \beta^3(f_a)}, \tag{2.46}$$

$$\beta(f_a) = \sqrt{1 - \left(\frac{f_a \lambda}{2v_p}\right)^2}, \tag{2.47}$$

k_r is the modulation rate of the transmitted chirps and the azimuth frequency f_a varies within the following range:

$$\frac{-\text{PRF}}{2} \leq f_a \leq \frac{\text{PRF}}{2} \tag{2.48}$$

The next step is to estimate the range impulse response at every Doppler frequency using one of the range estimation algorithms described previously (i.e. matched filter or FDSI-based estimation algorithm) . The bulk RCMC is then performed by multiplying the estimated impulse response in range frequency-Doppler domain with a phase term expressed below

$$H_{\text{RCMC}}(f_r, f_a) = \exp\left[j4\pi r_{\text{ref}} a(f_a) f_r / c \right] \tag{2.49}$$

The data is then converted into range time-Doppler domain to compensate for the residual phase and perform azimuth compression using the following matched filter:

$$H_{\mathrm{CS},2}(n_t, f_a; r_{\mathrm{ref}}) = \exp\left[\frac{j2\pi r_{\mathrm{ref}}}{v_p}\sqrt{f_{am}^2 - f_a^2}\right]\exp[j\Delta\varphi(f_a, r_{\mathrm{ref}})] \tag{2.50}$$

where,

$$\Delta\varphi(f_a, r_{\mathrm{ref}}) = \frac{4\pi}{c^2}k(f_a)a(f_a)(1 + a(f_a))(r - r_{\mathrm{ref}})^2, \tag{2.51}$$

$f_{am} = \frac{2v_p}{\lambda}$ and $r = \frac{cn_tT_s}{2}$. The inverse azimuth Fourier transform is finally computed to obtain the image.

2.3.5 Digital Beamforming (DBF) on Receive in Elevation

A small size transmitting antenna is employed in an HRWS imaging application to illuminate a large footprint on the ground as shown in Fig.2.15. In addition, a large receive antenna with multiple subapertures in elevation is adopted to attain the desired SNR in the formed image [64]. The size of each receiving subaperture is generally smaller than the transmitting antenna in order to ensure the reception of the echoes from the illuminated area. The received signals at each receiving elevation subaperture is separately amplified, down-converted and digitised as illustrated in Fig.2.16. The posteriori combination of subaperture signals using any beamformer algorithm such as linearly constrained minimum variance (LCMV) beamformer algorithm [65] can be used to form beams with adaptive shape as shown in Fig.2.15. Moreover, the knowledge about the elevation directions of the scatterers can be used to perform the following [66][67]:

1. Suppression of spatially ambiguous echoes from the ground.
2. Improvement of the gain of the receiving antenna without a reduction of the imaged area.
3. Suppression of spatially localised interferences.
4. Obtaining more information about the dynamic behaviour of the scatterers.

2.4 SIMO SAR

SIMO SAR is introduced to address the tradeoff between obtaining the desired wide swath and high cross-range resolution in conventional SISO SAR. The minimum PRF in SIMO SAR

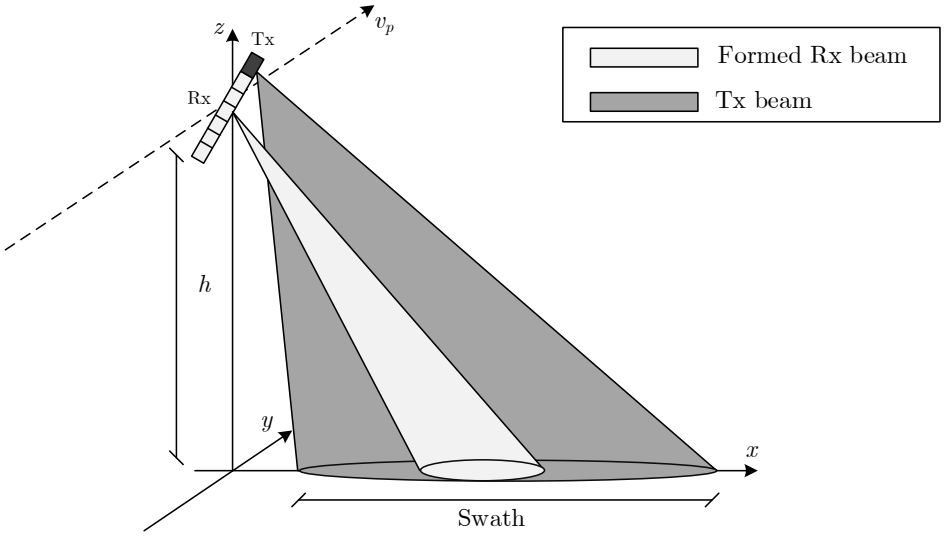

Figure 2.15: *Combination of multiple receiving subapertures in elevation.*

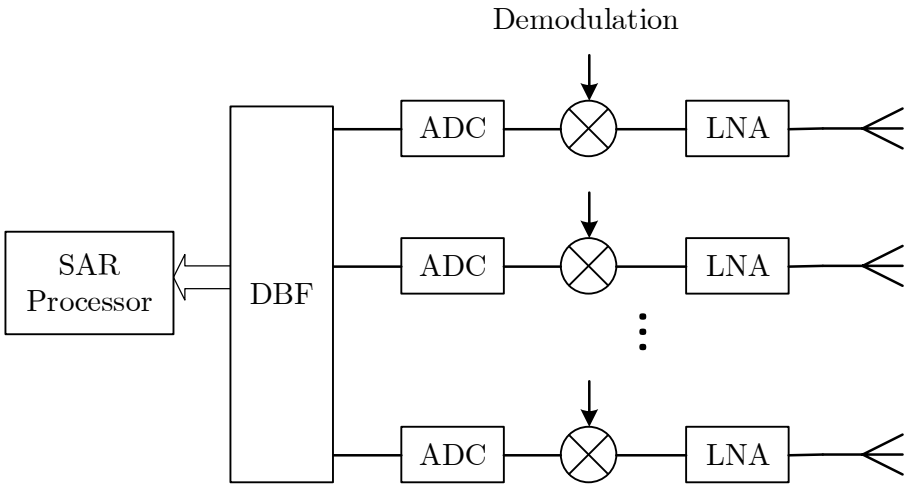

Figure 2.16: *The schematic of digital beamforming (DBF) on receive. LNA and ADC stand for low noise amplifier and analogue to digital converter, respectively. Image formation algorithm is performed in SAR processor block.*

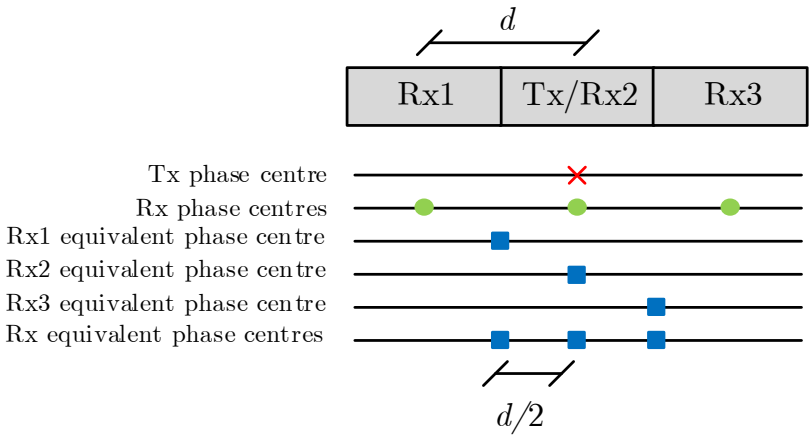

Figure 2.17: *Locations of the phase centres in SIMO SAR. d denotes the separation between the the adjacent receivers.*

should satisfy the inequality PRF $\geq B_d/K_p$ where B_d denotes the Doppler bandwidth and K_p is the number of effective phase centres which corresponds to the number of receivers. The locations of the effective phase centres in SIMO SAR, for the case when the number of receivers is three, are as illustrated in Fig.2.17. SIMO SAR can be categorised into three major types as follows [64]:

- Single-phase centre multiple beam (SPCMB).
- Displaced phase centre multiple beam (DPCMB).
- Single phase centre on transmit and displaced phase centre on receive (SPCT-DPCR).

2.4.1 SPCMB SIMO SAR

Single phase centre multiple beam (SPCMB) SIMO SAR is proposed in [64][68][66][44] where multiple narrow azimuth receive beam having a single phase centre but with different squint angles are formed. Wide Doppler bandwidth is synthesised from the Doppler spectra of the receiving azimuthal echo signals. The system PRF needs only to satisfy the Nyquist rate of the partial Doppler bandwidth corresponding to each narrow receiver beam. Therefore, the PRF can be reduced by a factor of N for a given azimuth resolution, where N denotes the number

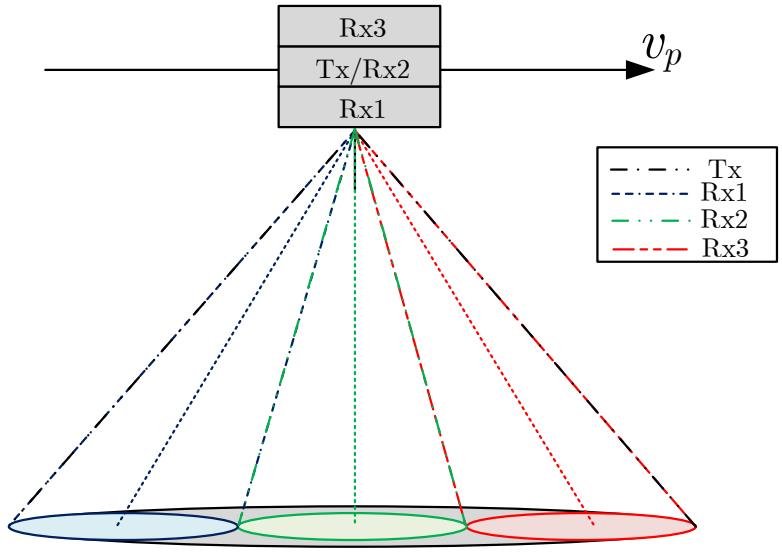

Figure 2.18: *WTNR implementation of SPCMB SIMO SAR. v_p denotes the platform velocity.*

of receivers. Two different configurations are proposed to implement SPCMB SIMO SAR, namely, wide-transmit narrow-receive (WTNR) implementation and narrow-transmit narrow-receive (NTNR) implementation.

The system geometry of WTNR implementation is illustrated in Fig.2.18, for the case of three receivers, where a wide transmit beam in azimuth is used to illuminate the entire synthetic aperture length and multiple narrow receive beam with different squint angles are used for reception. On the other hand, the NTNR implementation shown in Fig.2.19 employs multiple contiguous narrow beam in azimuth with different squint angles for both transmission and reception. The signal processing in both implementations is the same but azimuth ambiguity characteristics are different as will be described next. The spectral distribution of SPCMB SIMO SAR is shown in Fig.2.20 where it is clear that the squint angles of the narrow receive beams are translated into different Doppler centroids.

The main challenging of SPCMB SIMO SAR is the interbeams suppression which is required to reduce the azimuth ambiguity level. This is the result of the overlap between the sidelobes of the receive beams with the mainlobes of the adjacent beams.

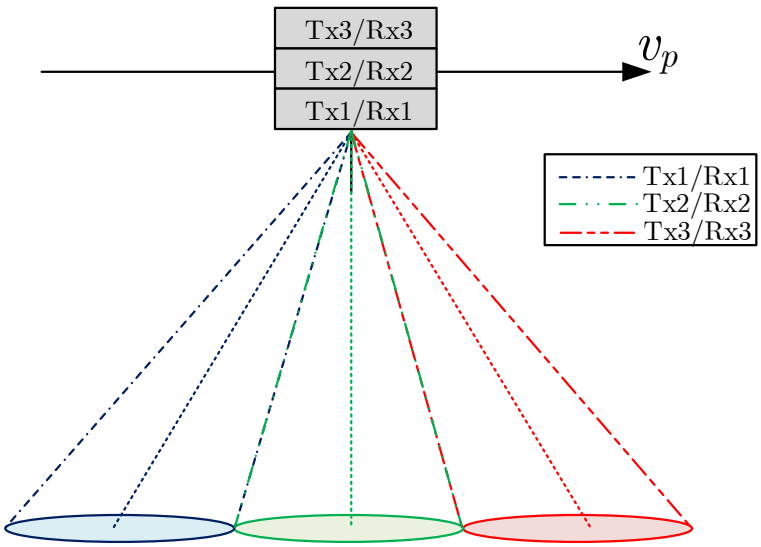

Figure 2.19: *NTNR implementation of SPCMB SIMO SAR. v_p denotes the platform velocity.*

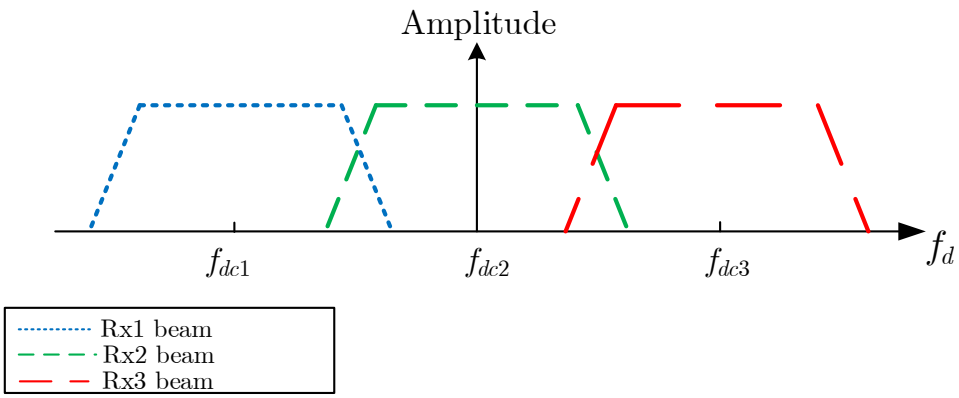

Figure 2.20: *Spectral distribution of the echo signal in each receiving beam in SPCMB SIMO SAR. f_{dci} denotes the Doppler centroid of the echo signal in the ith receiver.*

2.4.1.1 Azimuth Ambiguity Analysis

The azimuth beams of the receivers are not ideal and the sidelobes of the receive beams will overlap with the mainlobes of the adjacent azimuth beams.

Without loss of generality, raised cosine function is used to generate the transmit and receive beam patterns in the azimuth ambiguity analysis. The transmitter beam in WTNR implementation is N times wider than any receive beam so that the one-way normalised azimuthal transmit and receive power patterns can be expressed as the following [69]:

$$G_t(\theta) = \left(\mathrm{sinc}\big(U_{Tx}(\theta)\big)\frac{\cos(\pi U_{Tx}(\theta))}{1-4(U_{Tx}(\theta))^2}\right)^2 \tag{2.52}$$

$$G_{r,n}(\theta) = \left(\mathrm{sinc}\big(U_{Rx,n}(\theta-\theta_n)\big)\frac{\cos(\pi U_{Rx,n}(\theta-\theta_n))}{1-4(U_{Rx,n}(\theta-\theta_n))^2}\right)^2 \tag{2.53}$$

where,

$$U_{Tx}(\theta) = \frac{\pi L_a}{N\lambda}\sin(\theta), \tag{2.54}$$

$$U_{Rx,n}(\theta) = \frac{\pi L_a \cos(\theta_n)}{\lambda}\sin(\theta) \tag{2.55}$$

for ($n = 1, 2, ..., N$). θ_n and L_a denote the squint angle of the nth receiver and the antenna azimuth length of the receiver, respectively. The normalised equivalent combined power pattern of the broad transmit beam and the nth narrow receive beam can be expressed as follows:

$$G_n(\theta) = \left(\mathrm{sinc}\big(U_{Tx}(\theta)\big)\frac{\cos(\pi U_{Tx}(\theta))}{1-4(U_{Tx}(\theta))^2}\right)^2 \left(\mathrm{sinc}\big(U_{Rx,n}(\theta-\theta_n)\big)\frac{\cos(\pi U_{Rx,n}(\theta-\theta_n))}{1-4(U_{Rx,n}(\theta-\theta_n))^2}\right)^2 \tag{2.56}$$

The 3-dB width of the combined pattern in (2.56) is 30% wider than the narrow receive beam [70]. Therefore, the PRF should be 30% higher than the ideal case in order to achieve the desired azimuth ambiguity level. The azimuth ambiguity to signal ratio (AASR) for the nth receive beam in WTNR implementation can be computed as follows [44]:

$$\mathrm{AASR}_n = \frac{\sum_{\substack{k=-\infty \\ k\neq 0}}^{\infty} \int_{(f_{dc,n}-0.5B_{d,\mathrm{Rx}})}^{(f_{dc,n}+0.5B_{d,\mathrm{Rx}})} G_n^2(f+kf_r)\mathrm{d}f}{\int_{(f_{dc,n}-0.5B_{d,\mathrm{Rx}})}^{(f_{dc,n}+0.5B_{d,\mathrm{Rx}})} G_n^2(f)\mathrm{d}f} \tag{2.57}$$

where $f_{dc,n}$ is the Doppler centroid of the nth receiver, f_r is the PRF, and $B_{d,\mathrm{Rx}}$ is the Doppler

bandwidth of a single receiver.

The azimuth ambiguity is different for the case of NTNR implementation. It consists of two components in which the first component is the same as the conventional SISO SAR, while the second component is due to the echoes which are transmitted by the other beams. The AASR in this case can be expressed as follows [44]:

$$\mathrm{AASR}_n = \frac{P_{n,\mathrm{ambig}}}{P_{n,\mathrm{sig}}} \tag{2.58}$$

where,

$$P_{n,\mathrm{ambig}} = \sum_{\substack{k=-\infty \\ k\neq 0}}^{\infty} \Bigg[\int_{(f_{dc,n}-0.5B_{d,\mathrm{Rx}})}^{(f_{dc,n}+0.5B_{d,\mathrm{Rx}})} G_{r,n}^2(f+kf_r)\mathrm{d}f + \sum_{m\neq n} \int_{(f_{dc,n}-0.5B_{d,\mathrm{Rx}})}^{(f_{dc,n}+0.5B_{d,\mathrm{Rx}})} G_{r,n}(f+kf_r)G_{r,m}(f+kf_r)\mathrm{d}f \Bigg], \tag{2.59}$$

$$P_{n,\mathrm{sig}} = \int_{(f_{dc,n}-0.5B_{d,\mathrm{Rx}})}^{(f_{dc,n}+0.5B_{d,\mathrm{Rx}})} G_{r,n}^2(f)\mathrm{d}f + \sum_{m\neq n} \int_{(f_{dc,n}-0.5B_{d,\mathrm{Rx}})}^{(f_{dc,n}+0.5B_{d,\mathrm{Rx}})} G_{r,n}(f)G_{r,m}(f)\mathrm{d}f, \tag{2.60}$$

2.4.2 DPCMB SIMO SAR

Displaced phase centre multiple beam (DPCMB) SIMO SAR shown in Fig.2.21 is first presented in details in [70] where a broad beam transmit antenna is used to emit radar pulses and multiple receiving aperture used for reception are placed along the azimuth dimension and separated by an appropriate distance to obtain uniform sampling of the total received signal. In addition, the PRF should be selected in a strict way in order to guarantee uniform sampling, which may contradict the timing diagram selection and affect the azimuth ambiguity suppression. The reconstruction of a nonuniform sampled signal is proposed in [43] using a set of reconstruction filters or DBF with a null steering technique. DPCMB SIMO SAR has been implemented successfully in TerraSAR-X and Radarsat-2 [64].

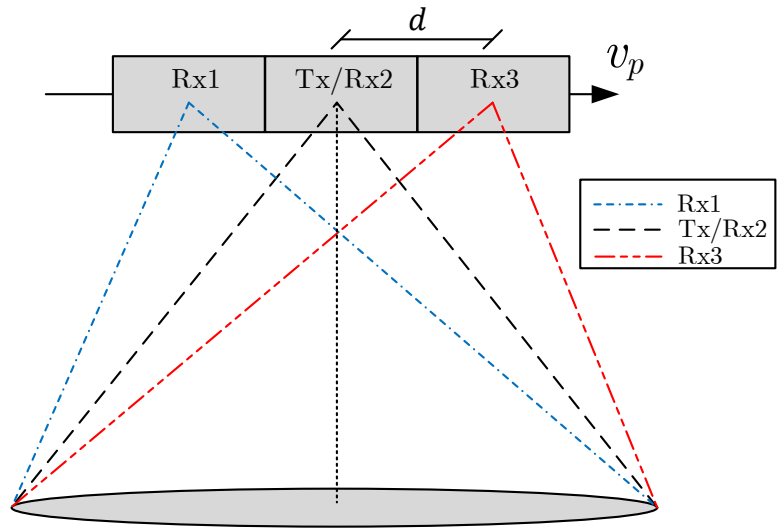

Figure 2.21: *DPCMB SIMO SAR configuration. d and v_p denote the distance between the adjacent receivers and the platform velocity, respectively.*

2.4.3 SPCT-DPCR SIMO SAR

Single phase centre on transmit and DPC on receive is an improvement of DPCMB SIMO SAR in a way that the wide transmit beam is obtained (i.e. synthesised) by combining multiple narrow transmit beams instead of using a small transmit antenna. The wide transmit beam is synthesised from a narrow transmit beam by sequentially emitting multiple subpulses in a single PRI [66]. Each transmitted subpulse is associated with a different transmit narrow beam as shown in Fig.2.22. This operation allows to attain the desired SNR by using a large transmit antenna. Each receiver in this configuration consists of N_{el} elevation channels which allows the use of DBF on receive in elevation.

Furthermore, the use of DBF on receive in elevation described in Section 2.3.5 along with a synthesised wide beam can be used to suppress the receiving interbeams overlapping. This is because echoes corresponding to different subpulses (at each instant of time) arrive from different elevation angles. Therefore, it is possible to separate them by digital beamforming on receive in elevation using the relation between time delay and elevation angle in a side-looking radar imaging geometry. One of this operation drawbacks is the enlargement of the blind area due to the increase of the transmit window size (i.e. multiple subpulses are transmitted in a PRI). The AASR at the nth receiver in this configuration can be expressed as the following

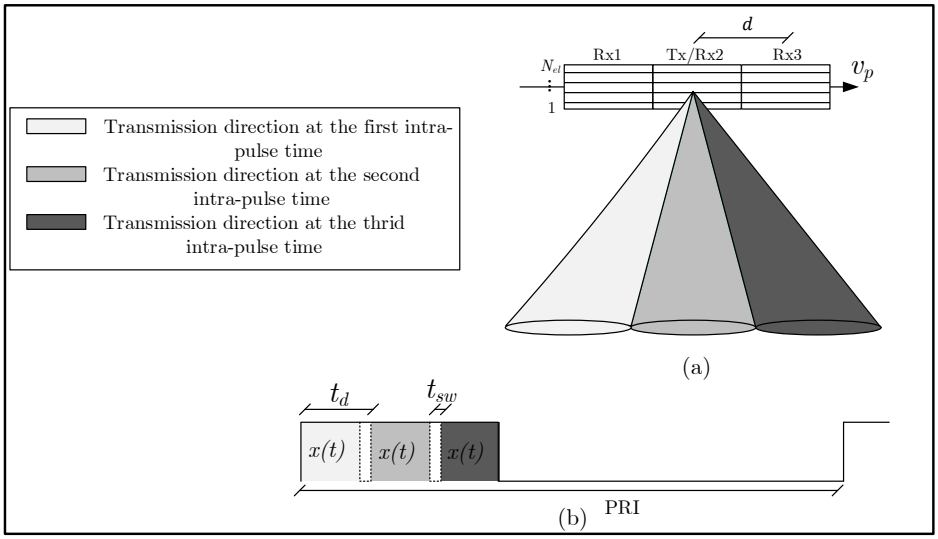

Figure 2.22: *Generation of a synthesised wide transmission beam from a narrow beam. (a) Transmission directions sequence of the transmitter where* d *denotes the separation between the adjacent receivers. (b) Timing structure of a single* PRI *where* $x(t)$ *is the transmitted waveform,* t_d*, and* t_{sw} *denote the delay between the subsequent transmitted subpulses and the beam switching time, respectively. Each receiver consists of* N_{el} *elevation channels.*

[44]:

$$\mathrm{AASR}_n = \frac{P_{n,\mathrm{ambig}}}{P_{n,\mathrm{sig}}} \tag{2.61}$$

where,

$$P_{n,\mathrm{ambig}} = \sum_{\substack{k=-\infty \\ k\neq 0}}^{\infty} \Bigg[\int_{(f_{dc,n}-0.5B_{d,\mathrm{Rx}})}^{(f_{dc,n}+0.5B_{d,\mathrm{Rx}})} G_{r,n}^2(f+kf_r)\mathrm{d}f + \sum_{m\neq n} \int_{(f_{dc,n}-0.5B_{d,\mathrm{Rx}})}^{(f_{dc,n}+0.5B_{d,\mathrm{Rx}})} G_{r,n}(f+kf_r)G_{r,m}(f+kf_r)\Delta_{nm}\mathrm{d}f \Bigg], \tag{2.62}$$

$$P_{n,\mathrm{sig}} = \int_{(f_{dc,n}-0.5B_{d,\mathrm{Rx}})}^{(f_{dc,n}+0.5B_{d,\mathrm{Rx}})} G_{r,n}^2(f)\mathrm{d}f + \sum_{m\neq n} \int_{(f_{dc,n}-0.5B_{d,\mathrm{Rx}})}^{(f_{dc,n}+0.5B_{d,\mathrm{Rx}})} G_{r,n}(f)G_{r,m}(f)\Delta_{nm}\mathrm{d}f, \tag{2.63}$$

$$\Delta_{nm}(r) = \frac{\int_{(m-n)t_d-\tau_p/2}^{(m-n)t_d+\tau_p/2} G_{el}^2(t-2r/c)\mathrm{d}t}{\int_{-\tau_p/2}^{\tau_p/2} G_{el}^2(t-2r/c)\mathrm{d}t}, \quad n \neq m \tag{2.64}$$

τ_p is the transmitted subpulsewidth, r is the slant range, G_{el} denotes the receiving elevation antenna pattern, and Δ_{nm} is a reduction factor caused by the interbeams suppression (IBS) operation [71]. According to [66], it is sufficient to shape the receiving elevation beam such that the range ambiguities remain below a given level (i.e. -25dB).

2.5 MIMO SAR

MIMO SAR has been first introduced in [72] where it is stated that it is possible to obtain a high resolution wide swath image due to the extra phase centres introduced by the use of the multiple transmitters along with the multiple receiving channels. MIMO SAR can be used in different applications such as the following [44]:

- High resolution wide swath (HRWS) imaging: The number of effective phase centres in MIMO SAR, for the case when the same antenna arrays are used for transmission and reception, is $M + N - 1$ where M and N denote the number of transmitters and receivers, respectively. This allows a further reduction in the PRF which widens the swath for a given azimuth resolution. Throughout this thesis, the application of a HRWS imaging is considered.
- Ground moving target indication (GMTI) [73]: A long virtual array steering vector can be constructed in MIMO SAR using the phase differences among the transmitting antennas along with the receiving antennas. This increases the degrees of freedom which improves the performance of clutter suppression and slowly moving target detection using space-time adaptive processing (STAP).
- Accuracy improvement in height measurement of interferometer [74]

MIMO SAR can be categorised based on the operation schemes [64] as follows:

- Orthogonal waveform encoding MIMO SAR.
- Multiple subband MIMO SAR.
- Beam-space MIMO SAR.

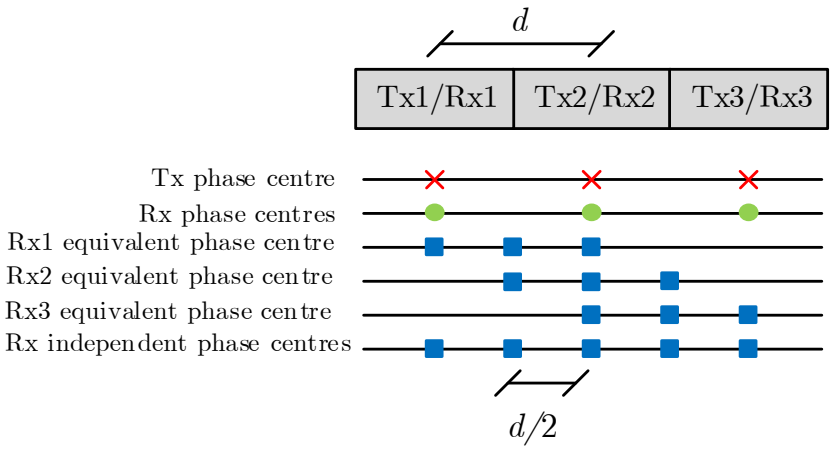

Figure 2.23: *Locations of the phase centres in MIMO SAR. d denotes the separation between the the adjacent receivers.*

2.5.1 Orthogonal Waveform Encoding MIMO SAR

Orthogonal waveform encoding MIMO SAR simultaneously emits multiple orthogonal waveforms into the area to be imaged and the echoes due to the different transmitted waveforms can be separated at the receiver by employing different matched filters. The minimum PRF in MIMO SAR should satisfy the inequality PRF $\geq B_d/K_p$, where B_d denotes the Doppler bandwidth and K_p is the number of independent phase centres which is, for the case that the same antenna arrays are used for transmission and reception, equal to $M + N - 1$ where M and N denote the number of transmitters and receivers, respectively [10]. The locations of the independent phase centres for the case when $M = N = 3$ are as shown in Fig.2.23.

The most challenging issue in this type of MIMO SAR is the design of multiple orthogonal waveforms in such a way that the waveforms are orthogonal to each other regardless of the time delays and Doppler shifts [10][75]. The authors in [76][36] use up and down-chirps to generate a more sophisticated waveform consisting of a sequence of multiple subpulses in such a way that each subpulse is simply a superposition of multiple chirped signals. Short-term shift orthogonal waveforms are proposed in [10] which uses digital beamforming on receive in elevation to suppress distant scatterers. The authors in [77][78] proposed a technique to perfectly separate the echoes corresponding to the transmitted orthogonal waveforms based on echoes compression. The transmitters in this technique, apart from the simultaneous transmissions, are

required to alone emit several times to obtain their private inner-aperture channels after which match filtering is used to concentrate the energy of the solely radiated orthogonal waveforms. MIMO SAR waveforms based on azimuth phase coding (APC) and digital beamforming are proposed in [79] where multiple waveforms are emitted simultaneously. Echoes corresponding to the transmitted waveforms are well separated by implementing azimuth digital beamforming technique.

A detailed analysis of different MIMO radar waveforms is provided in [80]. According to the analysis, time division multiple access (TDMA) waveforms are perfectly orthogonal but this approach suffers from a significant loss of the transmit power. For code division multiple access (CDMA) waveforms, it is not possible to obtain good auto and cross-correlation properties in a single sequence. In frequency division multiple access (FDMA) waveforms, each transmit antenna emits at different carrier frequency. The mere use of FDMA waveforms will restrict the range resolution to correspond to the bandwidth of a single transmitting waveform (i.e. subband waveform) [81][82]. A class of LFM based MIMO waveforms along with DBF in elevation is proposed in [83] which employs short-term shift-orthogonal waveforms, which is described next, in which shifted copies of chirp waveforms that share the same carrier frequency and cover the same bandwidth are used. Echoes due to different transmitted waveforms are separated at the receiver using DBF on receive in elevation and null-steering technique.

Short-term shift-orthogonal waveforms (STSOW) is proposed in [84]. The transmitted signals in this class of waveform is partly orthogonal. For the case of two transmitters, the cross-correlation between the two transmitted signals, x_i and x_j, can be expressed as the following:

$$\int x_i^*(t)x_j(t+\tau)dt = 0 \quad \forall\tau \in \big[-\frac{\tau_p}{2}, \frac{\tau_p}{2}\big], i \neq j \tag{2.65}$$

where τ_p denotes the pulsewidth. One choice of the waveforms that can be used for transmission and satisfy (2.65) is to make x_i a normal up-chirp while x_j a shifted up-chirp. The transmitted signals in the time-frequency plane is shown in Fig.2.24. The cross-correlation between the two transmitted waveforms, , x_i and x_j, is illustrated in Fig.2.25 where it is clear that the two waveforms are almost orthogonal for the mutual time shifts within the interval $\tau \in \big[-\frac{\tau_p}{2}, \frac{\tau_p}{2}\big]$.

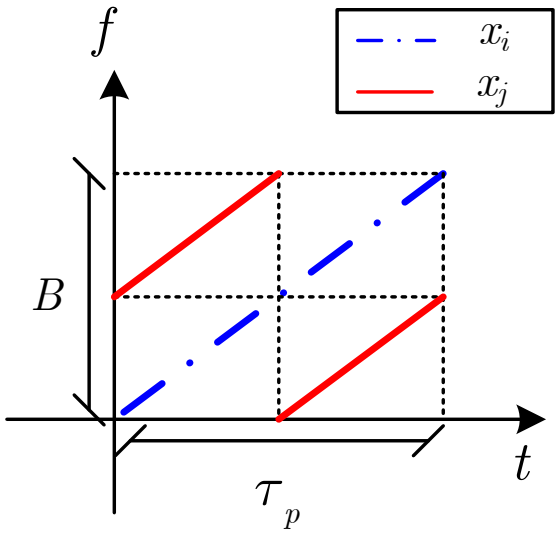

Figure 2.24: *Short-term shift-orthogonal waveforms in the time-frequency plane.*

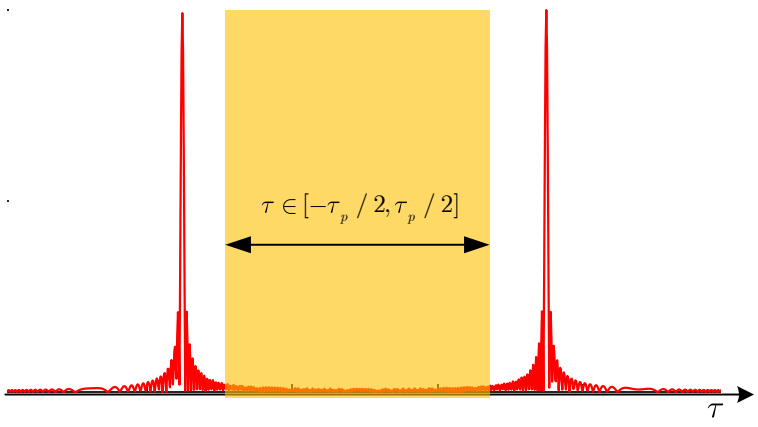

Figure 2.25: *The cross-correlation of the transmitted waveforms x_i and x_j.*

2.5.2 Multiple Subband MIMO SAR

Multiple subband MIMO SAR emits multiple radar waveforms with different carrier frequencies simultaneously [64]. This would allow to increase the transmitted bandwidth significantly and the narrowband assumption is relaxed to the individual transmitted subband. This type of MIMO SAR is mainly used to improve the range resolution instead of obtaining more effective phase centres in the azimuth than that of SIMO SAR.

Most of subband MIMO SAR algorithms in the literature [8] [9] use a bank of bandpass filters (BPFs) at the receiver to separate the subbands. However, the overlapping between the adjacent subbands will affect the performance of the range profile estimation. Therefore, a guard band needs to be added between the adjacent subbands so that they can be separated at the receiver using a bank of BPFs [9] which would affect the bandwidth utilisation efficiency.

2.5.2.1 Received Signal Model

Consider a narrowband MIMO SAR system with an array of M antenna elements at the transmitter and an array of N antenna elements at the receiver. A set of M known subband waveforms (i.e. LFM waveforms) $x_m(t), (\forall m = 1, 2, , ..., M)$ in which each occupies a portion of the total transmitting bandwidth are emitted through the transmitting array. The baseband received signal at the $n\text{th}$ receive antenna can be expressed as

$$y_n(t,\eta) = \sum_{m=1}^{M}\sum_{l=0}^{L-1} \sigma_l e^{-j2\pi F_c \tau_{l,mn}(\eta)} x_m(t - \tau_{l,mn}(\eta)) + w_n(t) \tag{2.66}$$

where,

$$\tau_{l,mn}(\eta) = \frac{R_{l,m}(\eta) + R_{l,n}(\eta)}{c}, \quad \forall m, n = 1, 2, 3 \tag{2.67}$$

$R_{l,m}$ and $R_{l,n}$ are the slant range from the $m\text{th}$ transmitter to the $l\text{th}$ scattering point and from the $n\text{th}$ receiver to the $l\text{th}$ scattering point, respectively, and can be expressed under the assumption of a straight sensor trajectory and approximated using Taylor expansion to the

second order as follows [44]:

$$\begin{aligned} R_{l,n}(\eta) =& \sqrt{R_l^2 + (v_p\eta + (N-1-n)d)^2 - 2R_l v_p \eta \sin(\theta_n)} \\ &\approx R_l - v_p \sin(\theta_n)(\eta + (N-1-n)\frac{d}{v_p}) + \frac{v_p^2 \cos^2(\theta_n)(\eta + (N-1-n)d/(v_p))^2}{2R_l} \end{aligned} \tag{2.68}$$

where v_p is the platform velocity, d is the separation between the adjacent transmitters/receivers, θ_n denotes the squint angle of the nth receiver, and R_l is the slant range to the lth scatterer when $\eta = 0$ (i.e. the slant range of the closest approach). Quadratic approximation of $R_{l,m}(\eta) + R_{l,n}(\eta)$ can be expressed as the following (see Appendix A for the derivation):

$$R_{l,m}(\eta) + R_{l,n}(\eta) \approx 2R_{l,m}(\eta - \frac{\Delta y_{mn}}{2v_p})_{\theta=\theta_n} + \frac{\Delta y_{mn}^2}{4R_l} \tag{2.69}$$

where Δy_{mn} denotes the separation between the mth transmitter and the nth receiver. The azimuth impulse response $h_{az,mn}$ when the signal is transmitted by the mth transmitter and received by the nth receiver is determined by the distance of the transmit and receive path, which can be expressed as

$$h_{az,mn}(\eta) = e^{-j\frac{2\pi}{\lambda}(R_{l,m}(\eta) + R_{l,n}(\eta))} \tag{2.70}$$

The received signal in (2.66) is sampled from the range cell that corresponds to the near range to the range cell that corresponds to the far range with a sampling frequency of $f_s = 1/T_s$. The signals are also sampled in the azimuth dimension with a sampling frequency of $f_p = \mathrm{PRF}$. The discrete time version of the received signal can be expressed as follows:

$$z_n[n_t, n_a] = \sum_{l=0}^{L-1} h_{mn}[l, n_a] x_m[n_t - l] + w_n[n_t] \tag{2.71}$$

where,

$$\begin{aligned} h_{mn}[l, n_a] =& \sigma_l e^{-j2\pi F_c \tau_{l,mn}(n_a)} \\ =& \sigma_l e^{j\phi_{l,mn}(n_a)} \end{aligned} \tag{2.72}$$

n_t and n_a are the range and azimuth time indices, respectively. This received signal model will be used throughout the thesis.

2.5.3 Beam-space MIMO SAR

Beam-space MIMO SAR [85][86] shown in Fig.2.26 is used to obtain a high resolution ultra-wide swath imaging by concurrently emitting a sequence of subpulses in a PRI by multiple transmitters. Different subswaths, at a given time, are illuminated by different subapertures in azimuth and DBF on receive in elevation is used to separate the echoes due to different transmitted subpulses by exploiting the one-to-one relation between the delay and the receiving angle in the side-looking radar geometry. It should be noted that the emitted radar subpulses have the same waveform encoding and share the same carrier frequency. Beam-space MIMO SAR is usually incorporated with burst imaging mode such as Scan SAR in order to image the blind area between different subswaths as shown in Fig.2.26. The main disadvantage of this mode is the high complexity of implementation [64].

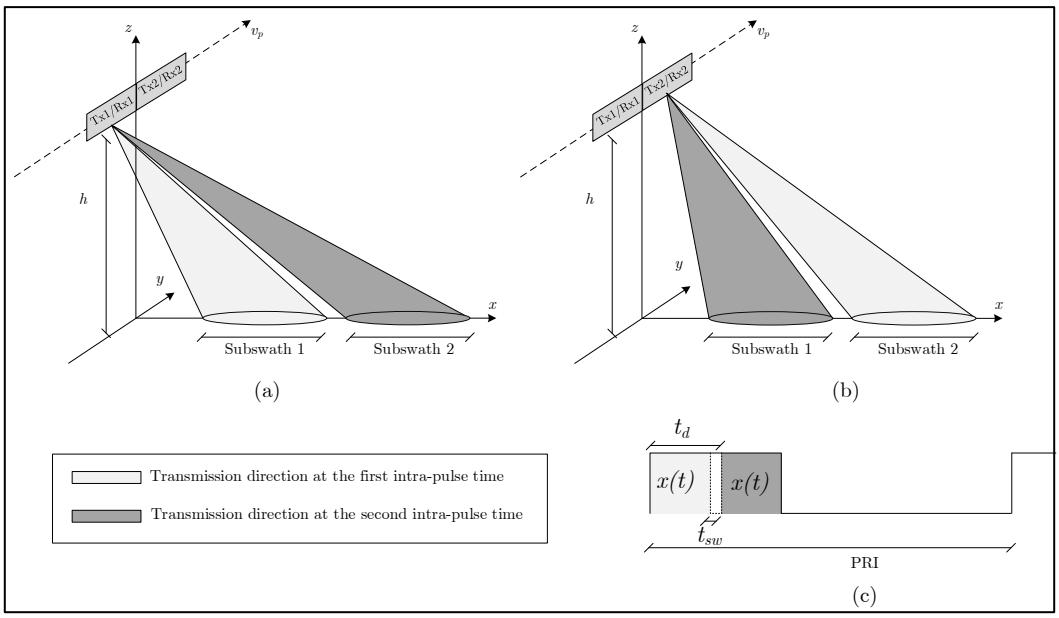

Figure 2.26: *Beam-space MIMO SAR configuration.(a) Transmission directions sequence of the* 1st *transmitter. (b) Transmission directions sequence of the* 2nd *transmitter. (c) Timing structure of a single* PRI *transmitted by the* mth *transmitter where* t_d*, and* t_{sw} *denote the delay between the subsequent transmitted subpulses and the beam switching time, respectively.*

2.5.4 MIMO SAR Technical Challenges

One of the fundamental challenges in MIMO SAR is the orthogonality between the different transmtted signals which needs to be ensured for arbitrary shifts [84][10] in orthogonal waveform encoding MIMO SAR. The orthogonality can be ensured if the waveforms are transmitted at different times and/or with different frequencies. However, this is not desirable for geophysical measurement [84]. Many mutual orthogonal waveforms are proposed in the literature which cover the same frequency band [7][75][76] but the signal energy after range focusing from all unmatched waveforms is still present in the focused signal. Moreover, the smeared energy (i.e. which can be seen as noise) from the unmatched waveforms may even exceed the energy of the focused image response depending on the number of the transmitted waveforms. A solution to this challenge is to employ short-term shift orthogonal waveforms described previously along with DBF on receive in elevation [10]. One other solution which is recently proposed in the literature [87] is based on a segmented phase code (SPC) waveform in which the separation of the echoes from close elevation arrival angles is done using a simple time-shift weighting processing while the echoes received from far elevation angles are separated using a range bandpass filter in addition to a DBF technique.

One of the other challenges is motion errors due to the presence of the atmospheric turbulence which causes deviations of the platform trajectory from the nominal positions as well as altitude. This error needs to be eliminated in order to meet the quality requirement of the high resolution SAR image [88]. High-precision navigation systems such as on-board global positioning system (GPS) and inertial navigation units (INUs) are used to account for such errors [41]. If such systems are not reachable, signal processing-based motion compensation methods are applied [89][90][91]. Throughout the thesis, a straight sensor trajectory is assumed (i.e. the motion error is assumed to be compensated for).

2.6 Preliminary Study on System Identification Formulation of MIMO Radar

A preliminary study on formulating MIMO radar as a system identification problem is described. Next, an FDSI-based estimation algorithm is proposed to estimate the range profile instead of a matched filter. The proposed algorithm allows the use of partially correlated waveforms (i.e. LFM waveforms) and the sidelobes in the estimated range profile are ideally zero

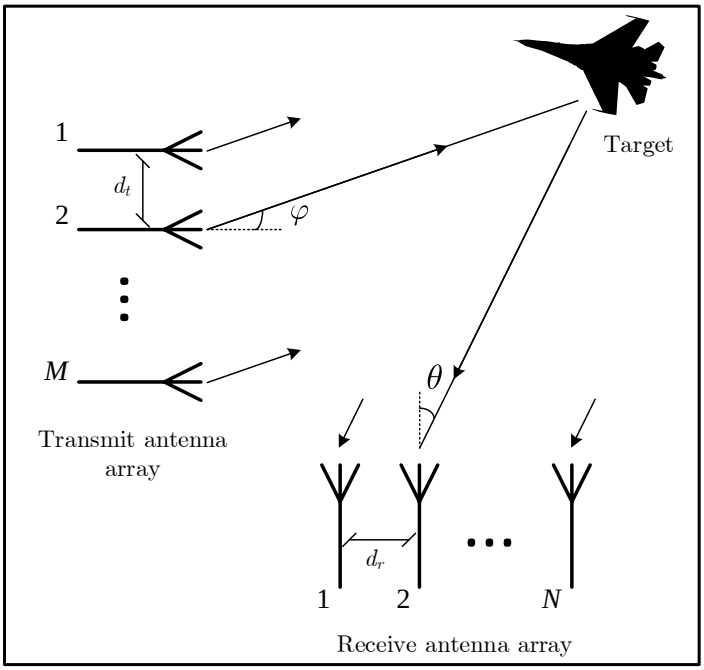

Figure 2.27: *MIMO radar configuration. φ and θ denote the angle of departure and angle of arrival, respectively. d_t and d_r are the separation between the transmitting and receiving antenna elements, respectively.*

which is the property of IRCI-free. In addition, the length of the transmitted waveform is not a function of the channel impulse response to be estimated and the narrowband assumption is relaxed to the bandwidth of a single transmitted waveform. This preliminary study is published in [13].

2.6.1 Received Signal Model

Consider a narrowband MIMO radar system with an array of M antenna elements at the transmitter and an array of N antenna elements at the receiver as shown in Fig.2.27. A set of M known subband waveforms (i.e. LFM waveforms) $x_m(t), (\forall m = 1, 2, , ..., M)$ in which each occupies a portion of the total transmitting bandwidth are emitted through the transmitting array. The baseband signals reflected from a target located at the position (φ, θ) and received at

all receiving antennas can be expressed in a vector form as follows:

$$\begin{aligned}\mathbf{y}(t) &= [y_1(t), y_2(t), ..., y_N(t)]^T \\ &= [e^{-j2\pi F_c \beta_1}, ..., e^{-j2\pi F_c \beta_N}]^T u(t) + [w_1(t), ..., w_N(t)]^T \\ &= \mathbf{a}_r(\theta)u(t) + \mathbf{w}(t)\end{aligned} \tag{2.73}$$

where,

$$u(t) = \sum_{m=1}^{M} \sum_{l=0}^{L-1} \sigma_l e^{-j2\pi F_c \tau_l} x_m(t - \tau_l) e^{-j2\pi F_c \gamma_m} \tag{2.74}$$

$y_n(t), \forall (n = 1, 2, ..., N)$ is as defined in (2.6) and $\mathbf{a}_r(\theta)$ is the receiving array manifold vector. The received signal after DBF can be expressed as

$$\begin{aligned}z(t) &= \mathbf{a}_r^H(\theta)\mathbf{y}(t) \\ &= \mathbf{a}_r^H(\theta)\mathbf{a}_r(\theta)u(t) + \mathbf{a}_r^H(\theta)\mathbf{w}(t) \\ &= Nu(t) + v(t) \\ &= N \sum_{l=0}^{L-1} \sigma_l e^{-j2\pi F_c \tau_l} \underbrace{\mathbf{a}_t^T(\varphi)\mathbf{x}(t - \tau_l)}_{b(t-\tau_l)} + v(t)\end{aligned} \tag{2.75}$$

where $\mathbf{a}_t(\varphi)$ denotes the transmitting array manifold vector and can be expressed as follows:

$$\mathbf{a}_t(\varphi) = [e^{-j2\pi F_c \gamma_1}, ..., e^{-j2\pi F_c \gamma_M}]^T \tag{2.76}$$

2.6.2 Impulse Response Estimation

It is assumed that the set of transmitted waveforms $\mathbf{x}(t)$ are not perfectly orthogonal. Thus, there might be some overlapping in the frequency domain. In our case, a set of LFM waveforms are used in such a way that each LFM waveform occupies a subband of the total available spectrum. The received signal in (2.75) is sampled from the range cell that corresponds to the minimum range to the range cell that corresponds to the maximum range with a sampling frequency f_s so that the discrete time version of the received signal can be expressed as

$$z[n] = N \sum_{l=0}^{L} h[l]b[n - l] + v[n], \quad 0 \leq n < K + L - 1 \tag{2.77}$$

where K is the length of the waveform transmitted and $h[l]$ is the channel impulse response that needs to be estimated which can be expressed as

$$h[l] = \sigma_l e^{-j2\pi f_c l T_s} \tag{2.78}$$

where $T_s = 1/f_s$ is the sampling interval. The discrete time received signal in (2.77) can be written in a matrix form as

$$\begin{aligned} \mathbf{z} &= \big[z[0], z[1], ..., z[K+L-1]\big]^T \\ &= N\mathbf{B}\mathbf{h} + \mathbf{v} \end{aligned} \tag{2.79}$$

where,

$$\mathbf{h} = \big[h[0], h[1], ..., h[L-1]\big]^T \tag{2.80}$$

$$\mathbf{v} = \big[v[0], ..., v[K+L-1]\big]^T \tag{2.81}$$

the matrix $\mathbf{B}$ is of dimension $(K+L-1) \times L$ which can be expressed as

$$\mathbf{B} = \begin{bmatrix} b[0] & 0 & \dots & \dots & 0 \\ b[1] & b[0] & & & 0 \\ \vdots & b[1] & \ddots & & \vdots \\ b[K-1] & \vdots & \vdots & \ddots & 0 \\ 0 & b[K-1] & & & b[0] \\ 0 & 0 & \ddots & \vdots & b[1] \\ \vdots & \vdots & & \ddots & \vdots \\ 0 & 0 & \dots & 0 & b[K-1] \end{bmatrix} \tag{2.82}$$

If the angle of departure (φ) is known at the receiver, the matrix $\mathbf{B}$ can be computed at the receiver and the impulse response $\mathbf{h}$ can be estimated in the same way as described in Section 2.3.2.4. The FDSI-based impulse response estimation algorithm will be used in all of the proposed MIMO SAR configurations in the thesis to demonstrate the performance of the algorithm for the case when the input SAR signal has a non-flat spectrum.

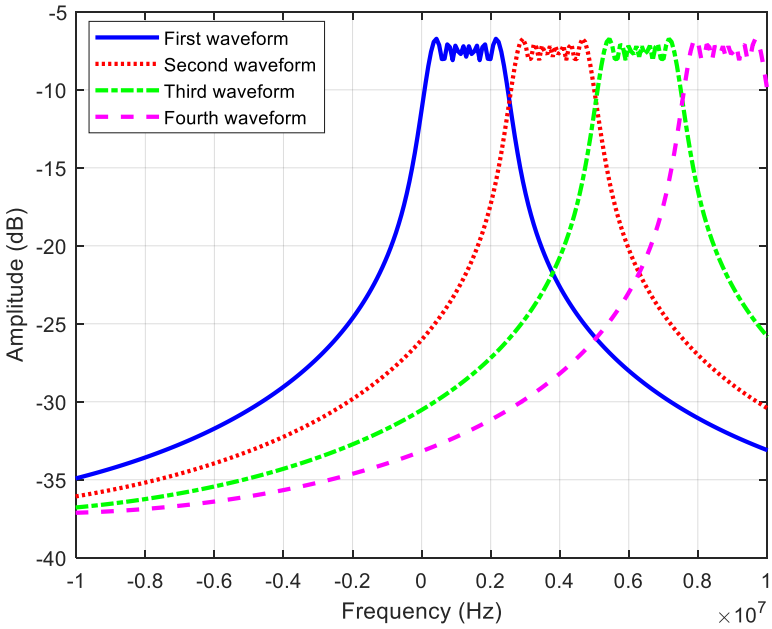

Figure 2.28: *The spectra of the transmitted waveforms.*

2.6.3 Simulation Results

The following subsection shows the numerical results of our proposed frequency domain system identification estimation algorithm for MIMO radar using a set of partially correlated LFM waveforms and compare it with the results obtained using the CP-OFDM based waveforms [4]. We then show the effect of the DBF pointing error on the performance of the proposed method. It is assumed in the simulation that the Doppler shift in the received signal when the target moves has been compensated for at the receiver. The effect of the Doppler estimation error is the same as the effect of DBF pointing error which is considered in one of the scenarios.

2.6.3.1 Performance of Range Profile Reconstruction

Assume there are $M = 4$ transmit antennas, $N = 4$ receive antennas and both of the transmit and receive arrays are uniform linear arrays with a half wavelength element spacing. The channel impulse response length is assumed to be $L = 256$ which corresponds to the tracking zone. The spectra of the transmitted waveforms are shown in Fig.2.28 in which each waveform occupies a subband of $2.5MHz$ and the total bandwidth of the receiver is $B_{tot} = M \times 2.5MHz = 10MHz$. Accordingly, the range resolution of the system should be $15m$. In order to demon-

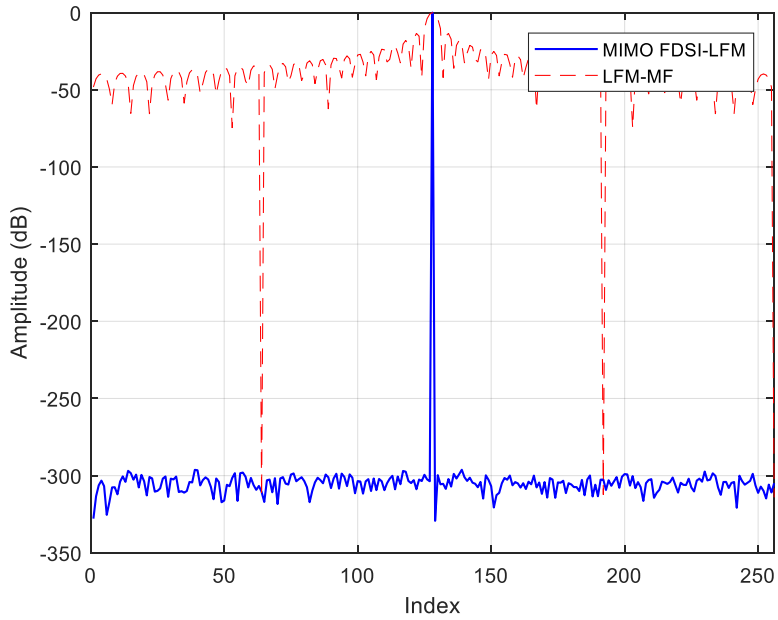

Figure 2.29: *The normalised point spread function of MIMO-FDSI method and LFM-MF method for the case when a scatterer falls exactly in the range cell.*

strate the free interrange cell interference property of the proposed method, we compare the point spread function of the proposed method with the conventional LFM waveform with a bandwidth of $10MHz$ using matched filter for the case when a scatterer falls exactly in the range cell as shown in Fig.2.29. In addition, the point spread function when the scatterer falls between two range cells is shown in Fig.2.30. In both cases, the proposed FDSI-based algorithm outperforms the matched filter. This is because the FDSI-based algorithm takes into account the fact that the spectrum of the combined signal is not flat unlike the case of the matched filter which assumes a flat spectrum.

Next, consider a scenario in which there is a target that occupies four range cells in which the width of each range cell is $15m$ which corresponds to the range resolution using the total bandwidth B_{tot}. The estimated channel impulse response for an $\mathrm{SNR} = 10\mathrm{dB}$ is shown in Fig.2.31 where it is obvious that the range profile is recovered perfectly.

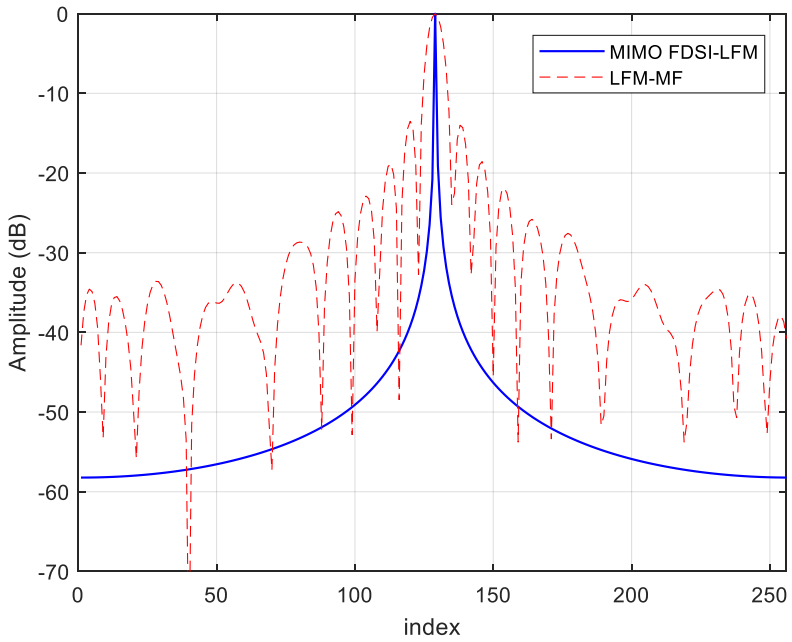

Figure 2.30: *The normalised point spread function of MIMO-FDSI method and LFM-MF method for the case when a scatterer falls between two range cells*

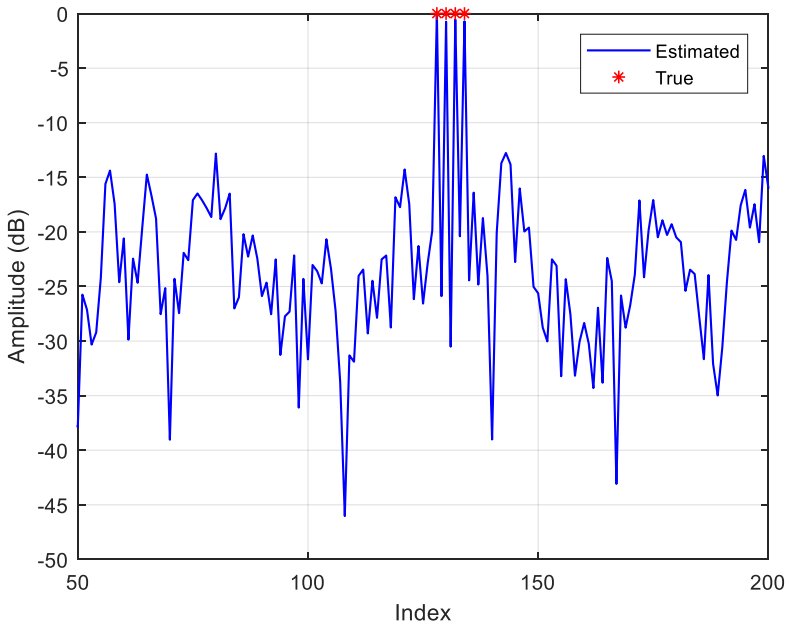

Figure 2.31: *Estimated range profile for the case of an extended target.*

2.6.3.2 Influences of Transmit and Receive DBF Errors

Consider the simulation parameters in section 2.6.3.1. The error in the estimation of the angle of arrival will cause a degradation in the SNR because the full gain of the array is not obtained.

Suppose that the transmit DBF pointing error is $(\Delta\theta = 2^o)$ and there is a point target located in the 128th range cell. Our proposed MIMO-FDSI method will be compared with the CP-OFDM method described in [40]. The total number of subcarriers used in CP-OFDM method is $N_s = 256$ which corresponds to the channel length L. Each transmit antenna uses $N_0 = 64$ subcarriers. The length of the cyclic prefix should be at least equal to $(L-1) = 255$ which is the one used in the simulation in order to prevent the range cell interference. In addition, Zadoff-Chu sequences [40] defined below are used as the weighting coefficients for the subcarriers in the discrete frequency domain.

$$W_m(k) = \begin{cases} \sqrt{M}e^{j\phi_{m,p}} & , k = Mp + m \text{ for some integer } p \text{ with } 0 \leq p < N_0 \\ 0 & , \text{else} \end{cases} \tag{2.83}$$

where,

$$\phi_{m,p} = -\frac{\pi}{N_0}(p + \langle N_0 \rangle_2)\mu_m p \tag{2.84}$$

$k \in [0, N_s - 1]$ and μ_m is a positive integer less than and relatively prime to N_0. The use of a cyclic prefix does not allow full utilisation of the transmitted energy as it is removed at the receiver. The spectra of the transmitted waveforms used in the proposed MIMO-FDSI are shown in Fig.2.28. The estimated range profile using both methods is illustrated in Fig.2.32 for the case when the SNR is 40dB where it is clear that our proposed method exhibits robustness to the pointing error unlike the CP-OFDM method which produces spurious peaks.

The robustness of our proposed algorithm to the DBF pointing error is studied by counting the average number of spurious peaks whose levels exceed a certain threshold, which has been chosen to be slightly above the noise level, for different SNRs at different DBF pointing errors as shown in Fig.2.33 in which the number of Monte-Carlo simulation runs is 1000. The results in Fig.2.33 are expected because the spurious peaks are greater than the noise floor for high SNR and they will be below the noise floor as the SNR gets lower. In addition, It is obvious from Fig.2.33 that our proposed algorithm is shown to have no spurious peaks above the noise floor as long as the pointing error is below 3^o.

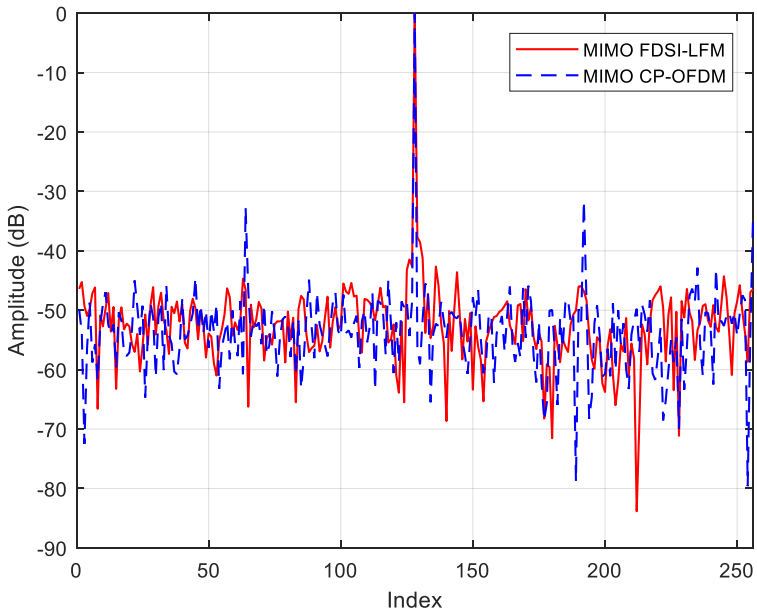

Figure 2.32: *Estimated range profile for the case of DBF pointing error using MIMO-FDSI method and CP-OFDM method for an SNR of 40dB.*

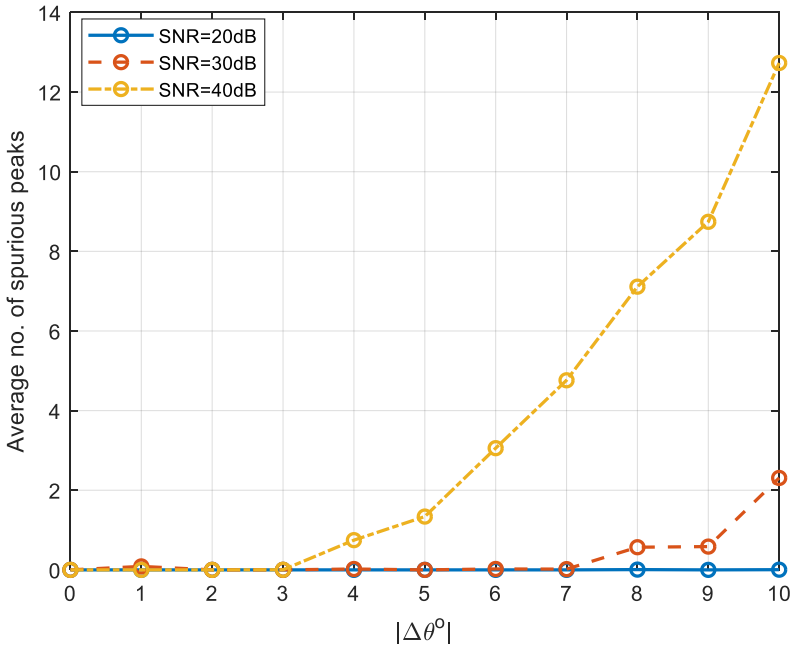

Figure 2.33: *The average number of spurious peaks at different DBF pointing errors.*

2.7 Summary

SIMO SAR and MIMO SAR have been proposed in the literature to address the tradeoff between the desired wide swath width and high cross-range resolution in conventional stripmap SISO SAR. Most of the multiple subband MIMO SAR algorithms in the literature use a bank of bandpass filters at the receiver to separate the subbands but the overlapping between the adjacent subbands will affect the performance of the range profile estimation. Therefore, a guard band needs to be added between the adjacent subbands so that they can be separated at the receiver which would affect the bandwidth utilisation efficiency. The main application of multiple subband MIMO SAR is to improve the range resolution by transmitting more bandwidth while the narrowband assumption is relaxed to the individual transmitted subband. Orthogonal waveform encoding MIMO SAR provides more effective phase centres than SIMO SAR and the minimum PRF should satisfy the inequality PRF $\geq B_d/K_p$ where B_d denotes the Doppler bandwidth and K_p is the number of independent phase centres which is, for the case that the same antenna arrays are used for transmission and reception, equal to $M + N - 1$ where M and N denote the number of transmitters and receivers, respectively. Most of MIMO SAR algorithms employ a bank of matched filters to separate the echoes corresponding to different orthogonal transmitted waveforms but the matched filter is optimal for detection which is not the case in SAR imaging as it is desired to reconstruct the range profile from the received signal. Accordingly, an alternative method based on FDSI will be employed in MIMO SAR as will be presented in later chapters.

Chapter 3
Bandpass-Filter Based Multiple Subband IRCI-Free MIMO SAR

3.1 Introduction

In this chapter, we propose a new bandpass filters based multiple subband technique based on frequency domain system identification (FDSI) to estimate the channel impulse response in the range dimension for MIMO SAR. The estimated range profile has the property of IRCI-free. In addition, a low pulse repetition frequency (PRF) which is less than the Doppler bandwidth is used to obtain a wide swath and the resulted Doppler aliasing is recovered using a set of spatial filters. Two modes of operation are considered, namely, stripmap MIMO SAR ($A = 1$) and sliding spotlight MIMO SAR ($0 < A < 1$). It is worth pointing out that the proposed FDSI-based estimation algorithm, in this chapter, will be used to estimate the range profile in all proposed configurations in the thesis.

This chapter is divided into sections. Section 3.2 describes how the azimuth ambiguity is removed when the PRF used is lower than the Doppler bandwidth and Section 3.3 provides the derivation of the proposed FDSI-based algorithm to estimate the impulse response in the range dimension. Finally, simulated data is used in Section 3.4 to validate the effectiveness of the proposed algorithm. The last section summarises the chapter. The results of this chapter were published in [14] and [15].

3.2 Azimuth Ambiguity Removal

Consider a narrowband sliding spotlight MIMO SAR geometry with an array of M antenna elements at the transmitter and an array of N antenna elements at the receiver as shown in Fig.3.1 where the radar beams are steered during the illumination time towards the point O located beyond the centre of the imaging scene.

Using the received signal model described in Section 2.5.2.1, the discrete time version of the

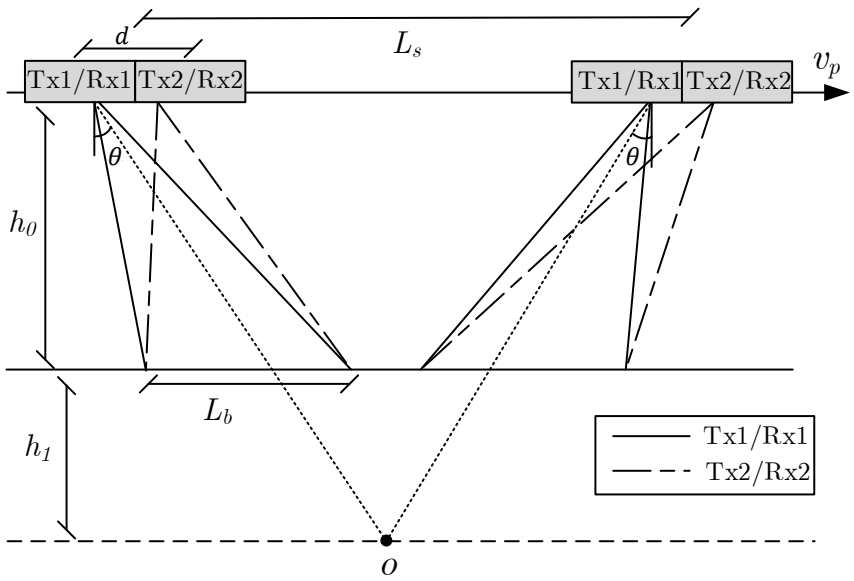

Figure 3.1: *Sliding spotlight MIMO SAR geometry. h_0 denotes the platform height, h_1 is the shortest distance between the scene and the focus point, v_p denotes the platform velocity. L_s and L_b denote the synthetic aperture length and antenna footprint length on the ground, respectively.*

received signals for the case when $M = N = 2$ as shown in Fig.3.1 (i.e. the squint angles for all beams are zeros) can be expressed as the following:

$$z_1[n_t, n_a] = \sum_{l=0}^{L-1} h_{11}[l, n_a]x_1[n_t - l] + \sum_{l=0}^{L-1} h_{21}[l, n_a]x_2[n_t - l] + w_1[n_t] \tag{3.1}$$

$$z_2[n_t, n_a] = \sum_{l=0}^{L-1} h_{12}[l, n_a]x_1[n_t - l] + \sum_{l=0}^{L-1} h_{22}[l, n_a]x_2[n_t - l] + w_2[n_t] \tag{3.2}$$

The azimuth ambiguity removal will be performed in the frequency domain. It is based on the concept of the multi-aperture reconstruction algorithm which is a generalisation of the sampling theorem which has been applied in SIMO SAR case in [72]. The algorithm states that if there are N independent representations of the signal and the sampling frequency is $1/N\text{th}$ the signal Nyquist frequency, it is possible to reconstruct the original signal from the aliased spectra of the N representations.

The Fourier transform of (3.1) and (3.2) across both azimuth and range dimensions can be expressed as the following:

$$Z_1(f_r, f_a) = \underbrace{X_1(f_r)H_{11}(f_r, f_a)}_{Y_{11}(f_r,f_a)} + \underbrace{X_2(f_r)H_{21}(f_r, f_a)}_{Y_{21}(f_r,f_a)} + W_1(f_r) \tag{3.3}$$

$$Z_2(f_r, f_a) = \underbrace{X_1(f_r)H_{12}(f_r, f_a)}_{Y_{12}(f_r,f_a)} + \underbrace{X_2(f_r)H_{22}(f_r, f_a)}_{Y_{22}(f_r,f_a)} + W_2(f_r) \tag{3.4}$$

After passing the received signals in (3.3) and (3.4) through a bank of band pass filters, the received signals at different frequency subbands can be separated and reexpressed using the principle of DPC [44] as the following (the noise is not included in the following equations and the transmitted waveforms can be passed through a bank of bandpass filters on transmit so that

they can be separated at the receiver):

$$
\begin{aligned}
Y_{11}(f_r, f_a) &= X_1(f_r)H_{11}(f_r, f_a) \\
&= \underbrace{X_1(f_r)H_{12}(f_r, f_a)}_{U_1(f_r,f_a)} \underbrace{e^{j\frac{\pi d f_a}{v_p}} e^{j\frac{\pi d^2}{2\lambda R_l}}}_{Q_1(f_a)} \qquad (3.5)
\end{aligned}
$$

$$
Y_{12}(f_r, f_a) = \underbrace{X_1(f_r)H_{12}(f_r, f_a)}_{U_1(f_r,f_a)} \times \underbrace{1}_{Q_2(f_a)} \qquad (3.6)
$$

$$
Y_{21}(f_r, f_a) = \underbrace{X_2(f_r)H_{21}(f_r, f_a)}_{U_2(f_r,f_a)} \times \underbrace{1}_{Q_3(f_a)} \qquad (3.7)
$$

$$
\begin{aligned}
Y_{22}(f_r, f_a) &= X_2(f_r)H_{22}(f_r, f_a) \\
&= \underbrace{X_2(f_r)H_{21}(f_r, f_a)}_{U_2(f_r,f_a)} \underbrace{e^{-j\frac{\pi d f_a}{v_p}} e^{j\frac{\pi d^2}{2\lambda R_l}}}_{Q_4(f_a)} \qquad (3.8)
\end{aligned}
$$

The received signals are aliased in the azimuth dimension because it is assumed that $\mathrm{PRF} < B_d(= 2\mathrm{PRF})$ as illustrated in Fig.3.2. The output of the bandpass filters are expressed as a function of $H_{12} = H_{21}$ which corresponds to the impulse response of a SISO case in which the effective phase centre is located midway between the two transmitters. $U_1(f_r, f_a)$ corresponds to a single subband and will be perfectly reconstructed from the aliased signals in the azimuth dimension expressed in (3.5) and (3.6). Similarly, $U_2(f_r, f_a)$ corresponds to the other subband and will be reconstructed from the aliased signals in the azimuth dimension expressed in (3.7) and (3.8). The reconstruction of $U_1(f_r, f_a)$ will be now considered and the same technique will be applied to reconstruct $U_2(f_r, f_a)$. The aliased signals of $Y_{11}(f_r, f_a)$ and $Y_{12}(f_r, f_a)$ can be expressed as the following:

$$
\begin{aligned}
\tilde{Y}_{mn}(f_r, f_a) &= \sum_{k=-\infty}^{\infty} Y_{mn}(f_r, f_a + kf_p) \\
&= \sum_{k=-\infty}^{\infty} U_m(f_r, f_a + kf_p) Q_{n+2(m-1)}(f_a + kf_p) \qquad (3.9)
\end{aligned}
$$

It is possible to weight and combine $\tilde{Y}_{11}(f_r, f_a)$ and $\tilde{Y}_{12}(f_r, f_a)$ in such a way that the original spectrum $U_1(f_r, f_a)$ is recovered while the back-folded component is removed as expressed in the following equations for the intervals I_1 and I_2 in Fig.3.2 (P_{ni} denotes the reconstruction

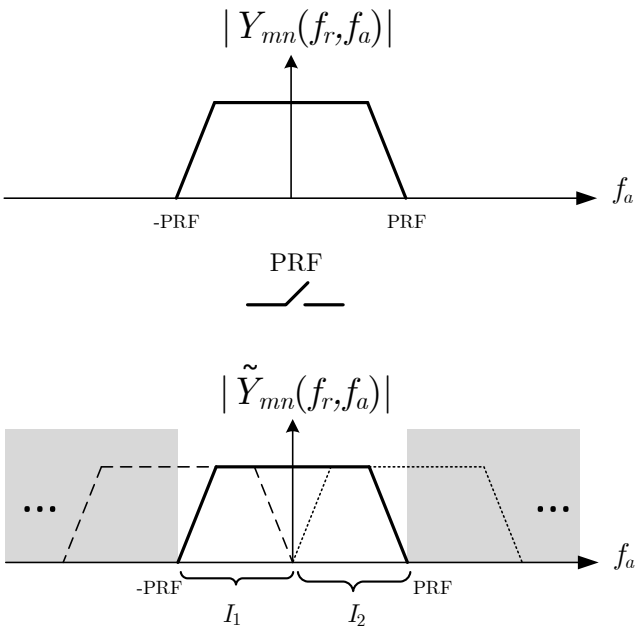

Figure 3.2: *The spectrum at the* nth *receiver when the signal is transmitted by the* mth *transmitter.* B_d *is assumed to be* 2PRF.

filter for the nth receiver on the ith Doppler frequency interval):

$$P_{11}(f_a)U_1(f_r,f_a)Q_1(f_a)+P_{21}(f_a)U_1(f_r,f_a)Q_2(f_a)=2U_1(f_r,f_a) \tag{3.10}$$

$$P_{11}(f_a)U_1(f_r,f_a+f_p)Q_1(f_a+f_p)+P_{21}(f_a)U_1(f_r,f_a+f_p)Q_2(f_a+f_p)=0 \tag{3.11}$$

For interval I_2 after shifting to I_1 to allow for setting up the linear systems of (3.14).

$$\begin{aligned}&P_{12}(f_a+f_p)U_1(f_r,f_a+f_p)Q_1(f_a+f_p)+P_{22}(f_a+f_p)U_1(f_r,f_a+f_p)Q_2(f_a+f_p)\\&=2U_1(f_r,f_a+f_p)\end{aligned} \tag{3.12}$$

$$P_{12}(f_a+f_p)U_1(f_r,f_a)Q_1(f_a)+P_{22}(f_a+f_p)U_1(f_r,f_a)Q_2(f_a)=0 \tag{3.13}$$

The reconstruction filters can be computed as the following:

$$\mathbf{P}(f_a)=2\mathbf{Q}^{-1}(f_a) \tag{3.14}$$

where,

$$\mathbf{Q}(f_a) = \begin{bmatrix} Q_1(f_a) & Q_2(f_a) \\ Q_1(f_a + f_p) & Q_2(f_a + f_p) \end{bmatrix} \tag{3.15}$$

$$\mathbf{P}(f_a) = \begin{bmatrix} P_{11}(f_a) & P_{12}(f_a + f_p) \\ P_{21}(f_a) & P_{22}(f_a + f_p) \end{bmatrix} \tag{3.16}$$

I_2 is then concatenated with I_1 to obtain the original spectrum $U_1(f_r, f_a)$. Similarly, the original spectrum $U_2(f_r, f_a)$ is reconstructed.

The reconstructed signals in different range frequency subbands are superimposed to obtain the full bandwidth signal in range frequency domain.

$$\begin{aligned} U(f_r, f_a) &= U_1(f_r, f_a) + U_2(f_r, f_a) \\ &= \underbrace{(X_1(f_r) + X_2(f_r))}_{B(f_r)} H_{12}(f_r, f_a) + W(f_r) \end{aligned} \tag{3.17}$$

For the case of sliding spotlight SAR mode, the azimuth bandwidth of $U(f_r, f_a)$ is now $B_{overall}$ which is greater than $N\mathrm{PRF}$ so the signal in (3.17) needs to go through an azimuth filter to perform deramping [68]. The azimuth filter can be expressed as the following:

$$g(\eta) = e^{j\pi \frac{2v_p^2\eta^2}{\lambda(h_0+h_1)}} \tag{3.18}$$

The signal in (3.17) after deramping and azimuth dechirp residue compensation can be expressed as the following:

$$U_d(f_r, f_a) = \underbrace{(X_1(f_r) + X_2(f_r))}_{B(f_r)} H_{d,12}(f_r, f_a) + W(f_r) \tag{3.19}$$

where $H_{d,12}(f_r, f_a)$ is the frequency impulse response that needs to be estimated after deramping. The azimuth bandwidth is now less than or equal to $N\mathrm{PRF}$. It should be noted that there is no need for deramping for the case of stripmap SAR mode. A schematic of the proposed configuration implementation is shown in Fig.3.3

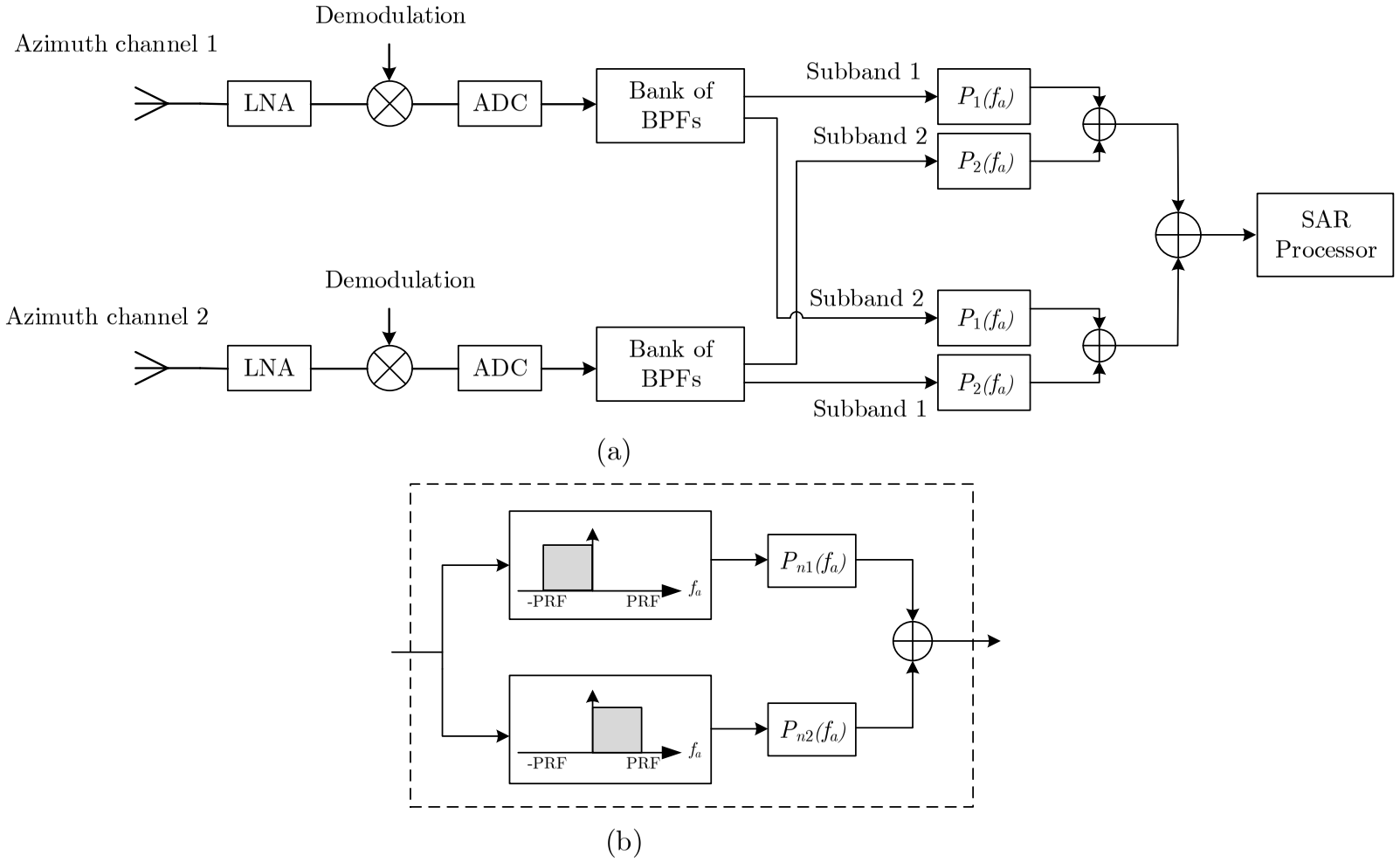

Figure 3.3: *(a)A schematic of the proposed configuration implementation. (b) A schematic of the spatial filters bank* $P_n(f_a)$ *which is computed using* (3.14)*. Image formation algorithm is performed in SAR processor block.*

3.3 Impulse Response Estimation and Image Formation

Without loss of generality, chirp scaling (CS) algorithm described in Section 2.3.4.1 is used for image formation. The estimation of the range impulse response at every Doppler frequency using our proposed FDSI-based estimation algorithm is described next. The scaled received signal (i.e. after the multiplication with the first chirp scaling function) can be expressed as the following:

$$u_s(n_t, f_a) = \sum_{l=0}^{L-1} h_{d,12}[l, f_a] b_s[n_t - l, f_a] + w_s(n_t, f_a)$$
$$0 \leq n_t \leq K + L - 1 \tag{3.20}$$

where K is the length of the waveform transmitted, $w_s(n_t, f_a)$ is the noise after being multiplied with $H_{\mathrm{CS},1}$ in the range-Doppler domain and $b_s[n_t, f_a]$ is the combined transmitted chirps but with a new chirp rate which varies with the Doppler frequency as given below

It is worth pointing out that the proposed FDSI-based algorithm is particularly appropriate for the range profile estimation because the fact that the spectrum of $b_s[n_t, f_a]$ is non-flat is considered which makes the range profile estimation performance better than the one obtained using the matched filter (i.e. which assumes a flat spectrum). The received signal in (3.20) can be written in a matrix form for a given Doppler frequency (f_a) as the following:

$$\begin{aligned}\mathbf{u}_s(f_a) &= \left[u_s[0, f_a], u_s[1, f_a], ..., u_s[K + L - 1, f_a]\right]^T \\ &= \mathbf{B}_s(f_a)\mathbf{h}_{d,12}(f_a) + \mathbf{w}_s(f_a)\end{aligned} \tag{3.21}$$

where,

$$\mathbf{h}_{d,12}(f_a) = \left[h_{d,12}[0, f_a], h_{d,12}[1, f_a], ..., h_{d,12}[L - 1, f_a]\right] \tag{3.22}$$
$$\mathbf{w}_s(f_a) = \left[w_s[0, f_a], ..., w_s[K + L - 1, f_a]\right]^T \tag{3.23}$$

$$\mathbf{B}_s(f_a) = \begin{bmatrix} b_s[0,f_a] & 0 & \dots & \dots & 0 \\ b_s[1,f_a] & b_s[0,f_a] & & & 0 \\ \vdots & b_s[1,f_a] & \ddots & & \vdots \\ b_s[K-1,f_a] & \vdots & \vdots & \ddots & 0 \\ 0 & b_s[K-1,f_a] & & & b_s[0,f_a] \\ 0 & 0 & \ddots & \vdots & b_s[1,f_a] \\ \vdots & \vdots & & \ddots & \vdots \\ 0 & 0 & \dots & 0 & b_s[K-1,f_a] \end{bmatrix}$$

The estimation of $\mathbf{h}_{d,12}(f_a)$ at every Doppler frequency can be performed as explained in Section 2.3.2.4. Next, the bulk RCMC and azimuth compression are performed to obtain the final image.

3.4 Simulation Results

This section shows the simulations results of the following two multiple subband MIMO SAR modes:

- Stripmap SAR
- Sliding spotlight SAR

In all simulation scenarios, the results of the proposed FDSI-MIMO SAR are compared with the ones obtained using matched filter (MF) based MIMO SAR and the conventional SISO SAR, which has the same simulation parameters as the corresponding MIMO SAR but with the number of transmitter (M) = number of receiver (N) = 1 . The spectra of the LFM transmitted waveforms in this section are as shown in Fig.3.4.

3.4.1 Azimuth Ambiguity Removal

3.4.1.1 Stripmap SAR

Consider the simulation parameters listed in Table.3.1. In addition, the Doppler bandwidth (B_d) and the PRF are $200Hz$ and $100Hz$, respectively. Assume that there is a single scatterer located at the swath centre. The azimuth and range cuts of the formed image at the scatterer

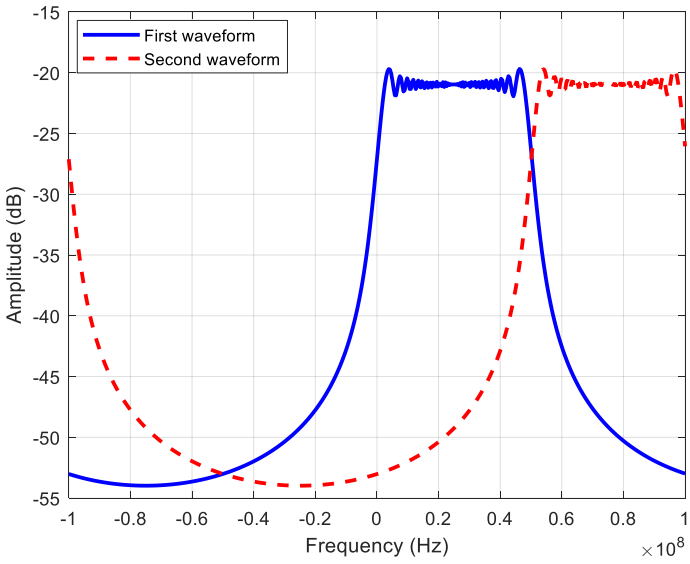

Figure 3.4: *The spectra of the transmitted LFM waveforms.*

location for the noiseless case are shown in Fig.3.5 and Fig.3.6, respectively, where it is clear that no azimuth aliasing is present using MIMO SAR configurations unlike the case for the conventional SISO SAR. In addition, the sidelobes level of the range cuts of the estimated scene using the proposed FDSI-MIMO SAR is much lower than the one obtained using the matched filter based MIMO SAR. This is because our proposed algorithm takes into account the fact that the spectrum of the combined signal is not flat.

Parameter	Symbol	Value
Number of Tx	M	2
Number of Rx	N	2
Min. distance to the swath centre	R_0	$20km$
Look angle	ϕ	45^o
Length of a single beamformer	L_a	$2m$
Distance between adjacent Tx/Rx	d	$3m$
Height of a single beamformer	H_a	$0.27m$
Platform Velocity	v_p	$200m/s$
Carrier Frequency	F_c	$4.5GHz$
Sampling Frequency	F_s	$200MS/s$
Single waveform Bandwidth	BW	$50MHz$
Pulse width	τ	$2.5\mu s$

Table 3.1: *Simulation Parameters*

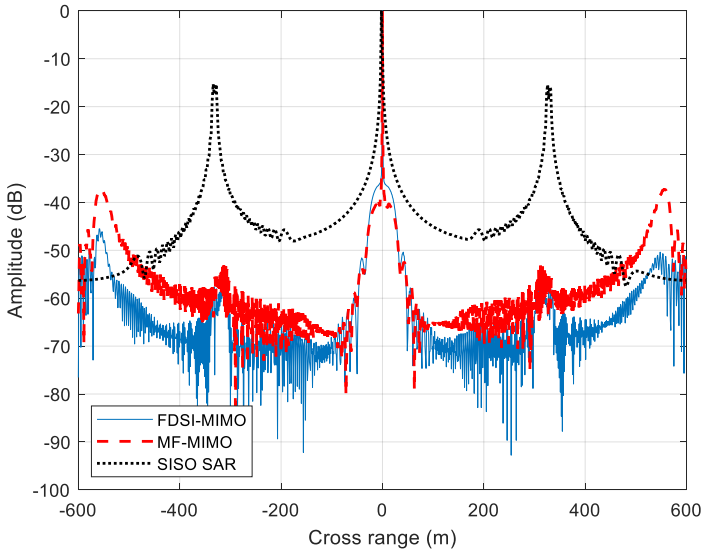

Figure 3.5: *The azimuth cuts for the estimated scene using the proposed FDSI-MIMO SAR, MF-MIMO SAR and the conventional SISO stripmap SAR.*

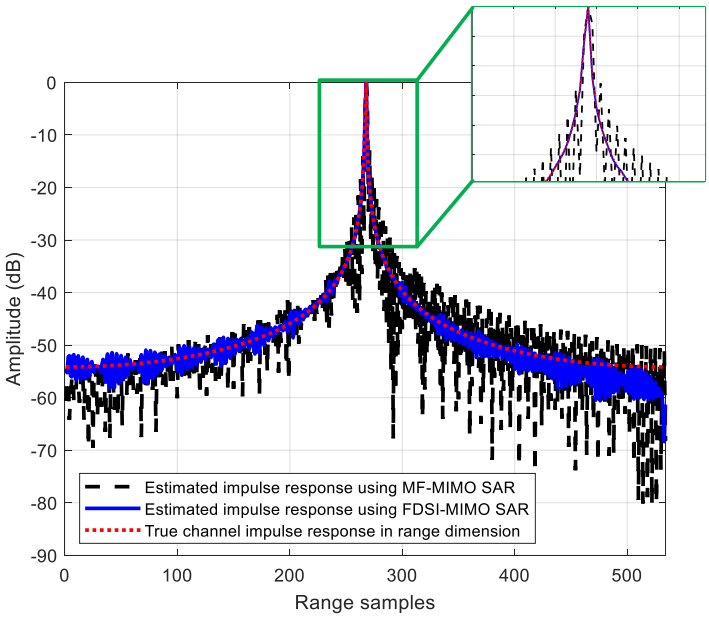

Figure 3.6: *The range cuts of the true range impulse response* $\mathbf{h}_{d,12}$ *and the estimated ones using our proposed FDSI-MIMO SAR and MF-MIMO SAR.*

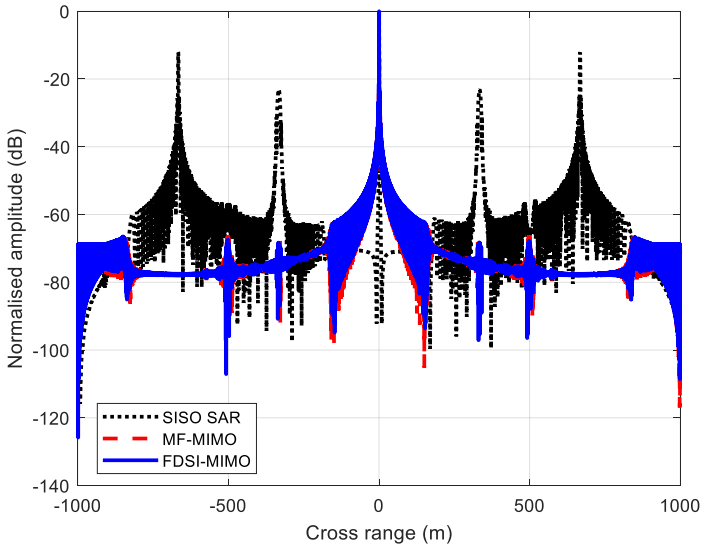

Figure 3.7: *The azimuth cuts for the estimated scene using the proposed FDSI-MIMO SAR, MF-MIMO SAR and the conventional SISO sliding spotlight SAR.*

3.4.1.2 Sliding Spotlight SAR

Consider the simulation parameters listed in Table.3.1. In addition, the synthetic aperture time (T_{syn}) is assumed to be $10s$. The sliding factor (A) and the PRF are 0.5 and $200Hz$, respectively. Assume that there is a single scatterer located at the swath centre. The azimuth and range cuts of the formed image at the scatterer location for the noiseless case are shown in Fig.3.7 and Fig.3.8 respectively. It is clear that there is no azimuth aliasing using MIMO SAR configurations unlike the case for the conventional sliding spotlight SAR. In a similar case to the stripmap scenario, the sidelobes level of the range cuts of the estimated scene using the proposed FDSI-MIMO SAR is much lower than the one obtained using the matched filter based MIMO SAR.

3.5 Conclusion

This chapter presents a bandpass filters based multiple subband IRCI-free MIMO SAR. Two modes of operation are considered, namely, stripmap SAR and sliding spotlight SAR which provides ultra high resolution images with wide swath coverage. A set of conventional LFM waveforms is used for transmission which eases the implementation. The use of FDSI-based

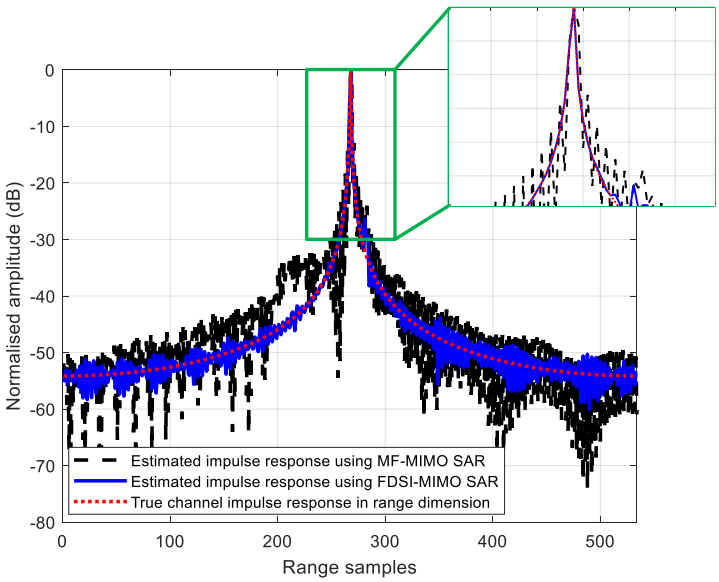

Figure 3.8: *The range cuts of the true range impulse response* $\mathbf{h}_{d,12}$ *and the estimated ones using our proposed FDSI-MIMO SAR and MF-MIMO SAR.*

estimation algorithm to estimate the range profile is particularly appropriate in MIMO SAR application because the non-flat spectrum of the combined subband waveforms is taken into account which is not the case in the matched filter. In addition, a PRF lower than the Doppler bandwidth is used and the resulted azimuth ambiguity is removed using a set of spatial filters and azimuth deramping for the case of sliding spotlight SAR. It should be pointed out that the use of a bank of bandpass filters at the receive does not allow to utilise the bandwidth to maximum efficiency. Therefore, alternative methods are proposed in the subsequent chapters to process the subband waveforms jointly without separating them at the receiver.

Chapter 4
Multiple-Beam Based Multiple Subband IRCI-Free MIMO SAR

4.1 Introduction

Most of multiple subband MIMO SAR algorithms in the literature [8] [9], including the one presented in Chapter 3, use a bank of bandpass filters (BPFs) at the receiver to separate the subbands. However, the overlap between the spectra of adjacent subbands will affect the performance of the range profile estimation. Therefore, a guard band needs to be added between the adjacent subbands so that they can be separated at the receiver using a bank of BPFs [9] which would affect the bandwidth utilisation efficiency.

In this chapter, we propose a new MIMO SAR configuration shown in Fig.4.1 in which the beams of the transmitters are wide and multiple contiguous receiving subbeams with different phase centres and squint angles are generated in the azimuth direction. The system pulse repetition frequency (PRF) needs only to satisfy the Nyquist rate of the partial Doppler bandwidth corresponding to each receiver subbeam. Wide Doppler bandwidth is then synthesised to obtain wide swath high resolution image.

Moreover, the proposed algorithm does not require separating the subbands at the receiver as they are processed jointly without a need to add guard bands between adjacent subbands. This is accomplished by formulating the MIMO SAR problem as an N individual multiple-input single-output (MISO) system identification problems using the principle of displaced phase centre (DPC), where N is the number of receivers. As a result, the proposed algorithm utilises the available bandwidth to maximum efficiency and facilitates the use of linear frequency-modulated (LFM) waveforms and, hence, gains all the inherent benefits of these waveforms (e.g. constant envelope and unity peak to average power ratio). The narrowband assumption is relaxed to the bandwidth of the individual transmitted subband as FDMA is used. In addition, a frequency domain system identification (FDSI) based algorithm is described in Section 4.2 to estimate the channel impulse responses of the MISO problems in the range dimension instead of

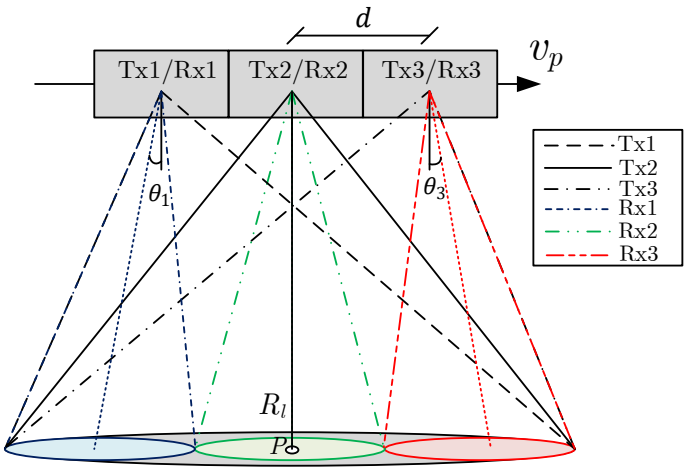

Figure 4.1: *MIMO SAR configuration where R_l is the slant range of the closest approach to a point target P located at the lth range cell, v_p is the platform velocity, d is the distance between adjacent Tx/Rx and θ_n is the squint angle of the nth receiver beam ($\theta_2 = 0$).*

a matched filter, which has the IRCI-free property and then, a way of combining the estimated impulse responses in the azimuth dimension is explained to obtain a high resolution wide swath (HRWS) image. In Section 4.3, the method of synthesising a wide transmit antenna beam from a narrow antenna beam applied in SIMO SAR is extended to MIMO SAR in order to attain the desired signal-to-noise ratio (SNR). Finally, both simulated and constructed raw data are used in Section 4.4 to validate the effectiveness of the proposed algorithm. The results of this chapter were published in [16] and [17].

4.2 Impulse Response Estimation and Image Formation

Consider a narrowband MIMO SAR system with an array of M antenna elements at the transmitter and an array of N antenna elements at the receiver. Using the received signal model described in Section 2.5.2.1, the discrete time version of the received signals for the case when

$M = N = 3$ as shown in Fig.4.1 can be expressed as the following ($\forall n = 1, 2, 3$):

$$z_n[n_t, n_a] = \sum_{l=0}^{L-1} h_{1n}[l, n_a]x_1[n_t - l] + \sum_{l=0}^{L-1} h_{2n}[l, n_a]x_2[n_t - l] + \sum_{l=0}^{L-1} h_{3n}[l, n_a]x_3[n_t - l] + w_n[n_t] \tag{4.1}$$

As described previously, each transmitter emits a portion of the total bandwidth and the range resolution should correspond to the total transmitted bandwidth. Therefore, the received signals due to all the transmitted waveforms should be processed jointly. In addition, the effective sampling frequency in the azimuth dimension is $f_p = \mathrm{PRF} = B_d/N$ so it is expected to have an azimuth ambiguity. The azimuth ambiguity is avoided by reducing the beamwidth of each receiver so that the Doppler bandwidth of each receiver is B_d/N. The beam of each receiver should have a squint angle so that the area spotted by the wide transmitted beams is completely covered, as shown in Fig.4.1. The cross-range resolution should correspond to the full Doppler bandwidth B_d and thus, the Doppler bandwidths at all receivers should be processed jointly as explained in the following.

The Fourier transform of (4.1) across both azimuth and range dimensions (for $n = 1, 2, 3$) expressed as a function of the impulse response, whose phase centre is located in the middle using the principle of DPC [44], can be written as follows:

$$\begin{aligned} Z_1(f_r, f_a) =& X_1(f_r)H_{11}(f_r, f_a) + X_2(f_r)H_{21}(f_r, f_a) + X_3(f_r)H_{31}(f_r, f_a) + W_1(f_r) \\ =& B_1(f_r, f_a)H_{31}(f_r, f_a) + W_1(f_r) \end{aligned} \tag{4.2}$$

$$\begin{aligned} Z_2(f_r, f_a) =& X_1(f_r)H_{12}(f_r, f_a) + X_2(f_r)H_{22}(f_r, f_a) + X_3(f_r)H_{32}(f_r, f_a) + W_2(f_r) \\ =& B_2(f_r, f_a)H_{22}(f_r, f_a) + W_2(f_r) \end{aligned} \tag{4.3}$$

$$\begin{aligned} Z_3(f_r, f_a) =& X_1(f_r)H_{13}(f_r, f_a) + X_2(f_r)H_{23}(f_r, f_a) + X_3(f_r)H_{33}(f_r, f_a) + W_3(f_r) \\ =& B_3(f_r, f_a)H_{13}(f_r, f_a) + W_3(f_r) \end{aligned} \tag{4.4}$$

where,

$$B_1(f_r, f_a) = X_1(f_r)e^{j\frac{2\pi df_a}{v_p}}e^{j\frac{2\pi d^2}{\lambda R_l}} + X_2(f_r)e^{j\frac{\pi df_a}{v_p}}e^{j\frac{3\pi d^2}{2\lambda R_l}} + X_3(f_r) \tag{4.5}$$

$$B_2(f_r, f_a) = X_1(f_r)e^{j\frac{\pi df_a}{v_p}}e^{-j\frac{\pi d^2}{2\lambda R_l}} + X_2(f_r) + X_3(f_r)e^{-j\frac{\pi df_a}{v_p}}e^{-j\frac{\pi d^2}{2\lambda R_l}} \tag{4.6}$$

$$B_3(f_r, f_a) = X_1(f_r) + X_2(f_r)e^{-j\frac{\pi df_a}{v_p}}e^{j\frac{3\pi d^2}{2\lambda R_l}} + X_3(f_r)e^{-j\frac{2\pi df_a}{v_p}}e^{j\frac{2\pi d^2}{\lambda R_l}} \tag{4.7}$$

The spectra of the transmitting waveforms $X_m(f_r)\ \forall m \in [1, 2, 3]$ from (4.5), (4.6) and (4.7) are chosen such that each $B_n(f_r, f_a)\ \forall n \in [1, 2, 3]$ occupies the whole fast time spectrum to identify $H_{31}(f_r, f_a)$, $H_{22}(f_r, f_a)$ and $H_{13}(f_r, f_a)$. All of the impulse responses to be estimated have the same phase centre but each occupies a portion of the Doppler bandwidth. Therefore, they need to be analysed in order to synthesise the full Doppler bandwidth properly to obtain the corresponding cross-range resolution in the formed image.

The instantaneous Doppler frequency of $h_{31}[l, n_a]$, $h_{22}[l, n_a]$ and $h_{13}[l, n_a]$ (h_{mn} is defined in (2.72)) can be derived as follows:

$$\begin{aligned} f_{d,31}(n_a) &= \frac{1}{2\pi}\frac{d}{dn_a}\phi_{l,31}(n_a) \\ &= \underbrace{\frac{2}{\lambda}v_p\sin(\theta_1)}_{f_{dc,31}} - \frac{2}{\lambda}\frac{v_p^2\cos^2(\theta_1)n_aT_r}{R_l} \end{aligned} \tag{4.8}$$

$$\begin{aligned} f_{d,22}(n_a) &= \frac{1}{2\pi}\frac{d}{dn_a}\phi_{l,22}(n_a) \\ &= \underbrace{\frac{2}{\lambda}v_p\sin(\theta_2)}_{f_{dc,22}} - \frac{2}{\lambda}\frac{v_p^2\cos^2(\theta_2)n_aT_r}{R_l} \end{aligned} \tag{4.9}$$

$$\begin{aligned} f_{d,13}(n_a) &= \frac{1}{2\pi}\frac{d}{dn_a}\phi_{l,13}(n_a) \\ &= \underbrace{\frac{2}{\lambda}v_p\sin(\theta_3)}_{f_{dc,13}} - \frac{2}{\lambda}\frac{v_p^2\cos^2(\theta_3)n_aT_r}{R_l} \end{aligned} \tag{4.10}$$

where T_r denotes the pulse repetition interval (PRI) and $f_{dc,mn}$ is the Doppler centroid of h_{mn}. As the squint angles of the receivers are generally small, it can be seen from (4.8), (4.9) and (4.10) that the Doppler bandwidth of each receiver can be expressed as follows:

$$B_{d,13} \approx B_{d,22} \approx B_{d,31} = \left|\frac{2}{\lambda}\frac{v_p^2\cos^2(\theta_1)T_a}{R_l}\right| \tag{4.11}$$

where T_a is the synthetic aperture time.

The impulse responses $H_{31}(f_r, f_a)$, $H_{22}(f_r, f_a)$ and $H_{13}(f_r, f_a)$ will be estimated individually using the FDSI-based algorithm as described in Section 3.3. It should be noted that the azimuth frequency f_a of H_{mn} varies within the following range:

$$\frac{-f_p}{2} + f_{dc,31} \leq f_a \leq \frac{f_p}{2} + f_{dc,31} \tag{4.12}$$

A constant phase term should be compensated for in the estimated $\mathbf{h}_{22}(f_a)$ to make sure that its phase centre is aligned with the phase centres of the other estimated impulse responses and this can be done by multiplying the estimated $\mathbf{h}_{22}(f_a)$ by the following constant phase:

$$H_{comp} = e^{-j\frac{2\pi d^2}{\lambda R_l}} \tag{4.13}$$

The full Doppler bandwidth is synthesised before forming the image by performing the following steps:

1. The data of each receiving beam after the bulk range cell migration correction (RCMC) are converted into range time-Doppler domain.

2. The data of each receiving beam are then zero-padded in the Doppler dimension so that the points of each Doppler spectrum are increased by a factor of N.

3. Each zero-padded data is then frequency shifted in the Doppler dimension by the corresponding Doppler centroid to compensate for the Doppler shift introduced by the squint angle.

4. The data of all receiving beams are then added together to form the full Doppler bandwidth spectrum.

The resulted full Doppler bandwidth data is then used to perform azimuth compression and obtain the final image.

4.3 Transmitter Wide Beam Generation

The same antenna array can be used for both transmission and reception of the radar pulses by applying digital beamforming techniques. The trivial solution to achieve a wide transmit beam is the application of amplitude tapering, but this would significantly reduce the radiated power [66]. In addition, the high-power amplifiers may not be driven in saturation, which would lower the overall efficiency.

The wide transmit beam in Fig.4.1 can be achieved by transmitting multiple subpulses sequentially in a single PRI using the same narrow receive beam as described in Section 2.4.3. Each transmitted subpulse is associated with a different transmit narrow beam, which is switched in such a way that the wide transmit beam is synthesised as shown in Fig.4.2. This operation permits the use of the same large-receive antenna, which reduces the peak power requirement in order to attain the desired signal-to-noise ratio (SNR). Furthermore, the use of a synthesised wide beam will suppress the receiving interbeams overlapping by employing multiple subapertures in each receiver to perform digital beamforming (DBF) on receive in elevation, which has been applied in modified SPCMB SAR [68][92][67][71] and described in Section 2.4.3. Echoes corresponding to different subpulses (at each instant of time) arrive from different elevation angles. Therefore, it is possible to separate them by DBF on receive in elevation using the relation between the time delay and elevation angle in a side-looking radar imaging geometry.

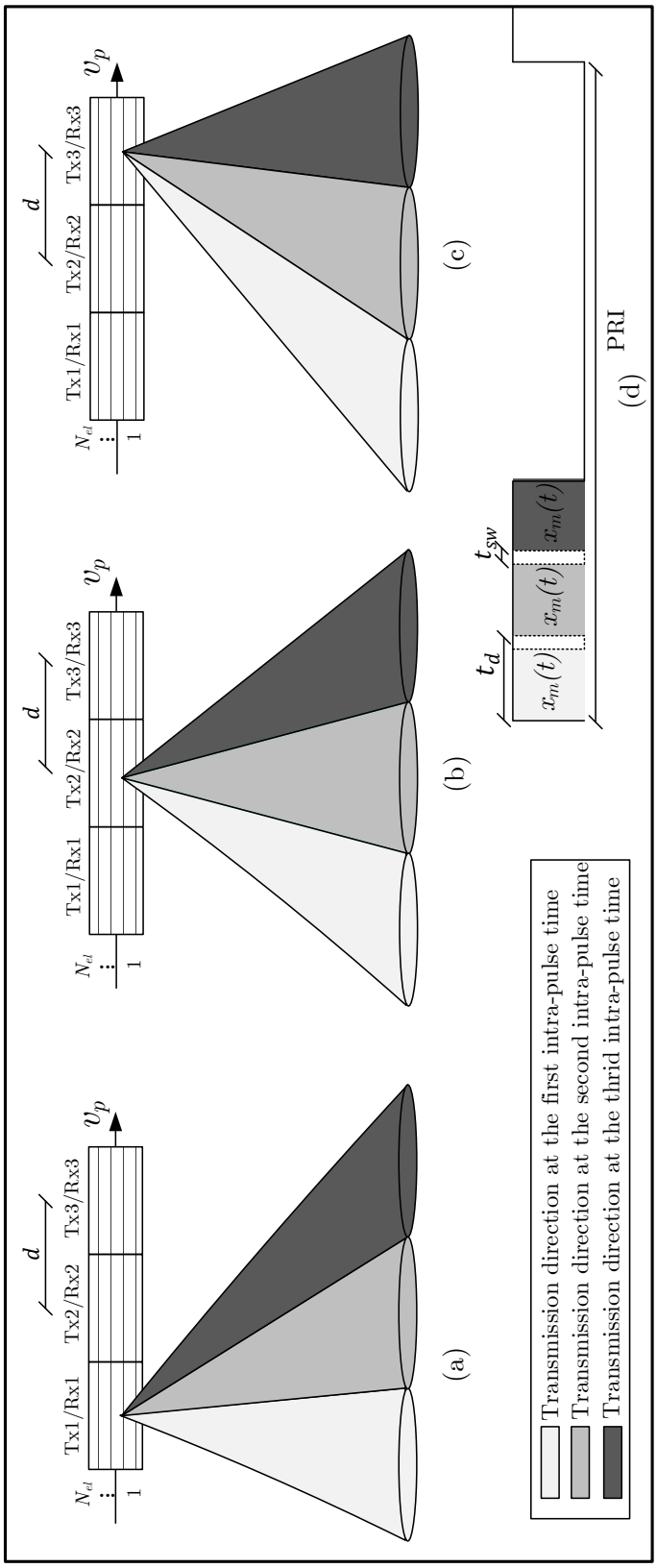

Figure 4.2: *Generation of synthesised wide transmission beams from narrow beams. (a) Transmission directions sequence of the* 1st *transmitter. (b) Transmission directions sequence of the* 2nd *transmitter. (c) Transmission directions sequence of the* 3rd *transmitter. (d) Timing structure of a single* PRI *transmitted by the* mth *transmitter where* t_{sw} *denotes the beam switching time. Each receiver consists of* N_{el} *elevation channels.*

The disadvantages of this operation are the increase of the system complexity due to use of DBF on receive in elevation and the broadening of the transmit window because of the multiple transmitted subpulses in a single PRI, which enlarges the blind area. However, it does not affect the application under consideration (i.e. HRWS imaging) which relies on a rather low PRF and the subpulse switching times, which are of the order of several microseconds can be included without loosing much of the duty cycle [66].

A fractional delay t_d, which includes the beam switching time as shown in Fig.4.2, should be accounted for in the range profile estimation. This can be done by reexpressing $B_1(f_r, f_a)$, $B_2(f_r, f_a)$, and $B_3(f_r, f_a)$ in (4.2),(4.3) and (4.4) as follows:

$$B_1(f_r, f_a) = X_1(f_r)e^{j\frac{2\pi df_a}{v_p}}e^{j\frac{2\pi d^2}{\lambda R_l}} + X_2(f_r)e^{j\frac{\pi df_a}{v_p}}e^{j\frac{3\pi d^2}{2\lambda R_l}} + X_3(f_r) \tag{4.14}$$

$$B_2(f_r, f_a) = \left(X_1(f_r)e^{j\frac{\pi df_a}{v_p}}e^{-j\frac{\pi d^2}{2\lambda R_l}} + X_2(f_r) + X_3(f_r)e^{-j\frac{\pi df_a}{v_p}}e^{-j\frac{\pi d^2}{2\lambda R_l}}\right)e^{-j2\pi f_r t_d} \tag{4.15}$$

$$B_3(f_r, f_a) = \left(X_1(f_r) + X_2(f_r)e^{-j\frac{\pi df_a}{v_p}}e^{j\frac{3\pi d^2}{2\lambda R_l}} + X_3(f_r)e^{-j\frac{2\pi df_a}{v_p}}e^{j\frac{2\pi d^2}{\lambda R_l}}\right)e^{-j4\pi f_r t_d} \tag{4.16}$$

Due to different introduced delays present in (4.14)-(4.16), echoes corresponding to different subpulses (i.e. receiving beams) can be separated by DBF on receive in elevation described in Section 2.3.5. The same process described in Section 4.2 is then applied to estimate the impulse response and form the image. A schematic of the proposed configuration implementation is shown in Fig.4.3 where it should be noted that the interpolation of the azimuth data at a sampling frequency of $N\mathrm{PRF}$ can be efficiently implemented by fast Fourier transform (FFT) and zero padding in the Doppler domain.

4.4 Simulation Results

This section shows the numerical results of our proposed FDSI estimation algorithm for MIMO SAR using a set of LFM waveforms. It is divided into subsections, in which Section 4.4.1 shows how the azimuth ambiguity is avoided using the proposed MIMO SAR configuration and compares the results with the ones obtained using the BPF-based MIMO SAR proposed in Chapter 3 and conventional SISO SAR. Section 4.4.2 shows the azimuth ambiguity characteristics for the case of different implementations of our proposed configuration and demonstrates how the sidelobes effect on the azimuth ambiguity is suppressed using IBS described in Section 2.4.3. Section 4.4.3 demonstrates the effectiveness of our proposed algorithm in a cluttered scene.

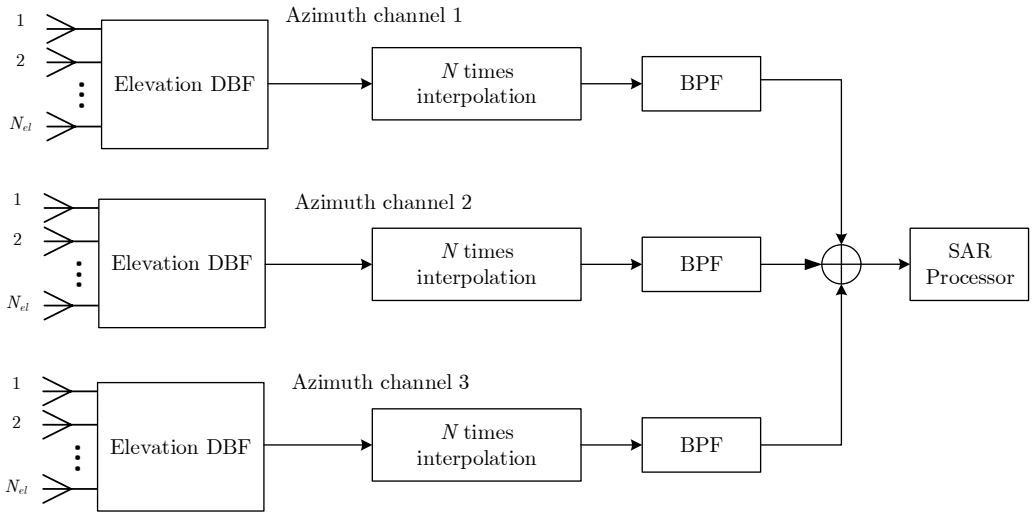

Figure 4.3: *A schematic of the proposed configuration implementation. The schematic of elevation DBF block is as shown in Fig.2.16. Image formation algorithm is performed in SAR processor block.*

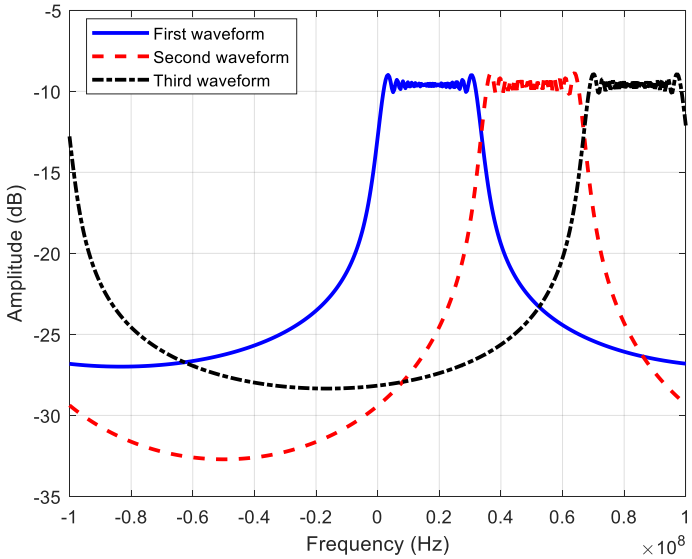

Figure 4.4: *The spectra of the transmitted waveforms.*

Parameter	Symbol	Value
Number of Tx	M	3
Number of Rx	N	3
Min. distance to the swath centre	R_0	$20km$
Look angle	ϕ	45^o
Azimuth length of the conventional SISO SAR beamformer	L_a	$1.5m$
Azimuth length of the single beamformer in MIMO SAR	$L_{a,\mathrm{MIMO}}$	$4.5m$
Distance between adjacent Tx/Rx in MIMO SAR	d	$4.5m$
Doppler bandwidth	B_d	$300Hz$
Pulse repetition frequency	PRF	$100Hz$
Platform Velocity	v_p	$225m/s$
Carrier Frequency	F_c	$4.5GHz$
Sampling Frequency	F_s	$200MS/s$
Single waveform Bandwidth	BW	$33.333MHz$
Pulse width	τ	$2.5\mu s$

Table 4.1: *Simulation Parameters*

4.4.1 Azimuth Ambiguity Removal

Consider the simulation parameters listed in Table 4.1 and assume that the spectra of the emitted waveforms are as shown in Fig.4.4 and there is a single scatterer located at the swath centre. The MIMO configuration used in the simulation is as shown in Fig.4.1, in which the squint angles are $|\theta_2| = 0$ and $|\theta_1| = |\theta_3| = \theta_{BW}/N = 0.0148$ where θ_{BW} is the 3-dB width of the wide transmit beam. The 3-dB width of each transmit receive beam of the BPF-based MIMO SAR proposed in Chapter is 3 is θ_{BW} which is similar to the one of the conventional SISO SAR beam used in the simulation (i.e. It is chosen in a way to obtain the same cross-range resolution as the one in MIMO SAR). In addition, the azimuth and range cuts of the formed image at the scatterer location for the noiseless case are shown in Fig.4.5 and Fig.4.6, respectively. It is clear that there is no azimuth aliasing using the MIMO SAR configurations even though the PRF used is lower than the Doppler bandwidth unlike the case in the conventional SISO SAR, where aliased components are present. It should be noted that the main advantages of the proposed multiple-beam based MIMO SAR over the BPF-based MIMO SAR proposed in Chapter 3 are the full utilisation of the available bandwidth as there is no need to use guard bands and the improvement of the SNR due to the use of large transmit-receive antennas.

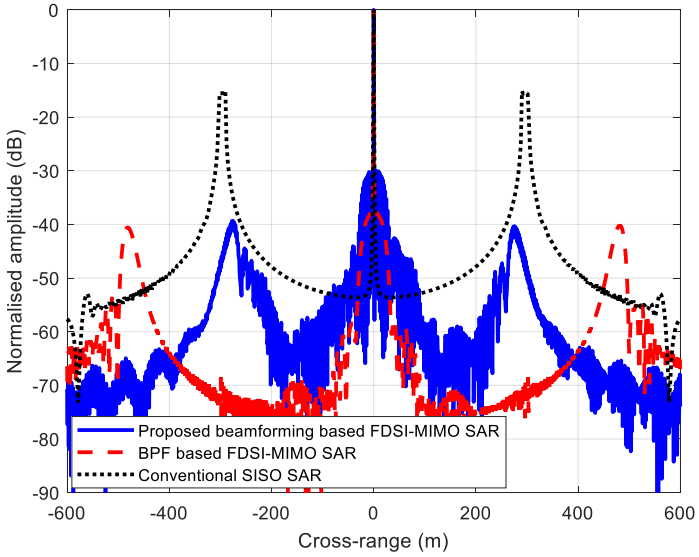

Figure 4.5: *The azimuth cut of the estimated scene using the proposed algorithm and the conventional SAR.*

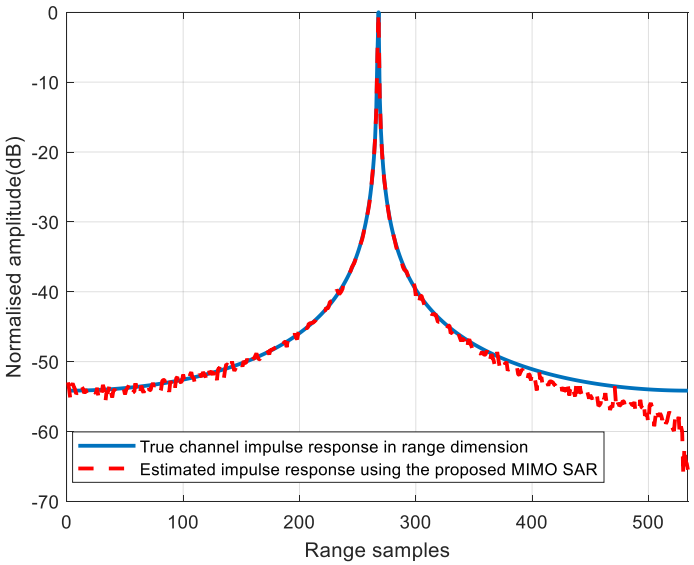

Figure 4.6: *The range cut of the true channel impulse response (i.e. the original image at the true scatterer location) and the estimated one using the proposed configuration.*

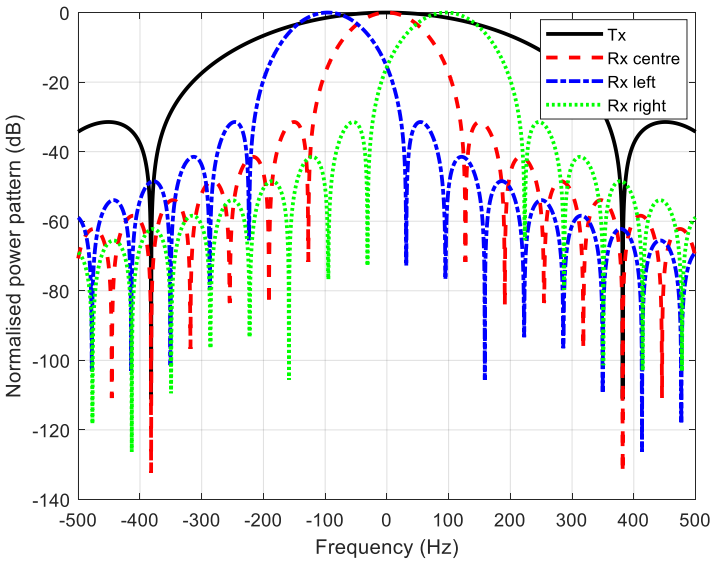

Figure 4.7: *The transmit and receive beam patterns as a function of frequency for the case when the proposed configuration is implemented using real wide transmit beams. It should be noted that all of the transmitters beams have the same shape.*

4.4.2 Azimuth Ambiguity to Signal Ratio (AASR)

The azimuth ambiguity characteristics of the proposed MIMO SAR configuration implemented using real wide transmit beams (i.e. achieved using small size transmit antennas) and synthesised wide transmit beams (i.e. achieved by combining multiple narrow transmit beams) are simulated and compared with the azimuth ambiguity of conventional SISO SAR based on the AASR. Assume that the beam patterns of the transmitters and receivers when the proposed configuration shown in Fig.4.1 is implemented using real wide transmit beams and synthesised wide transmit beams are as shown in Fig.4.7 and Fig.4.8, respectively. The beam pattern used in the conventional SISO SAR is the same as the transmitter pattern in Fig.4.7, which has been chosen to obtain the same cross-range resolution as the one obtained in MIMO SAR.

The AASR as a function of PRF of the proposed MIMO SAR configuration using the two different implementations is as shown in Fig.4.9, in which only one of the side beams is considered because the other side beam has the same azimuth ambiguity characteristics. The AASR for the case of conventional SISO SAR is shown in Fig.4.10 from which one can see that the PRF required for MIMO SAR configuration using any of the two different implementations is lower than that of conventional SISO SAR to attain the same azimuth ambiguity performance at the

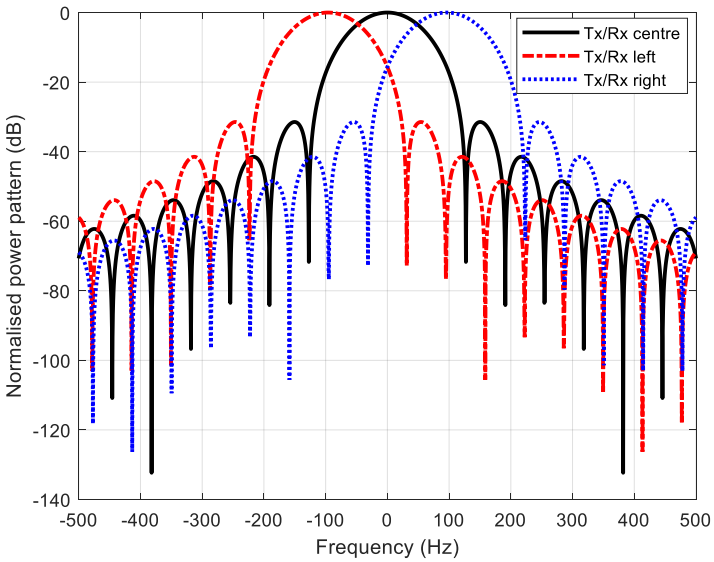

Figure 4.8: *The transmit and receive beam patterns as a function of frequency for the case when the proposed configuration is implemented using synthesised wide transmit beams.*

same cross-range resolution which makes it possible to have a wider swath.

It is clear from Fig.4.9 that the azimuth ambiguity characteristics of the proposed configuration using real wide beams transmitters are worse than that using synthesised beams. This is expected because the sidelobes of the receiving beams, as shown in Fig.4.7, are located within the mainlobe of the wide transmit beam, which would make the azimuth ambiguity stronger unlike the case of synthesised wide transmit beams implementation. The azimuth ambiguity characteristics of the side beams in both implementations are worse than that of the central beams. This is because the mainlobes of the side beams in the real wide beams transmitters implementation are located in the rolling-down part of the transmission mainlobe, and many of the sidelobes of the receivers side beams are located in the mainlobe peak part of the transmission beam, which would make the azimuth ambiguity stronger. In addition, the power of the desired signal component (i.e. the second term of (2.63)) in the side beams of synthesised wide transmission beams implementation is lower than that of the central beam, which would make the azimuth ambiguity characteristics worse. Furthermore, the azimuth ambiguity characteristics are better for the case of the synthesised wide beams with IBS because the second term of (2.62) is almost suppressed by DBF on receive in elevation. According to [45], the PRF should be chosen such that it is equal to an oversampling factor (1.1 to 1.4) multiplied by the 3-dB Doppler bandwidth.

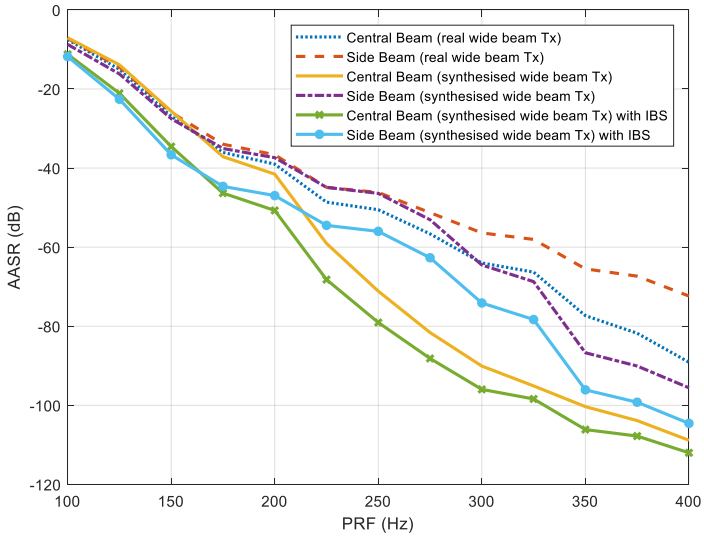

Figure 4.9: *Azimuth ambiguity characteristics of the proposed MIMO SAR implemented using real wide beams transmitters and synthesised wide beams transmitters.* $\Delta_{nm} = -10dB$ *for the case of the inter-beam suppression (IBS).*

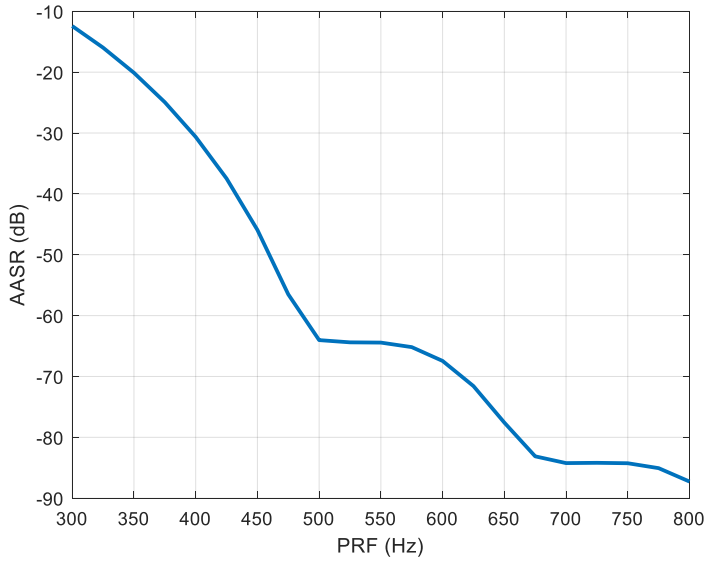

Figure 4.10: *Azimuth ambiguity characteristics of the conventional SISO SAR.*

4.4.3 Raw Data Simulation

As there is no multiple-phase centre multiple subband MIMO SAR data available for us, a publicly available airborne SISO SAR data "Gotcha" [93] is used to construct MIMO SAR data to test our proposed FDSI-based algorithm in a cluttered scene. A way for constructing MIMO SAR data from raw conventional SISO SAR data has been used in the literature [94] under the assumption that all receivers have the same beams so that the received signals at all receivers occupy the same Doppler bandwidth.

In our proposed configuration, the received signals at each receiver occupy a portion of the total Doppler bandwidth, which corresponds to the narrow receive beam. Accordingly, the first step of constructing MIMO SAR data is to divide the total azimuth angles into N parts, because each single azimuth angle corresponds to a single Doppler frequency. The Doppler bandwidth of the received signals from each of the N parts corresponds to the Doppler bandwidth at one of the N receivers. Next, the following steps are performed on the received signals at the $n\mathrm{th}$ azimuth part which corresponds to the $n\mathrm{th}$ receiver to construct the multiple-phase centre multiple subband MIMO SAR data for the case when $M = N = 2$:

1. The data are transformed into range frequency domain.
2. The whole range bandwidth is divided into two subbands.
3. Each subband is transformed into the Doppler domain and then multiplied by a slow time delay function to simulate the effective phase centre (EPC).
4. The data is then converted into range-azimuth domain, and each subband data is convolved with the corresponding transmitted subband chirp.
5. The subbands data are added together to construct the MIMO SAR data received at the $n\mathrm{th}$ receiver.

Consider the main system parameters listed in Table 4.2. It should be noted that the interbeams effect on the azimuth ambiguity is not considered here as it already has been addressed in Section 4.4.2. The formed image using the data received by a single receiver and the data combined from all receivers using the proposed algorithm are shown in Fig.4.11 and Fig.4.12, respectively. It is clear that the formed image using the data of all receivers has better cross-range resolution. In addition, the cross-range cuts of the indicated areas with red rectangles in

Parameter	Symbol	Value
Number of Tx	M	2
Number of Rx	N	2
Min. distance to the swath centre	R_0	$10.158km$
3-dB width of a single MIMO receiver beamwidth	θ_{BW}	3^o
3-dB width of the conventional SISO SAR	$\theta_{BW,\text{SISO}}$	6^o
Carrier Frequency	F_c	$9.58GHz$
distance between adjacent Tx/RX	d	$1m$
Single waveform Bandwidth	BW	$300MHz$

Table 4.2: *System Parameters*

the formed images are shown in Fig.4.13 from which one can see that the cross-range resolution is improved using the combined data.

Next consider the case of the conventional SISO SAR in which the transmitted bandwidth is $300MHz$, and the sampling frequency across the azimuth is similar to MIMO SAR configuration. The formed image is shown in Fig.4.14, where it is clear that the image is aliased. The sampling frequency across the azimuth should be double the one used in the MIMO SAR configuration in order to avoid the aliasing in the azimuth dimension. The formed image using double the sampling frequency of MIMO SAR is as shown in Fig.4.15. The range cuts of the indicated areas with red rectangles in the images shown in Fig.4.12 and Fig.4.15 are as shown in Fig.4.16. It is clear that the range resolution is better for the MIMO SAR configuration because it is possible to transmit more bandwidth and the narrowband assumption is relaxed to the bandwidth of the individual transmitting channel.

4.5 Conclusion

This chapter presents an FDSI-MIMO SAR algorithm using multiple phase centre multiple azimuth beams to obtain HRWS imaging. The proposed algorithm is IRCI-free although no guard bands are added between the adjacent spectra of the transmitting waveforms (i.e. the spectra of transmitting waveforms are partially overlapped) which allows us to utilise the available bandwidth to maximum efficiency. The length of the waveform is not a function of the channel impulse response in the range dimension, which makes the proposed algorithm suitable for stripmap mode of operation. A set of conventional LFM waveforms is used for transmission to simplify implementations and, hence, gains all the inherent benefits of these waveforms

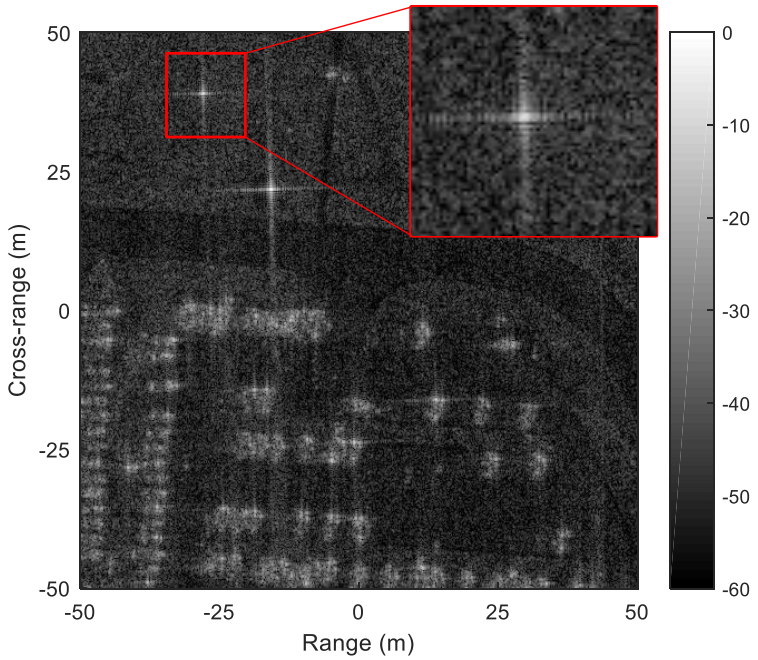

Figure 4.11: *Formed image using a single received data.*

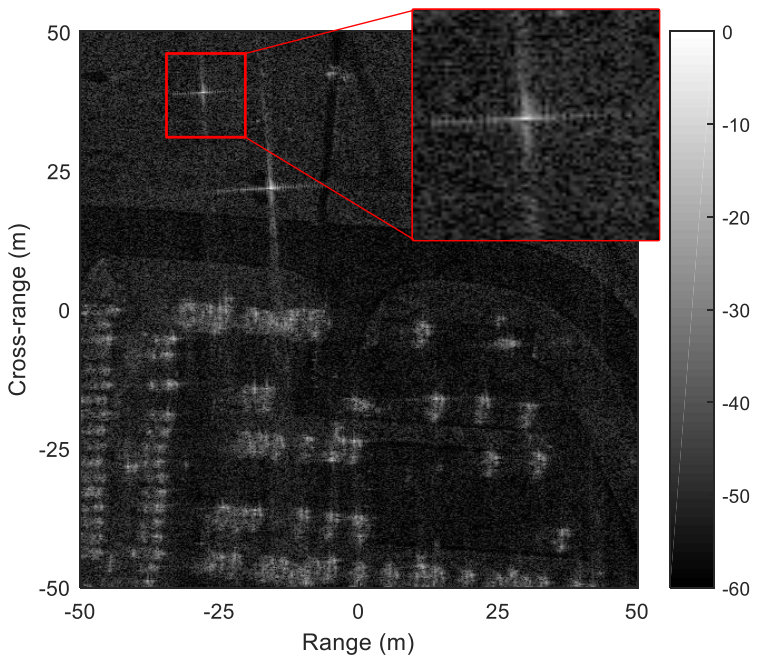

Figure 4.12: *Formed image using all receivers data.*

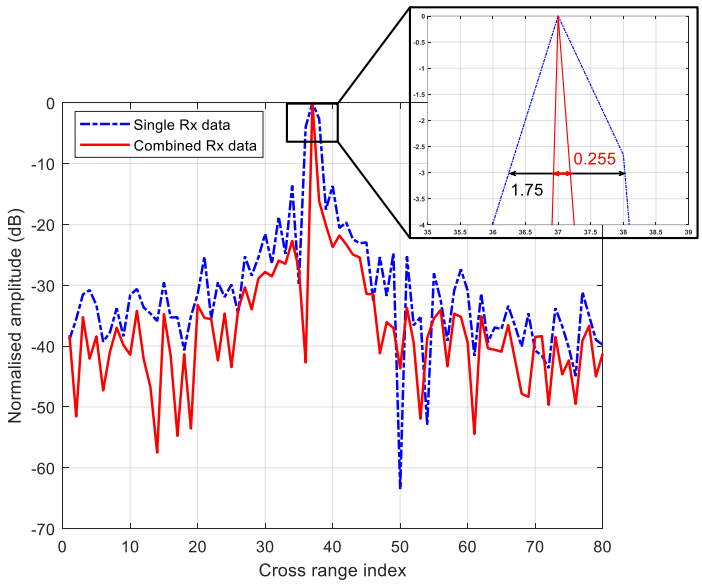

Figure 4.13: *The cross-range cuts of the indicated area with red rectangles in Fig.4.11 and Fig.4.12.*

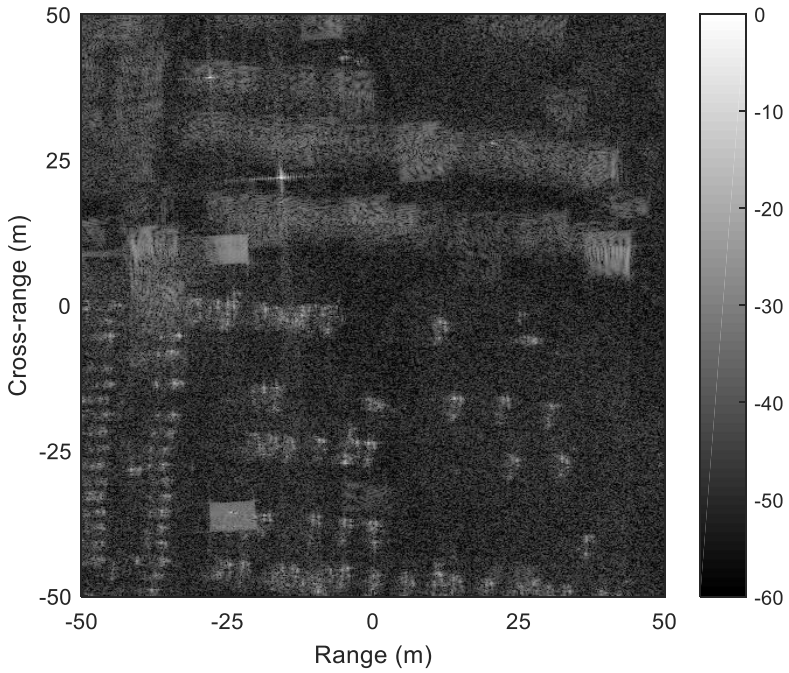

Figure 4.14: *Formed image using SISO SAR in which the azimuth sampling frequency is half the Doppler bandwidth and the same as the one used in MIMO SAR.*

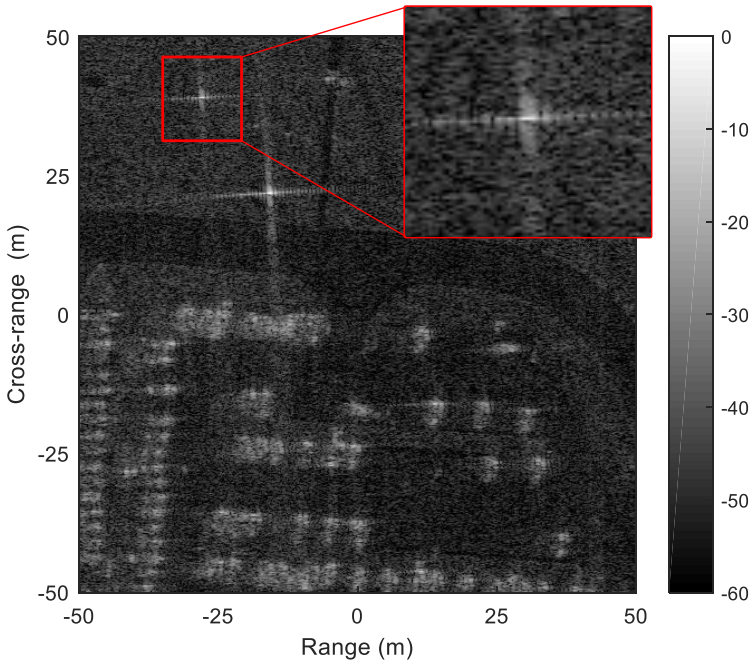

Figure 4.15: *Formed image using SISO SAR data in which the azimuth sampling frequency is double the one used in MIMO SAR.*

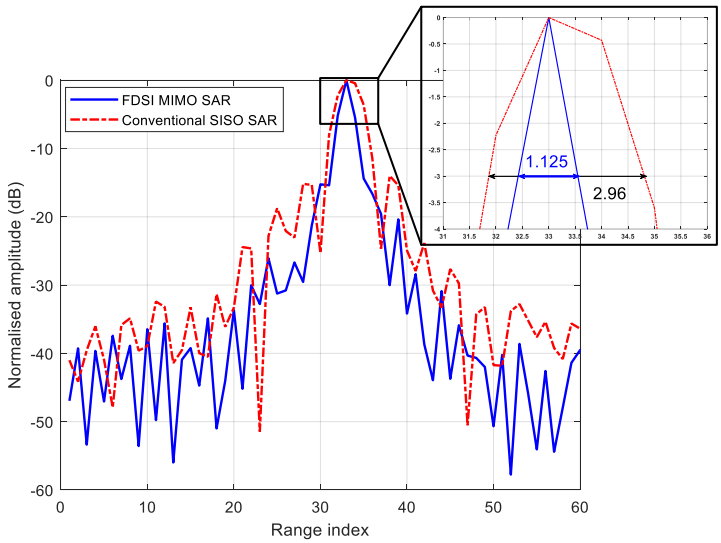

Figure 4.16: *The range cuts of the indicated area with red rectangles in Fig.4.12 and Fig.4.15.*

(e.g. constant envelope and unity peak to average power ratio). In addition, a PRF lower than the Doppler bandwidth is used to obtain wide swath without having aliasing in the Doppler spectrum. This is a result of the multiple narrow azimuth beams formed on receive. Wide transmission beams are synthesised using narrow beams in order to use the same antennas for both transmission and reception and achieve the desired SNR. The azimuth ambiguity characteristics of the proposed MIMO SAR configuration, implemented using real wide transmit beams and synthesised wide transmit beams, are analysed. Simulation results of point targets and constructed raw data are used to validate the effectiveness of the proposed algorithm.

Chapter 5
Multiple Subband IRCI-Free MIMO SAR

5.1 Introduction

In this chapter, we extend the work introduced in Chapter 4 in a way that the beamwidths of all the transmitters and receivers are the same and they simultaneously illuminate the same imaging area as shown in Fig.5.1. As a result, the proposed configuration has an advantage over the multiple-beam based FDSI-MIMO SAR proposed in Chapter 4 that no DBF in elevation is required because the interbeams overlapping problem is avoided which simplifies the system complexity. Moreover, the blind area is smaller as compared to the configuration proposed in Chapter 4 because only one pulse per PRI is transmitted. In addition, The proposed configuration has advantages over the BPF based FDSI-MIMO SAR proposed in Chapter 3 that the available bandwidth is utilised to maximum efficiency and less computations are required for the azimuth ambiguity removal because the whole range bandwidth is processed at once unlike the case of the BPF based FDSI-MIMO SAR where each subband is processed individually.

This chapter is divided into sections in which Section 5.2 formulates the received signal of the proposed configuration as a system identification problem in a way that echoes due to different transmitted subband waveforms are processed jointly without separating them at the receivers. Section 5.3 explains how the azimuth ambiguity resulted from using a PRF lower than the Doppler bandwidth is removed using a set of spatial filters applied on the received signals formulated as system identification problems. Finally, both simulated and constructed raw data are used in Section 5.4 to validate the effectiveness of the proposed algorithm. The results of this chapter were submitted in [18].

5.2 Received Signal Model

Consider a narrowband MIMO SAR system with an array of M antenna elements at the transmitter and an array of N antenna elements at the receiver. The following can be expressed

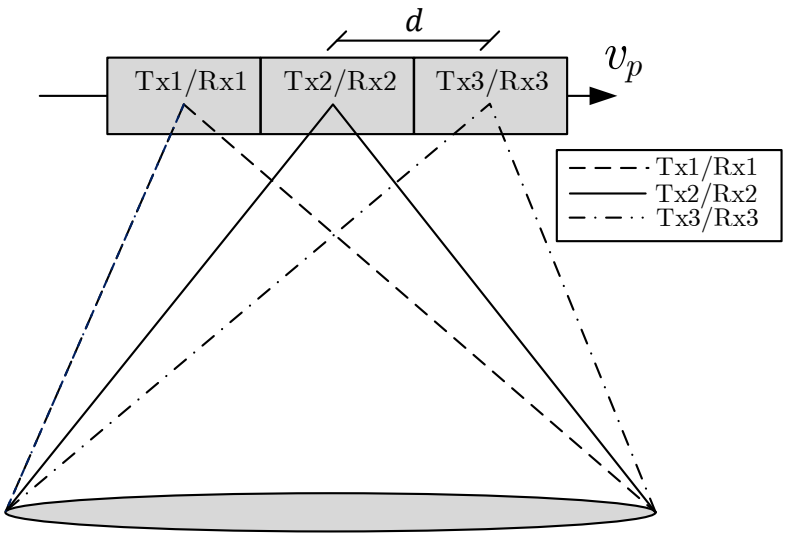

Figure 5.1: *Multiple subband MIMO SAR configuration in which the beam patterns of the transmitters and receivers are the same. v_p and d denote the platform velocity and the distance between adjacent Tx/Rx, respectively.*

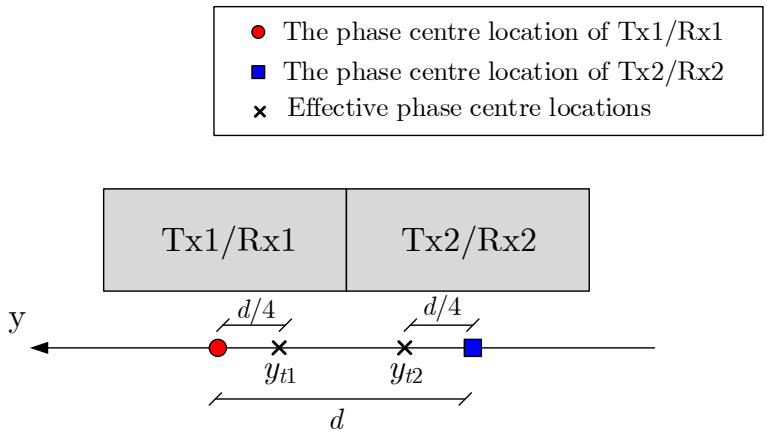

Figure 5.2: *The locations of the phase centres for the case when $M = N = 2$. y_{t1} and y_{t2} indicate the locations of the phase centres whose azimuth impulse responses are denoted by $h_{az,t1}$ and $h_{az,t2}$, respectively.*

using the principle of DPC [44] for the case when $M = N = 2$:

$$h_{az,t1}(\eta) = h_{az,11}(\eta - \frac{d}{4v_p})e^{-j\frac{\pi d^2}{8\lambda R_l}} \tag{5.1}$$

$$= h_{az,21}(\eta + \frac{d}{4v_p})e^{-j\frac{\pi d^2}{8\lambda R_l}} \tag{5.2}$$

$$h_{az,t2}(\eta) = h_{az,12}(\eta - \frac{d}{4v_p})e^{-j\frac{\pi d^2}{8\lambda R_l}} \tag{5.3}$$

$$= h_{az,22}(\eta + \frac{d}{4v_p})e^{-j\frac{\pi d^2}{8\lambda R_l}} \tag{5.4}$$

where $h_{az,t1}$ and $h_{az,t2}$ denote the azimuth impulse response whose phase centres locations are as indicated by y_{t1} and y_{t2} in Fig.5.2, respectively. The following can be expressed as well using the principle of DPC for the general case when $N \geq 3$ (i.e. without loss of generality it is assumed $M = N = 3$ as shown in Fig.5.1):

$$h_{az,12}(\eta) = h_{az,22}(\eta + \frac{d}{2v_p})e^{-j\frac{\pi d^2}{2\lambda R_l}} \tag{5.5}$$

$$h_{az,21}(\eta) = h_{az,11}(\eta - \frac{d}{2v_p})e^{-j\frac{\pi d^2}{2\lambda R_l}} \tag{5.6}$$

$$h_{az,32}(\eta) = h_{az,22}(\eta - \frac{d}{2v_p})e^{-j\frac{\pi d^2}{2\lambda R_l}} \tag{5.7}$$

$$h_{az,23}(\eta) = h_{az,33}(\eta + \frac{d}{2v_p})e^{-j\frac{\pi d^2}{2\lambda R_l}} \tag{5.8}$$

$$h_{az,13}(\eta) = h_{az,22}(\eta)e^{-j\frac{2\pi d^2}{\lambda R_l}} \tag{5.9}$$

Using the received signal model described in Section 2.5.2.1 (i.e. for the case when the squint angles of all beams are zeros), the discrete time version of the received signals can be expressed as the following:

$$z_n[n_t, n_a] = \sum_{m=1}^{M} \sum_{l=0}^{L-1} h_{mn}[l, n_a] x_m[n_t - l] + w_n[n_t] \tag{5.10}$$

5.3 Azimuth Ambiguity Removal

The azimuth ambiguity removal is performed in the frequency domain. It is based on a generalised concept of the sampling theorem which has been applied in SIMO SAR case in [43]

under the name of multi-aperture reconstruction algorithm. The algorithm states that if a signal is sampled by $1/N\text{th}$ its Nyquist frequency, it is possible to reconstruct the original signal when there are N independent representations of the aliased signal. A special case when $N = 2$ is first assumed and then will be generalised to the case when $N \geq 3$.

5.3.1 Two Receivers Case ($N = 2$)

The Fourier transform of (5.10) across both azimuth and range dimensions for the case when $M = N = 2$ can be expressed as follows:

$$Z_1(f_r, f_a) = X_1(f_r)H_{11}(f_r, f_a) + X_2(f_r)H_{21}(f_r, f_a) + W_1(f_r) \tag{5.11}$$

$$Z_2(f_r, f_a) = X_1(f_r)H_{12}(f_r, f_a) + X_2(f_r)H_{22}(f_r, f_a) + W_2(f_r) \tag{5.12}$$

The received signals in (5.11) and (5.12) can be expressed as a function of the impulse responses $h_{az,t1}$ and $h_{az,t2}$ using the principle of DPC (5.1)-(5.4) as follows:

$$Z_1(f_r, f_a) = B(f_r, f_a)H_{t1}(f_r, f_a) + W_1(f_r) \tag{5.13}$$

$$Z_2(f_r, f_a) = B(f_r, f_a)H_{t2}(f_r, f_a) + W_2(f_r) \tag{5.14}$$

where,

$$B(f_r, f_a) = X_1(f_r)e^{j\frac{\pi df_a}{2v_p}}e^{j\frac{\pi d^2}{8\lambda R_l}} + X_2(f_r)e^{-j\frac{\pi df_a}{2v_p}}e^{j\frac{\pi d^2}{8\lambda R_l}} \tag{5.15}$$

The spectra of the transmitting waveforms $X_m(f_r), \forall m \in [1, 2]$ are chosen such that $B(f_r, f_a)$ occupies the whole fast time spectrum to identify the impulse response in the range dimension. The signals in (5.13) and (5.14) can be expressed as a function of $H_{12} = H_{21}$, which corresponds to the impulse response of a SISO case in which the effective phase centre is located midway between the two receivers, as follows (the noise is not included in the following equations for the sake of clarity):

$$Z_1(f_r, f_a) = \underbrace{B(f_r, f_a)H_{21}(f_r, f_a)}_{U(f_r,f_a)}\underbrace{e^{j\frac{\pi df_a}{2v_p}}e^{-j\frac{\pi d^2}{8\lambda R_l}}}_{Q_1(f_a)} \tag{5.16}$$

$$Z_2(f_r, f_a) = \underbrace{B(f_r, f_a)H_{21}(f_r, f_a)}_{U(f_r,f_a)}\underbrace{e^{-j\frac{\pi df_a}{2v_p}}e^{-j\frac{\pi d^2}{8\lambda R_l}}}_{Q_2(f_a)} \tag{5.17}$$

The Doppler bandwidth of the received signals is assumed to be $N\text{PRF}$ (i.e. 2PRF) and the

sampling frequency in the azimuth dimension is $f_p = \mathrm{PRF}$ which would make the signals aliased in the azimuth dimension. $U(f_r, f_a)$ can be perfectly reconstructed from the aliased signals in the azimuth dimension expressed in (5.16) and (5.17) as explained in Section 3.2.

5.3.2 Three Receivers Case ($N \geq 3$)

Without loss of generality, it is assumed $N = M = 3$. The Fourier transform of (5.10) across both azimuth and range dimensions when the system configuration is as shown in Fig.5.1 can be expressed as follows:

$$Z_1(f_r, f_a) = X_1(f_r)H_{11}(f_r, f_a) + X_2(f_r)H_{21}(f_r, f_a) + X_3(f_r)H_{31}(f_r, f_a) + W_1(f_r) \tag{5.18}$$

$$Z_2(f_r, f_a) = X_1(f_r)H_{12}(f_r, f_a) + X_2(f_r)H_{22}(f_r, f_a) + X_3(f_r)H_{32}(f_r, f_a) + W_2(f_r) \tag{5.19}$$

$$Z_3(f_r, f_a) = X_1(f_r)H_{13}(f_r, f_a) + X_2(f_r)H_{23}(f_r, f_a) + X_3(f_r)H_{33}(f_r, f_a) + W_3(f_r) \tag{5.20}$$

The received signals in (5.18), (5.19) and (5.20) can be expressed as a function of of the impulse responses h_{21}, h_{22} and h_{23}, respectively, using the principle of DPC (5.5)-(5.9) as follows:

$$Z_1(f_r, f_a) = B_1(f_r, f_a)H_{21}(f_r, f_a) + W_1(f_r) \tag{5.21}$$

$$Z_2(f_r, f_a) = B_2(f_r, f_a)H_{22}(f_r, f_a) + W_2(f_r) \tag{5.22}$$

$$Z_3(f_r, f_a) = B_3(f_r, f_a)H_{23}(f_r, f_a) + W_3(f_r) \tag{5.23}$$

where,

$$B_1(f_r, f_a) = X_1(f_r)e^{j\frac{\pi d f_a}{v_p}} e^{j\frac{\pi d^2}{2\lambda R_l}} + X_2(f_r) + X_3(f_r)e^{-j\frac{\pi d f_a}{v_p}} e^{-j\frac{3\pi d^2}{2\lambda R_l}} \tag{5.24}$$

$$B_2(f_r, f_a) = X_1(f_r)e^{j\frac{\pi d f_a}{v_p}} e^{-j\frac{\pi d^2}{2\lambda R_l}} + X_2(f_r) + X_3(f_r)e^{-j\frac{\pi d f_a}{v_p}} e^{-j\frac{\pi d^2}{2\lambda R_l}} \tag{5.25}$$

$$B_3(f_r, f_a) = X_1(f_r)e^{j\frac{\pi d f_a}{v_p}} e^{-j\frac{3\pi d^2}{2\lambda R_l}} + X_2(f_r) + X_3(f_r)e^{-j\frac{\pi d f_a}{v_p}} e^{j\frac{\pi d^2}{2\lambda R_l}} \tag{5.26}$$

As the constant phase terms in (5.24), (5.25) and (5.26) are relatively small as they are functions of the slant range R_l, the following approximation can be used:

$$B_1(f_r, f_a) \approx B_2(f_r, f_a) \approx B_3(f_r, f_a) \approx B(f_r, f_a) \tag{5.27}$$

where,

$$B(f_r, f_a) = X_1(f_r)e^{j\frac{\pi df_a}{v_p}} + X_2(f_r) + X_3(f_r)e^{-j\frac{\pi df_a}{v_p}} \tag{5.28}$$

The spectra of the transmitting waveforms $X_m(f_r), \forall m \in [1, 2, 3]$ are chosen such that $B(f_r, f_a)$ occupies the whole fast time spectrum to identify the impulse response in the range dimension. Next, the received signals can be expressed as a function of H_{22}, which corresponds to the impulse response of a SISO case in which the effective phase centre is located at the second receiver, as follows:

$$\begin{aligned} Z_1(f_r, f_a) &\approx B(f_r, f_a)H_{22}(f_r, f_a)e^{j\frac{\pi df_a}{v_p}} e^{-j\frac{\pi d^2}{2\lambda R_l}} + W_1(f_r) \\ &\approx U(f_r, f_a)Q_1(f_a) + W_1(f_r) \end{aligned} \tag{5.29}$$

$$\begin{aligned} Z_2(f_r, f_a) &\approx B(f_r, f_a)H_{22}(f_r, f_a) + W_2(f_r) \\ &\approx U(f_r, f_a)Q_2(f_a) + W_2(f_r) \end{aligned} \tag{5.30}$$

$$\begin{aligned} Z_3(f_r, f_a) &\approx B(f_r, f_a)H_{22}(f_r, f_a)e^{-j\frac{\pi df_a}{v_p}} e^{-j\frac{\pi d^2}{2\lambda R_l}} + W_3(f_r) \\ &\approx U(f_r, f_a)Q_3(f_a) + W_3(f_r) \end{aligned} \tag{5.31}$$

where,

$$U(f_r, f_a) = B(f_r, f_a)H_{22}(f_r, f_a) \tag{5.32}$$

$$Q_1(f_a) = e^{j\frac{\pi df_a}{v_p}} e^{-j\frac{\pi d^2}{2\lambda R_l}} \tag{5.33}$$

$$Q_2(f_a) = 1 \tag{5.34}$$

$$Q_3(f_a) = e^{-j\frac{\pi df_a}{v_p}} e^{-j\frac{\pi d^2}{2\lambda R_l}} \tag{5.35}$$

The Doppler bandwidth of the received signals is assumed to be $3\mathrm{PRF}$ and the sampling frequency in the azimuth dimension is $f_p = \mathrm{PRF}$. Therefore, it is expected to have aliasing in the azimuth dimension which can be removed to perfectly reconstruct $U(f_r, f_a)$ in the same way as the one described previously for the case when $M = N = 2$ in Section 3.2. The reconstruction

filters in this case can be computed as follows:

$$\mathbf{P}(f_a) = 3\mathbf{Q}^{-1}(f_a) \tag{5.36}$$

where,

$$\mathbf{Q}(f_a) = \begin{bmatrix} Q_1(f_a) & Q_2(f_a) & Q_3(f_a) \\ Q_1(f_a + f_p) & Q_2(f_a + f_p) & Q_3(f_a + f_p) \\ Q_1(f_a + 2f_p) & Q_2(f_a + 2f_p) & Q_3(f_a + 2f_p) \end{bmatrix} \tag{5.37}$$

$$\mathbf{P}(f_a) = \begin{bmatrix} P_{11}(f_a) & P_{12}(f_a + f_p) & P_{13}(f_a + 2f_p) \\ P_{21}(f_a) & P_{22}(f_a + f_p) & P_{23}(f_a + 2f_p) \\ P_{31}(f_a) & P_{32}(f_a + f_p) & P_{33}(f_a + 2f_p) \end{bmatrix} \tag{5.38}$$

After the removal of the azimuth ambiguity, the impulse response estimation and image formation will be performed as explained in Section 3.3. A schematic of the proposed configuration implementation is shown in Fig.5.3 where it is clear that the whole range bandwidth is processed at once unlike the case of the BPF-based MIMO SAR configuration proposed in Chapter 3 in which each subband is processed individually.

5.4 Simulation Results

This section shows the simulation results of our proposed FDSI-based multiple subband MIMO SAR using a set of LFM waveforms. The section is divided into three subsections in which Section 5.4.1 demonstrates the azimuth ambiguity removal using our proposed FSDI MIMO SAR and compares the results with the ones obtained using the proposed configurations in the previous chapters. Section 5.4.2 compares the azimuth ambiguity resulted from the interbeams overlapping in the proposed configuration with the one presented in Chapter 4. Section 5.4.3 illustrates the effectiveness of our proposed algorithm in a cluttered scene.

5.4.1 Azimuth Ambiguity Removal

Consider the simulation parameters listed in Table.5.1 and assume that there is a single scatterer located at the swath centre. The spectra of the transmitted waveforms are as shown in Fig.4.4. The azimuth and range cuts of the formed image at the scatterer location for the noiseless case

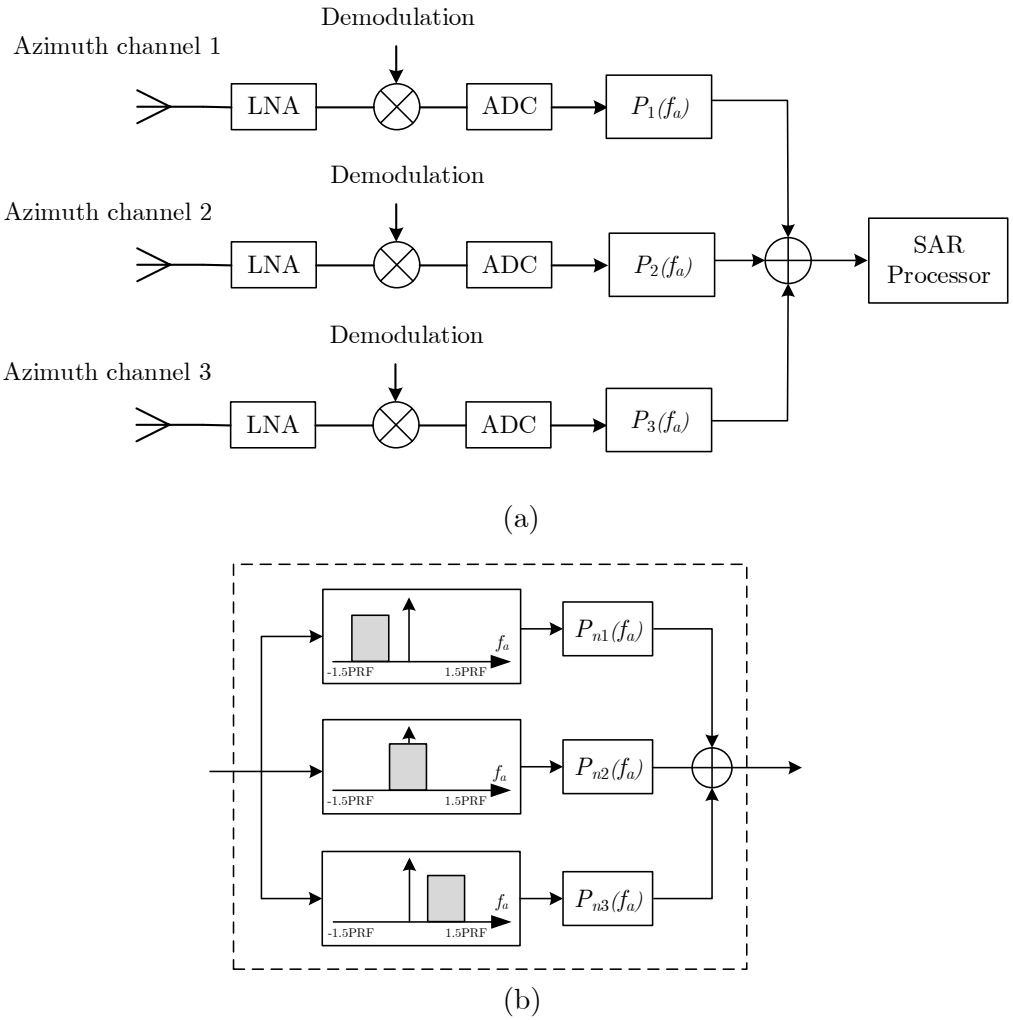

Figure 5.3: *(a)A schematic of the proposed configuration implementation. (b) A schematic of the spatial filters bank $P_n(f_a)$ which is computed using* (5.36)*. Image formation algorithm is performed in SAR processor block.*

Parameter	Symbol	Value
Number of Tx	M	3
Number of Rx	N	3
Min. distance to the swath centre	R_0	$20km$
Look angle	ϕ	45^o
Azimuth length of the beamformer	L_a	$1.5m$
Distance between adjacent Tx/Rx in MIMO SAR	d	$1.5m$
Doppler bandwidth	B_d	$300Hz$
Pulse repetition frequency	f_p	$100Hz$
Platform Velocity	v_p	$225m/s$
Carrier Frequency	F_c	$4.5GHz$
Sampling Frequency	F_s	$200MS/s$
Single waveform Bandwidth	BW	$33.333MHz$
Pulse width	τ	$2.5\mu s$

Table 5.1: *Simulation Parameters*

are shown in Fig.5.4 and Fig.5.5, respectively. One can see that the azimuth ambiguity for the case of MIMO SAR configurations is removed even though the operating PRF is lower than the Doppler bandwidth unlike the case of the conventional SISO SAR where azimuth ambiguity is present. It should be noted that the proposed configuration has an advantage over the multiple-beam based MIMO SAR that it does not require DBF in elevation which reduces the implementation complexity. In addition, the proposed configuration utilises the available bandwidth to maximum efficiency unlike the case of the BPF-based MIMO SAR which uses guard bands.

5.4.2 Azimuth Ambiguity Analysis

The azimuth ambiguity due to the interbeams overlapping in the configuration proposed in Chapter 4 (i.e. shown in Fig.4.1) is compared with the proposed system configuration shown in Fig.5.1 in which the transmitters and receivers use the same wide antenna beams. The azimuth ambiguity to signal ratio (AASR) defined in (2.58) will be used for the comparison.

The antenna beam patterns used in the simulation for the system configuration proposed in Chapter 4 are as shown in Fig.4.7. The transmit and receive antenna beam patterns in the proposed configuration are the same as the wide Tx beam depicted in Fig.4.7. It should be noted that all of the side beams of the configuration shown in Fig.4.1 have the same azimuth ambiguity characteristics. Therefore, only one of the side beams is considered. The AASR as a function of the PRF is shown in Fig.5.6 where it is clear from the AASR curves that the

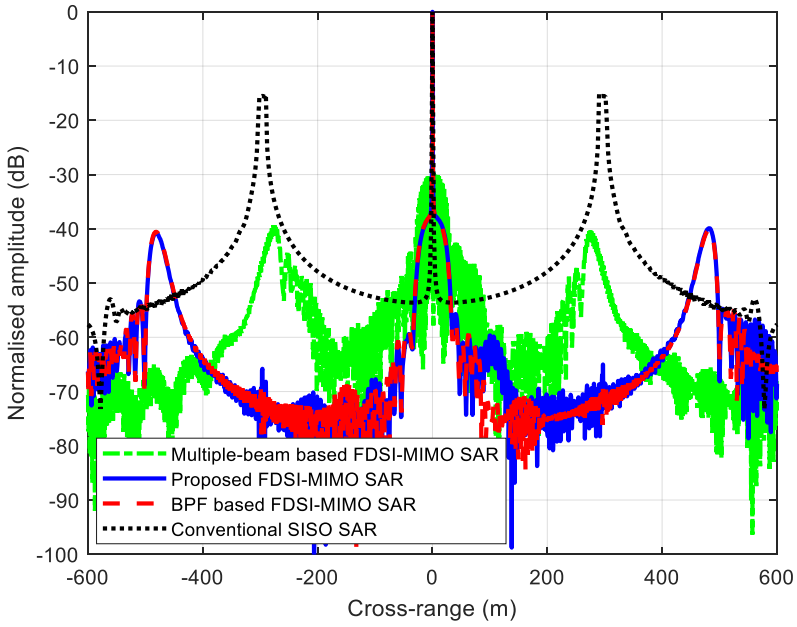

Figure 5.4: *The azimuth cut of the imaged scene using the proposed FDSI-based MIMO SAR, multiple-beam based MIMO SAR, BPF-based MIMO SAR and the conventional SISO SAR.*

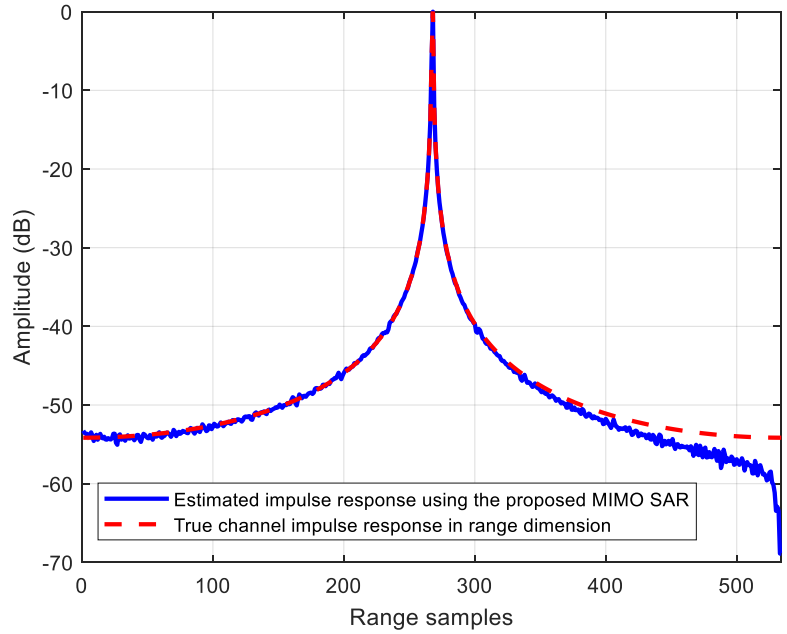

Figure 5.5: *The range cut of the true channel impulse response (i.e. the original image at the true scatterer location) and the estimated one using the proposed configuration.*

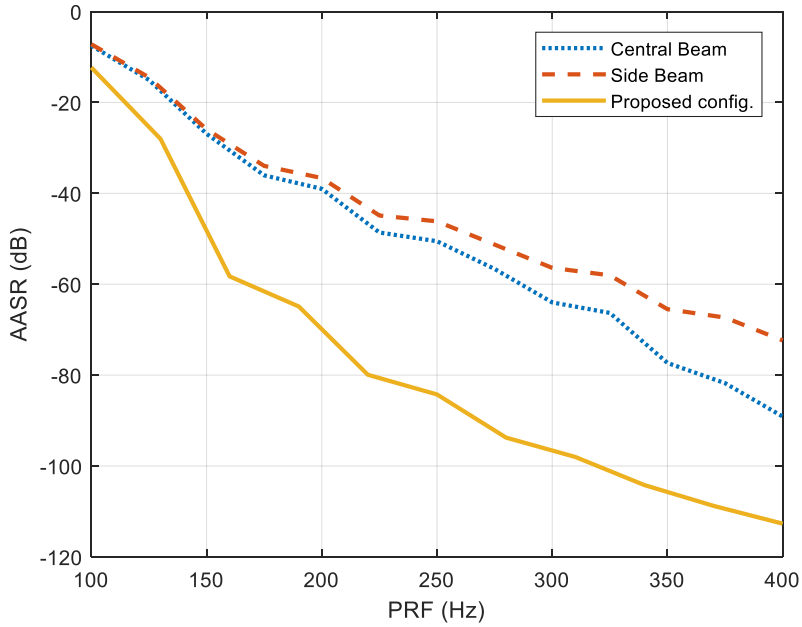

Figure 5.6: *Azimuth ambiguity characteristics of the proposed MIMO SAR configuration in which the same antenna wide beam is used for transmission and reception.*

azimuth characteristics of the system configuration with the narrow receiving beams are worse because the sidelobes of the receiving beams shown in Fig.4.7 are within the mainlobe of the transmit beam. In addition, the azimuth ambiguity of the system configuration with narrow receiving beams is a function of azimuth spacing among the receive beams in addition to the PRF. Therefore, the AASR cannot be reduced unless the azimuth spacing among the receive beams is increased. It is worth pointing out that digital beamforming in elevation on receive is proposed in Chapter 4 to mitigate the effect of interbeams overlapping but this will be at the expense of the system complexity.

It is assumed in the AASR curve of the proposed configuration that the azimuth ambiguity resulted from using a sampling frequency lower than the Doppler bandwidth is removed using a set of spatial filters as explained previously.

5.4.3 Raw Data Simulation

A publicly available airborne SISO SAR data ”Gotcha” [93] is used to construct multiple subband MIMO SAR data as there is no MIMO SAR data available for us. The multiple subband

MIMO SAR data is constructed in order to demonstrate the effectiveness of our proposed algorithm in a cluttered scene.

The following steps are performed to construct the multiple subband MIMO SAR data at the $n\text{th}$ receiver for the case when $M = N$ [94]:

1. The original SISO SAR data is transformed into range frequency domain.

2. The whole range bandwidth is divided into N subbands.

3. Each subband is transformed into Doppler domain. All the subbands other than the $n\text{th}$ subband are multiplied by the corresponding slow time delay functions to simulate the effective phase centre (EPC) difference from the $n\text{th}$ receiver.

4. The data is then converted into range-azimuth domain and each subband data is convolved with the corresponding transmitted subband chirp.

5. The subbands are added together and then down-sampled by a factor of N in the azimuth dimension to construct the multiple subband MIMO SAR data at the $n\text{th}$ receiver.

Consider the main system parameters listed in Table.4.2 but with $\theta_{BW} = \theta_{BW,SISO} = 6^o$. The formed image using a single received channel is similar to the one obtained using SISO SAR configuration as shown in Fig.4.14 where it is clear that the image is aliased. The formed image using the two receiving channels are as shown in Fig.5.7 where it is obvious that the azimuth ambiguity is removed using the multi-aperture reconstruction algorithm.

Next, consider the same conventional SISO SAR case as the one presented in Chapter 4 in which the transmitted bandwidth is $300MHz$ and the sampling frequency across the azimuth is double the one used in the MIMO SAR configuration so that the aliasing in the azimuth dimension is avoided. The formed image of the conventional SISO SAR is as shown in Fig.4.15. The range cuts of the indicated areas with red rectangles in the images shown in Fig.5.7 and Fig.4.15 are as illustrated in Fig.5.8 where one can see that the range resolution is better for the MIMO SAR. The is the result of transmitting more bandwidth and the narrowband assumption is relaxed to the bandwidth of the individual transmitting channel which is the main advantage of using multiple subband MIMO SAR.

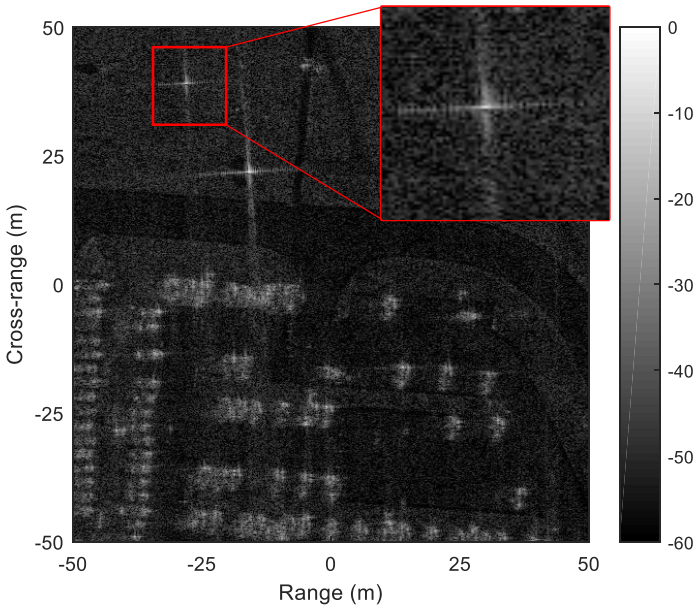

Figure 5.7: *The formed image using all receiving channels.The azimuth ambiguity is removed using the multi-aperture reconstruction algorithm.*

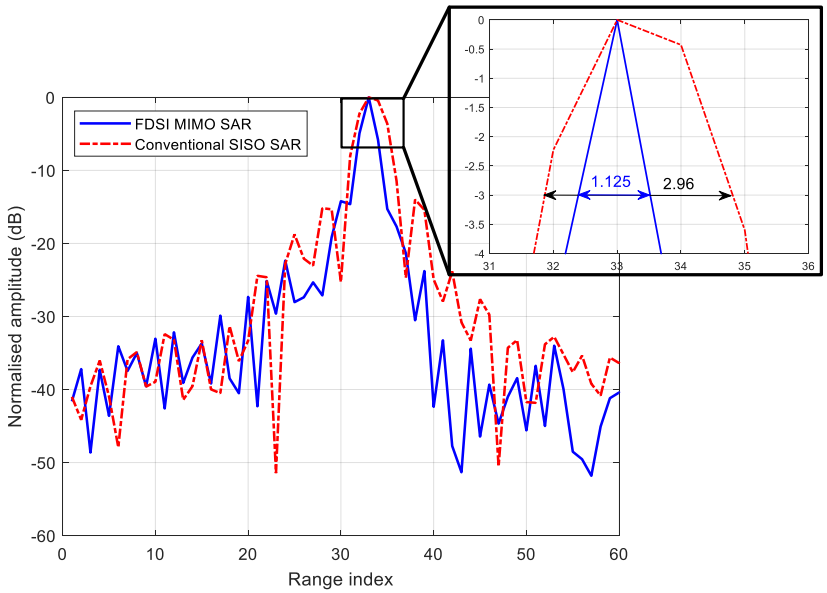

Figure 5.8: *The range cuts of the indicated areas with red rectangles in Fig.5.7 and Fig.4.15.*

5.5 Conclusion

This chapter presents an FDSI multiple subband MIMO SAR algorithm to obtain high resolution wide swath imaging. It exhibits better azimuth ambiguity characteristics as compared to the system configuration proposed in Chapter 4 as the receiving interbeams overlapping is avoided. This is a result of utilising the same antenna beamwidths for transmitters and receivers to simultaneously illuminate the same imaging area. The proposed algorithm utilises the available bandwidth to maximum efficiency as it does not require separating the subbands at the receiver (i.e. there is no need to add guard bands between adjacent subbands). It is IRCI-free although the spectra of transmitting waveforms are partially overlapped which facilitates the use of conventional LFM waveforms and hence, gains all the inherent benefits of these waveforms (e.g. constant envelope and unity peak to average power ratio). In addition, the length of the waveform is not a function of the channel impulse response in the range dimension which makes the proposed algorithm suitable for the stripmap mode of operation. Moreover, a PRF lower than the Doppler bandwidth is used to obtain wide swath and the resulted azimuth ambiguity is removed using a set of spatial filters. Simulation results of point targets and constructed raw data are used to validate the effectiveness of the proposed algorithm.

Chapter 6
Orthogonal Waveform Encoding IRCI-Free MIMO SAR

6.1 Introduction

The minimum pulse repetition frequency (PRF) in orthogonal waveform encoding MIMO SAR should satisfy the inequality $\mathrm{PRF} \geq B_d/K_p$ where B_d denotes the Doppler bandwidth and K_p is the number of independent phase centres which is, for the case that the same antenna arrays are used for transmission and reception, equal to $M + N - 1$ where M and N denote the number of transmitters and receivers, respectively [10].

In this chapter, we propose a new MIMO SAR configuration shown in Fig.6.1, which is independent of the orthogonal waveforms used for transmission, in which multiple contiguous receiving subbeams with different phase centres and squint angles are generated in the azimuth direction and the wide beams of the transmitters are synthesised from the narrow beams as shown in Fig.6.2. Each of the waveforms used for transmission is a sequence of subpulses consisting of conventional LFM waveforms. Echoes corresponding to different effective phase centres (i.e. transmitters) at the receiver are separated using digital beamforming (DBF) on receive in elevation and null-steering technique. This is possible because echoes corresponding to different transmitted subpulses (i.e. effective phase centres) arrive at each instant of time from different elevation angles. The main advantage of the proposed configuration over the conventional MIMO SAR is that all of the effective phase centres are utilised (i.e. even the overlapping ones). In other words, the number of independent effective phase centres in the proposed configuration is $(M \times N)$. This is the result of employing multiple contiguous beams which makes the echoes at the overlapping effective phase centres occupy different Doppler bandwidths. Therefore, the minimum PRF in the proposed configuration should satisfy the inequality $\mathrm{PRF} \geq B_d/(M \times N)$ which provides the opportunity to map wider image swaths with higher cross-range resolution compared to the conventional MIMO SAR.

In addition, a frequency domain system identification (FDSI)-based algorithm is used to estimate the channel impulse response in the range dimension instead of a matched filter which has

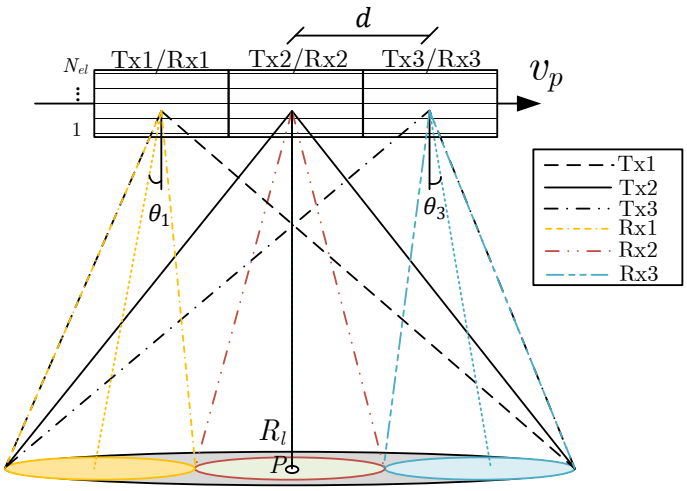

Figure 6.1: *MIMO SAR configuration, where R_l is the slant range of the closest approach to a point target P located at the lth range cell, v_p is the platform velocity, d is the distance between adjacent transmitter and receiver, and θ_n is the squint angle of the nth receiver beam ($\theta_2 = 0$). The wide transmit beams are synthesised from the narrow beams as described in Fig.6.2. Each receiver consists of N_{el} elevation channels.*

the property of free interrange cell interference (IRCI).

This chapter is divided into sections in which Section 6.2 formulates the received signals of the proposed configuration as system identification problems. Section 6.3 describes how the azimuth ambiguity resulted from using a PRF lower than the Doppler bandwidth is removed using multiple contiguous narrow receiving beams along with a set of spatial filters. In addition, it analyses the effect of interbeams overlapping on the azimuth ambiguity and proposes a technique to mitigate it. Both simulated and constructed raw data are used in Section 6.4 to validate the effectiveness of the proposed algorithm. The initial results of this chapter were published in [19] while the the complete results are submitted in [20].

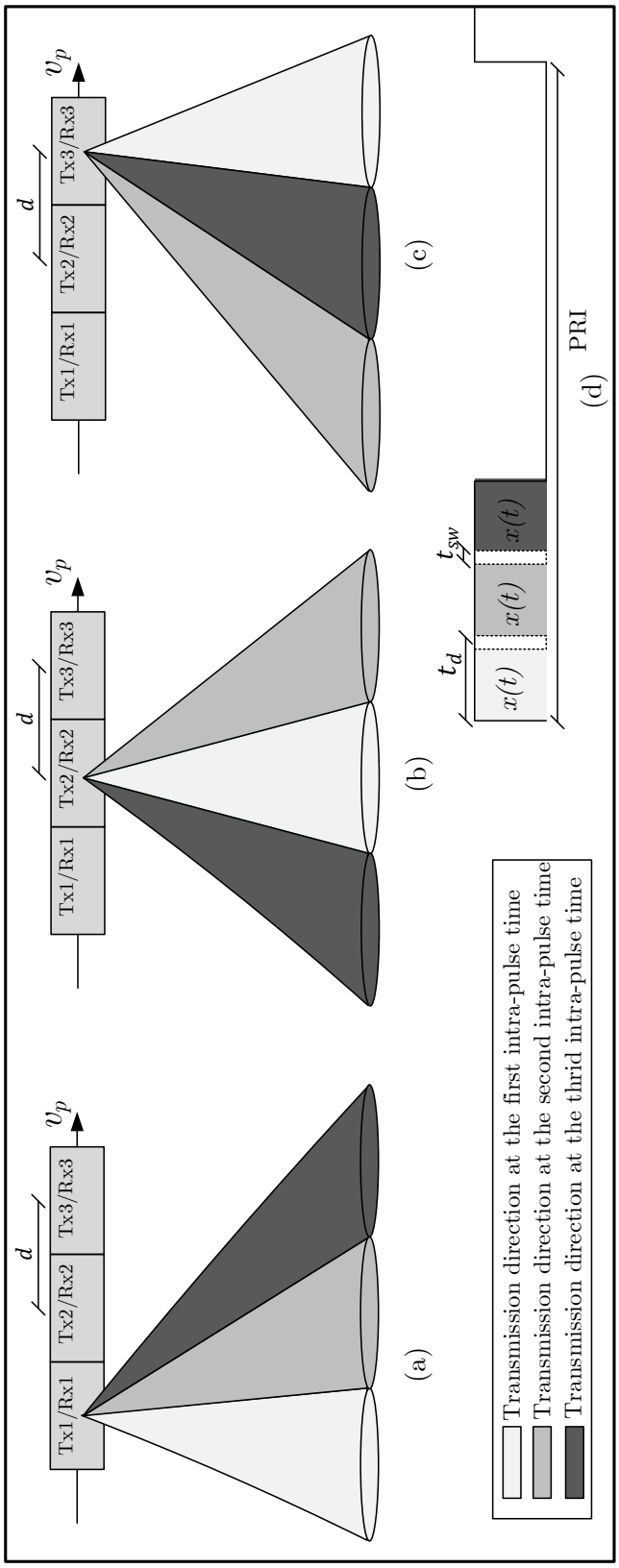

Figure 6.2: *Generation of synthesised wide transmission beams from narrow beams. (a) Transmission directions sequence of the* 1st *transmitter. (b) Transmission directions sequence of the* 2nd *transmitter. (c) Transmission directions sequence of the* 3rd *transmitter. (d) Timing structure of a single* PRI *transmitted by the* m^{th} *transmitter where* t_{sw} *denotes the beam switching time.*

6.2 Received Signal Model

Consider a narrowband MIMO SAR system with M transmit antennas, N receive antennas and N_{el} elevation channels. The baseband received signal at $i\text{th}$ elevation channel in the $n\text{th}$ receiving azimuth aperture and can be expressed as

$$y_{n,i}(t,\eta) = \sum_{m=1}^{M}\sum_{l=0}^{L-1}\left(\sigma_l e^{-j2\pi F_c \tau_{l,mn}(\eta)} a_i(\phi_l) x(t-\tau_{l,mn}(\eta) - \mid n-m \mid t_d)\right) + w_n(t) \tag{6.1}$$

where,

$$a_i(\phi_l) = e^{j2\pi i d_{\text{el}} \sin(\phi_l)/\lambda}, \quad i = 0,1,...,N_{\text{el}}-1 \tag{6.2}$$

$x(t)$ is a known waveform (i.e. LFM waveform), t_d denotes a delay between the transmitted subpulses which includes the beam switching time (t_{sw}), d_{el} denotes the distance between the elevation channels, N_{el} is the number of elevation channels and ϕ_l is the elevation angle of the $l\text{th}$ range cell.

Without loss of generality, consider the case when $M = N = 3$ as shown in Fig.6.1. The timing diagram of the transmitting waveforms is as shown in Fig.6.2 which can be used to express the received signals at the receivers as the following:

$$\begin{aligned} y_{1,i}(t,\eta) = &\sum_{l=0}^{L-1} \sigma_l e^{-j2\pi F_c \tau_{l,11}(\eta)} a_i(\phi_l) x(t-\tau_{l,11}(\eta)) + \\ &\sum_{l=0}^{L-1} \sigma_l e^{-j2\pi F_c \tau_{l,21}(\eta)} a_i(\phi_l) x(t-\tau_{l,21}(\eta) - 2t_d) + \\ &\sum_{l=0}^{L-1} \sigma_l e^{-j2\pi F_c \tau_{l,31}(\eta)} a_i(\phi_l) x(t-\tau_{l,31}(\eta) - t_d) + w_1(t) \end{aligned} \tag{6.3}$$

$$y_{2,i}(t,\eta) = \sum_{l=0}^{L-1} \sigma_l e^{-j2\pi F_c \tau_{l,12}(\eta)} a_i(\phi_l) x(t - \tau_{l,12}(\eta) - t_d) + \sum_{l=0}^{L-1} \sigma_l e^{-j2\pi F_c \tau_{l,22}(\eta)} a_i(\phi_l) x(t - \tau_{l,22}(\eta)) + \sum_{l=0}^{L-1} \sigma_l e^{-j2\pi F_c \tau_{l,32}(\eta)} a_i(\phi_l) x(t - \tau_{l,32}(\eta) - 2t_d) + w_2(t) \tag{6.4}$$

$$y_{3,i}(t,\eta) = \sum_{l=0}^{L-1} \sigma_l e^{-j2\pi F_c \tau_{l,13}(\eta)} a_i(\phi_l) x(t - \tau_{l,13}(\eta) - t_d) + \sum_{l=0}^{L-1} \sigma_l e^{-j2\pi F_c \tau_{l,23}(\eta)} a_i(\phi_l) x(t - \tau_{l,23}(\eta) - 2t_d) + \sum_{l=0}^{L-1} \sigma_l e^{-j2\pi F_c \tau_{l,33}(\eta)} a_i(\phi_l) x(t - \tau_{l,33}(\eta)) + w_3(t) \tag{6.5}$$

The received signals in (6.3), (6.4) and (6.5) are sampled from the range cell that corresponds to the near range to the range cell that corresponds to the far range with a sampling frequency of $f_s = 1/T_s$. The signals are also sampled in the azimuth dimension with a sampling frequency of $f_p = \mathrm{PRF}$. The discrete time version of the received signals can be expressed as the following:

$$z_{1,i}[n_t, n_a] = \sum_{l=0}^{L-1} \underbrace{(h_{11,i}[l, n_a] + h_{21,i,2d}[l, n_a] + + h_{31,i,d}[l, n_a])}_{h_{1,i}[l, n_a]} x[n_t - l] + w_1[n_t] \tag{6.6}$$

$$z_{2,i}[n_t, n_a] = \sum_{l=0}^{L-1} \underbrace{(h_{12,i,d}[l, n_a] + h_{22,i}[l, n_a] + h_{32,i,2d}[l, n_a])}_{h_{2,i}[l, n_a]} x[n_t - l] + w_2[n_t] \tag{6.7}$$

$$z_{3,i}[n_t, n_a] = \sum_{l=0}^{L-1} \underbrace{(h_{13,i,d}[l, n_a] + h_{23,i,2d}[l, n_a] + h_{33,i}[l, n_a])}_{h_{3,i}[l, n_a]} x[n_t - l] + w_3[n_t] \tag{6.8}$$

where,

$$h_{mn,i}[l, n_a] = \underbrace{\sigma_l e^{-j2\pi F_c \tau_{l,mn}(n_a)}}_{h_{mn}[l,n_a]} a_i(\phi_l), \tag{6.9}$$

$$h_{mn,i,\alpha d}[l, n_a] = h_{mn,i}[l - \alpha l_d, n_a], \tag{6.10}$$

$l_d = t_d/T_s$, n_t and n_a are the range and azimuth time indices, respectively.

6.3 Azimuth Ambiguity Removal and Image Formation

The effective sampling frequency in the azimuth dimension is $\mathrm{PRF} = B_d/(MN)$ so it is expected that the received signals will be aliased in the azimuth dimension. It should be borne in mind that the Doppler bandwidth of each of the received signals expressed in (6.6), (6.7) and (6.8) is B_d/N which corresponds to the receiving beamwidth.

The aliased Doppler spectrum of the signal received at a given receiver can be perfectly reconstructed if there are M independent representations of the aliased signal as stated in the multi-aperture reconstruction algorithm [72]. In our proposed configuration, the $M = 3$ independent representations of the impulse response measured from the first receiver are $h_{11,i}$, $h_{21,i}$ and $h_{31,i}$ which can be used to reconstruct the aliased Doppler spectrum that corresponds to the first receiving beamwidth. Similarly, the $M = 3$ independent representations of the impulse response measured from the second and third receivers can be obtained to reconstruct the Doppler spectra of the impulse responses measured from the second and third receivers, respectively. The locations of the phase centres that correspond to different Doppler bandwidths are illustrated in Fig.6.3. The phase centres overlapped spatially, in the proposed MIMO SAR configuration, are independent (i.e. carries different information) because the echoes corresponding to each of the overlapped phase centres occupy a different Doppler bandwidth as shown in Fig.6.4 unlike the case of the conventional MIMO SAR in which the echoes corresponding to all phase centres share the same Doppler bandwidth.

The separation of the impulse responses that correspond to different phase centres can be done by digital beamforming (DBF) in elevation on receive by exploiting the one to one relationship between time delay and elevation angle in a side-looking radar imaging geometry [68][92][67][71]. This relation results in that echoes corresponding to different transmitted subpulses (i.e. phase centres) arrive at each instant of time from different elevation angles.

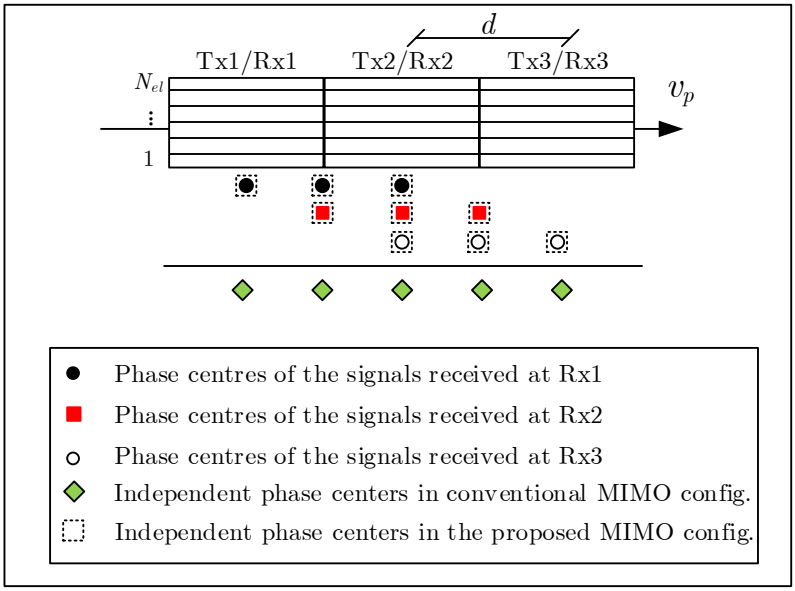

Figure 6.3: *Locations of the effective phase centres at different receivers. Each group of the phase centres occupies a portion of the total Doppler bandwidth which makes the overlapping phase centres independent (i.e. carries different information).*

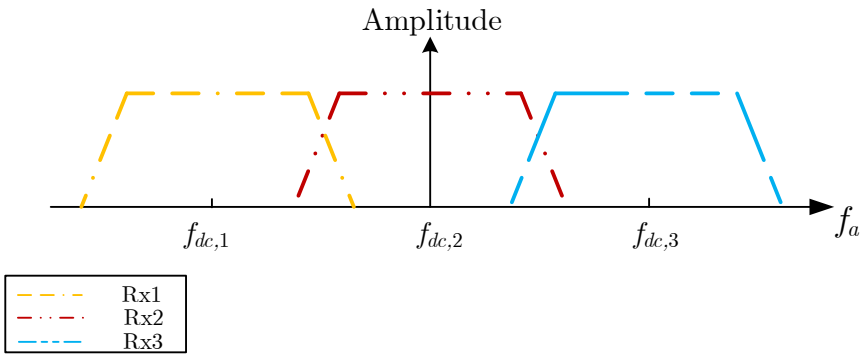

Figure 6.4: *Spectral distribution of the echo signal in each receiving beam in the proposed MIMO SAR configuration.* $f_{dc,n}$ *denotes the Doppler centroid of the echo signal in the* nth *receiver.*

Finally, the reconstructed Doppler bandwidth of the receivers should be combined to form the full Doppler bandwidth B_d as explained next.

6.3.1 Impulse Response Estimation and DBF in Elevation

The impulse responses $h_{1,i}$, $h_{2,i}$ and $h_{3,i}$ in (6.6), (6.7) and (6.8) will be estimated individually using our proposed FDSI-based estimation algorithm. It should be noted that each of the impulse responses $h_{1,i}$, $h_{2,i}$ and $h_{3,i}$ occupies a portion of the total Doppler bandwidth. Accordingly, the Doppler bandwidths need to be combined after removing the azimuth ambiguity to form the full Doppler bandwidth.

The received signals in (6.6), (6.7) and (6.8) can be written in a matrix form for a given azimuth bin as ($\forall n = 1, 2, 3$)

$$\begin{aligned}\mathbf{z}_{n,i}[n_a] &= \left[z_{n,i}[0, n_a], z_{n,i}[1, n_a], ..., z_{n,i}[K + L - 1, n_a]\right]^T \\ &= \mathbf{X}\mathbf{h}_{n,i}[n_a] + \mathbf{w}_n[n_a]\end{aligned} \tag{6.11}$$

where K is the length of the waveform transmitted. The matrix $\mathbf{X}$ can be made circulant and accordingly, the channel impulse response $\mathbf{h}_{n,i}[n_a]$ is zero padded by $(K-1)$ as the following:

$$\mathbf{z}_{n,i}[n_a] = \mathbf{X}_C \underbrace{\begin{bmatrix}\mathbf{h}_{n,i}[n_a] \\ \mathbf{0}_{(K-1)}\end{bmatrix}}_{\mathbf{h}_{n,i,p}[n_a]} + \mathbf{w}_n[n_a] \tag{6.12}$$

The channel impulse responses can be estimated as the following ($\forall n = 1, 2, 3$):

$$\hat{\mathbf{h}}_{n,i,p}[n_a] = \mathbf{X}_C^{-1}\mathbf{z}_{n,i}[n_a] \tag{6.13}$$

The impulse response estimation described above should be performed for all azimuth bins and all elevation channels.

The estimated impulse responses for all elevation channels ($\forall i = 0, 1, ..., N_{\text{el}} - 1$) at a given

range and azimuth bin can be expressed as the following:

$$\begin{aligned}\mathbf{h}_1[l,n_a] &= [h_{1,0}[l,n_a], h_{1,1}[l,n_a], ..., h_{1,(N_{\text{el}}-1)}[l,n_a]]^T \\ &= \underbrace{[\mathbf{a}(\phi_l) \quad \mathbf{a}(\phi_{l-2l_d}) \quad \mathbf{a}(\phi_{l-l_d})]}_{\mathbf{A}_1(\phi_l)} \begin{bmatrix} h_{11}[l,n_a] \\ h_{21,2d}[l,n_a] \\ h_{31,d}[l,n_a] \end{bmatrix} \end{aligned} \tag{6.14}$$

$$\begin{aligned}\mathbf{h}_2[l,n_a] &= [h_{2,0}[l,n_a], h_{2,1}[l,n_a], ..., h_{2,(N_{\text{el}}-1)}[l,n_a]]^T \\ &= \underbrace{[\mathbf{a}(\phi_{l-l_d}) \quad \mathbf{a}(\phi_l) \quad \mathbf{a}(\phi_{l-2l_d})]}_{\mathbf{A}_2(\phi_l)} \begin{bmatrix} h_{12,d}[l,n_a] \\ h_{22}[l,n_a] \\ h_{32,2d}[l,n_a] \end{bmatrix} \end{aligned} \tag{6.15}$$

$$\begin{aligned}\mathbf{h}_3[l,n_a] &= [h_{3,0}[l,n_a], h_{3,1}[l,n_a], ..., h_{3,(N_{\text{el}}-1)}[l,n_a]]^T \\ &= \underbrace{[\mathbf{a}(\phi_{l-l_d}) \quad \mathbf{a}(\phi_{l-2l_d}) \quad \mathbf{a}(\phi_l)]}_{\mathbf{A}_2(\phi_l)} \begin{bmatrix} h_{13,d}[l,n_a] \\ h_{23,2d}[l,n_a] \\ h_{33}[l,n_a] \end{bmatrix} \end{aligned} \tag{6.16}$$

where,

$$\mathbf{a}(\phi_l) = [a_0(\phi_l), a_1(\phi_l), ..., a_{N_{\text{el}}-1}(\phi_l)]^T \tag{6.17}$$

The corresponding impulse responses to each transmitter can be separated from $\mathbf{h}_n[l,n_a]$ by multiplying it with the weight matrix $\mathbf{W}_n(\phi_l)$ which can be obtained based on linearly constrained minimum variance (LCMV) beamformer algorithm [65] as the following ($\forall n = 1,2,3$):

$$\mathbf{W}_n(\phi_l) = (\mathbf{A}_n^H(\phi_l)\mathbf{A}_n(\phi_l))^{-1}\mathbf{A}_n^H(\phi_l) \tag{6.18}$$

The impulse responses are separated for all azimuth and range bins. The delay in $h_{mn,\alpha d}[l,n_a]$ can be easily compensated for in the range frequency domain by multiplying it with $e^{j2\pi f_r \alpha t_d}$ to obtain $h_{mn}[l,n_a]$ where f_r is the range frequency.

6.3.2 Azimuth Ambiguity Removal and Image Formation

As described previously, the impulse responses h_{1n}, h_{2n} and h_{3n} ($\forall n = 1,2,3$) occupy only a portion ($B_d/N = B_d/3$) of the total Doppler bandwidth which corresponds to the receiving beamwidth. The Doppler spectra of impulse responses are aliased as the effective sampling frequency in the azimuth dimension is assumed to be ($\text{PRF} = B_d/(MN) = B_d/9$). The

azimuth ambiguity removal of the Doppler spectra that correspond to the first receiving beam (i.e. $n = 1$) will be considered now.

The Fourier transform of h_{11}, h_{21} and h_{31} across both azimuth and range dimensions can be expressed using the principle of displaced phase centre (DPC) [14] as the following:

$$H_{11}(f_r, f_a) = H_{31}(f_r, f_a) \underbrace{e^{j2\pi d f_a / v_p} e^{j2\pi d^2/(\lambda R_l)}}_{Q_1(f_a)} \tag{6.19}$$

$$H_{21}(f_r, f_a) = H_{31}(f_r, f_a) \underbrace{e^{j\pi d f_a / v_p} e^{j3\pi d^2/(2\lambda R_l)}}_{Q_2(f_a)} \tag{6.20}$$

$$H_{31}(f_r, f_a) = H_{31}(f_r, f_a) \times \underbrace{1}_{Q_3(f_a)} \tag{6.21}$$

The aliased signals of $H_{m1}(f_r, f_r)$ can be expressed as the following ($\forall m = 1, 2, 3$):

$$\begin{aligned} \tilde{H}_{m1}(f_r, f_a) &= \sum_{k=-\infty}^{\infty} H_{m1}(f_r, f_a + k f_p) \\ &= \sum_{k=-\infty}^{\infty} H_{31}(f_r, f_a + k f_p) Q_m(f_a + k f_p) \end{aligned} \tag{6.22}$$

The aliased Doppler spectrum is divided into M intervals (i.e. $M = 3$) as shown in Fig.6.5, namely, I_1, I_2 and I_3 whose centre frequencies can be obtained using the following equation [95]:

$$f_{a,cj} = \big(-\frac{M}{2} - 0.5 + j \big) \mathrm{PRF} + f_{dc,n}, \quad \forall j = 1, 2, ..., M \tag{6.23}$$

where $f_{dc,n}$ is the Doppler centroid of the nth receiver (i.e. $n = 1$ for the first receiver) which is a function of the squint angle. It is possible for each Doppler interval to weight and combine $\tilde{H}_{11}(f_r, f_a)$, $\tilde{H}_{21}(f_r, f_a)$ and $\tilde{H}_{31}(f_r, f_a)$ in such a way that the original spectrum $H_{31}(f_r, f_a)$ is recovered while the back-folded component is removed as expressed in the following equations for the interval I_1:

$$P_{11}(f_a)\tilde{H}_{11}(f_r, f_a) + P_{21}(f_a)\tilde{H}_{21}(f_r, f_a) + P_{31}(f_a)\tilde{H}_{31}(f_r, f_a) = 3H_{31}(f_r, f_a) \tag{6.24}$$

$$P_{11}(f_a)\tilde{H}_{11}(f_r, f_a + f_p) + P_{21}(f_a)\tilde{H}_{21}(f_r, f_a + f_p) + P_{31}(f_a)\tilde{H}_{31}(f_r, f_a + f_p) = 0 \tag{6.25}$$

$$P_{11}(f_a)\tilde{H}_{11}(f_r, f_a + 2f_p) + P_{21}(f_a)\tilde{H}_{21}(f_r, f_a + 2f_p) + P_{31}(f_a)\tilde{H}_{31}(f_r, f_a + 2f_p) = 0 \tag{6.26}$$

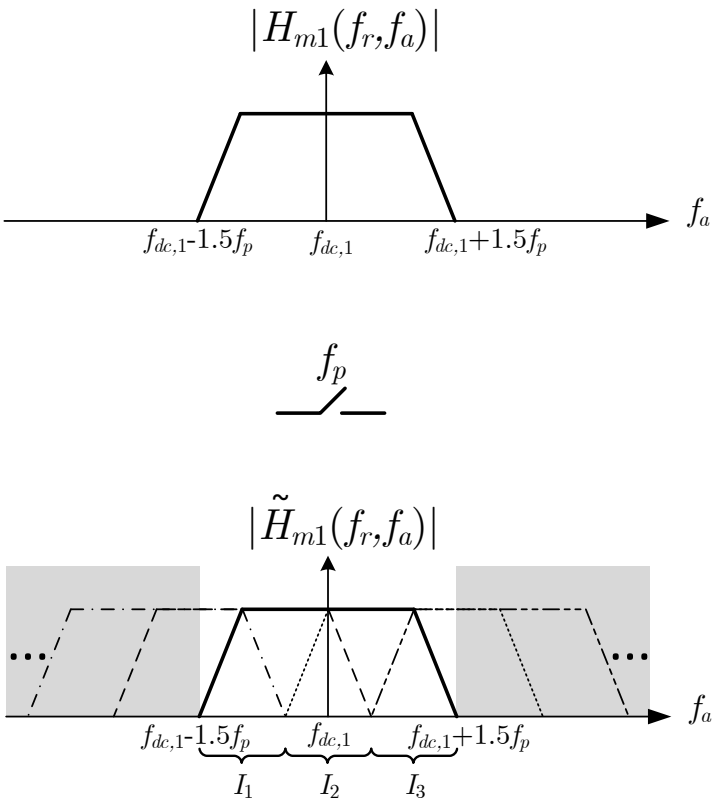

Figure 6.5: *The spectrum of the impulse response estimated at the first receiver when the transmitted signal is emitted by the* mth *transmitter before and after sampling with* $f_p = \mathrm{PRF}$. $f_{dc,1}$ *is the Doppler centroid of the first receiver. The Doppler bandwidth of each receiver is assumed to be* $3\mathrm{PRF}$.

For interval I_2 after shifting to I_1 to allow for setting up the linear systems,

$$P_{12}(f_a+f_p)\tilde{H}_{11}(f_r,f_a+f_p)+P_{22}(f_a+f_p)\tilde{H}_{21}(f_r,f_a+f_p)+P_{32}(f_a+f_p)\tilde{H}_{31}(f_r,f_a+f_p) = 3H_{31}(f_r,f_a+f_p) \tag{6.27}$$

$$P_{12}(f_a+f_p)\tilde{H}_{11}(f_r,f_a)+P_{22}(f_a+f_p)\tilde{H}_{21}(f_r,f_a)+P_{32}(f_a+f_p)\tilde{H}_{31}(f_r,f_a)=0 \tag{6.28}$$

$$P_{12}(f_a+f_p)\tilde{H}_{11}(f_r,f_a+2f_p)+P_{22}(f_a+f_p)\tilde{H}_{21}(f_r,f_a+2f_p)+P_{32}(f_a+f_p)\tilde{H}_{31}(f_r,f_a+2f_p) = 0 \tag{6.29}$$

For interval I_3 after shifting to I_1,

$$P_{13}(f_a+2f_p)\tilde{H}_{11}(f_r,f_a+2f_p)+P_{23}(f_a+2f_p)\tilde{H}_{21}(f_r,f_a+2f_p)+ P_{33}(f_a+2f_p)\tilde{H}_{31}(f_r,f_a+2f_p)=3H_{31}(f_r,f_a+2f_p) \tag{6.30}$$

$$P_{13}(f_a+2f_p)\tilde{H}_{11}(f_r,f_a+f_p)+P_{23}(f_a+2f_p)\tilde{H}_{21}(f_r,f_a+f_p) + P_{33}(f_a+2f_p)\tilde{H}_{31}(f_r,f_a+f_p)=0 \tag{6.31}$$

$$P_{13}(f_a+2f_p)\tilde{H}_{11}(f_r,f_a)+P_{23}(f_a+2f_p)\tilde{H}_{21}(f_r,f_a)+ P_{33}(f_a+2f_p)\tilde{H}_{31}(f_r,f_a)=0 \tag{6.32}$$

The reconstruction filters can be computed as the following:

$$\mathbf{P}(f_a)=3\mathbf{Q}^{-1}(f_a) \tag{6.33}$$

where,

$$\mathbf{Q}(f_a)=\begin{bmatrix} Q_1(f_a) & Q_2(f_a) & Q_3(f_a) \\ Q_1(f_a+f_p) & Q_2(f_a+f_p) & Q_3(f_a+f_p) \\ Q_1(f_a+2f_p) & Q_2(f_a+2f_p) & Q_3(f_a+2f_p) \end{bmatrix} \tag{6.34}$$

$$\mathbf{P}(f_a)=\begin{bmatrix} P_{11}(f_a) & P_{12}(f_a+f_p) & P_{13}(f_a+2f_p) \\ P_{21}(f_a) & P_{22}(f_a+f_p) & P_{23}(f_a+2f_p) \\ P_{31}(f_a) & P_{32}(f_a+f_p) & P_{33}(f_a+2f_p) \end{bmatrix} \tag{6.35}$$

I_1, I_2 and I_3 are then concatenated to obtain the original spectrum $H_{31}(f_r,f_a)$. Similarly, the original spectrum $H_{22}(f_r,f_a)$ is reconstructed using the aliased spectra of $\tilde{H}_{m2}(f_r,f_a)$ and the original spectrum of $H_{12}(f_r,f_a)$ is reconstructed from the aliased spectra of $\tilde{H}_{m3}(f_r,f_a)$ ($\forall m=1,2,3$).

The impulse responses $H_{rx,1}(f_r,f_a)=H_{31}(f_r,f_a)$, $H_{rx,2}(f_r,f_a)=H_{22}(f_r,f_a)$ and $H_{rx,3}(f_r,f_a)=$

$H_{13}(f_r, f_a)$ have the same phase centre but each occupies a portion of the total Doppler bandwidth. The Doppler centroids of $H_{rx,1}(f_r, f_a)$, $H_{rx,2}(f_r, f_a)$ and $H_{rx,3}(f_r, f_a)$ are functions of the squint angles θ_1, θ_2 and θ_2, respectively. The full Doppler bandwidth is then synthesised as described in Chapter 4, which is repeated here for clarity, before forming the image by performing the following steps:

1. The data of each receiving beam after RCMC is converted into range time-Doppler domain.
2. The data of each receiving beam is then zero-padded in the Doppler dimension so that the points of each Doppler spectrum are increased by a factor of N.
3. Each zero-padded data is then frequency shifted in the Doppler dimension by the corresponding Doppler centroid to compensate for the Doppler shift introduced by the squint angle.
4. The data of all receiving beams are then added together to form the full Doppler bandwidth spectrum.

The resulted full Doppler bandwidth data is then used to form the image (i.e. perform azimuth compression). A schematic of the proposed configuration implementation is shown in Fig.6.6.

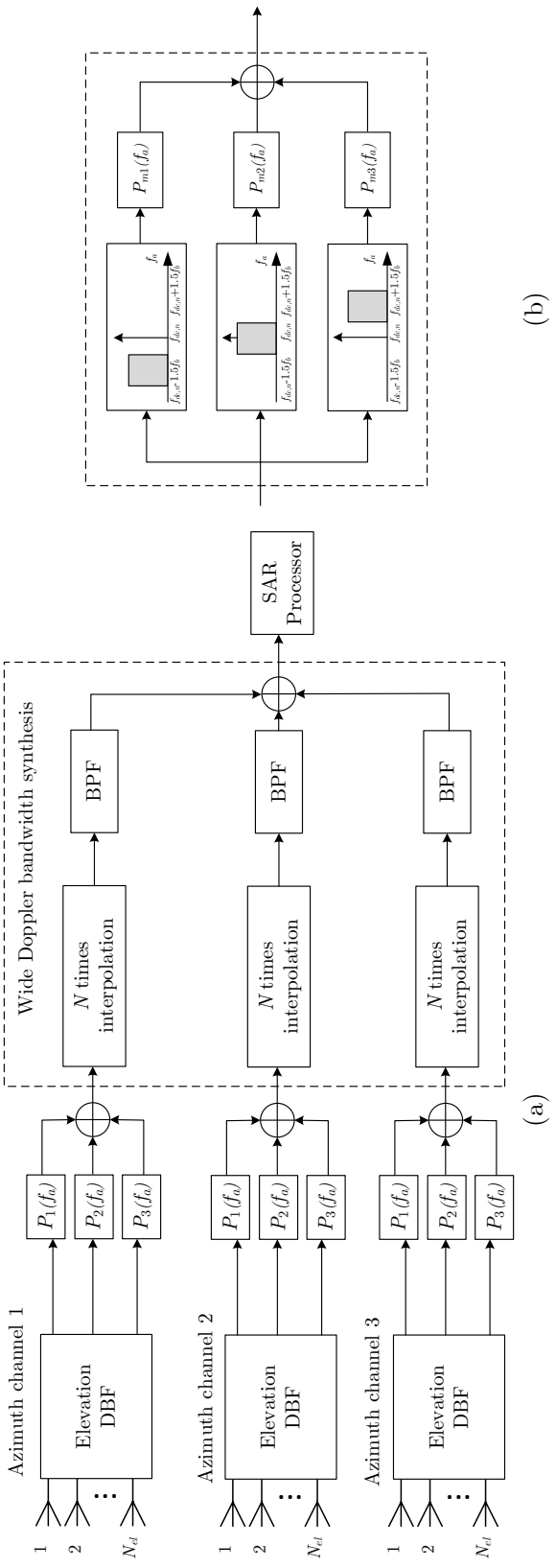

Figure 6.6: *(a)A schematic of the proposed configuration implementation where the elevation DBF block is as shown in Fig.2.16. (b) A schematic of the spatial filters bank $P_m(f_a)$ which is computed using* (6.33)*. Image formation algorithm is performed in SAR processor block.*

6.3.3 Azimuth Ambiguity Analysis

In the proposed MIMO SAR configuration, the receive beams of the channels are very close to each other in azimuth. Accordingly, the sidelobes of the receive beams will overlap with mainlobes of the adjacent azimuth beams which would degrade the performance of the azimuth ambiguity to signal ratio (AASR).

The azimuth ambiguity consists of two components in which the first one is the same as the conventional SISO SAR, whereas the second component is a result of the echoes which correspond to the signals emitted by the other beams. The AASR is the same as the one defined in Section 2.4.3 but with Δ_{mn} equals to one when the waveforms emitted by all transmitters are the same (i.e. LFM waveform). The AASR can be improved when short-term shift orthogonal waveforms (STSOW) [84] described in Section 2.5.1 are used in such a way that when a given transmitter (i.e. $\mathrm{Tx1}$) emits a conventional LFM chirp, the next adjacent transmitter (i.e. $\mathrm{Tx2}$) emits the same conventional LFM chirp but with sufficient offset in its instantaneous frequencies. The factor Δ_{mn} in this case can be expressed as

$$\Delta_{mn} = \begin{cases} 0 & , x_n \neq x_m \\ 1 & , \text{Otherwise} \end{cases} \tag{6.36}$$

where x_m and x_n denote the waveforms transmitted at the $m\mathrm{th}$ and $n\mathrm{th}$ transmitters, respectively. The use of short-term shift orthogonal waveform will remove the effects of the receive beams sidelobes overlapping with the next adjacent mainlobes. The AASR will therefore be improved.

6.4 Simulation Results

The following section shows the numerical results of our proposed MIMO SAR configuration using an LFM waveform and compares it with a conventional MIMO SAR described in Table 6.1. The waveforms used from transmission in the conventional MIMO SAR are assumed to be perfectly orthogonal.

6.4.1 One Dimensional Echo Separation

Consider a scenario in which there are $M = 3$ transmit antennas, $N = 3$ receive antennas as shown in Fig.6.1, the number of elevation channels is $N_{\mathrm{el}} = 25$ and the channel impulse response length is $L = 4268$. The carrier Frequency F_c is $9GHz$ and the distance between adjacent Tx/Rx is assumed to be $4.5m$. The transmitted waveform is an LFM waveform with a bandwidth of $100MHz$ and the sampling frequency is $F_s = 200MHz$. The SNR in the simulation is assumed to be $40\mathrm{dB}$ and the timing diagram of the transmission is as shown in Fig.6.2. Assume that there are three scatterers separated by a delay difference of $t_d = 3\mu s$ which is the same as the pulsewidth. This scenario (i.e. in which only the range dimension is considered) is presented to demonstrate how the received signals that correspond to different phase centres are separated at the receiver using digital beamforming (DBF) in elevation.

The received signal before and after estimating the impulse response at the first receiver are shown in Fig.6.7(a) and Fig.6.7(b), respectively, where one can see that the impulse responses corresponding to different phase centres are overlapped. The separation is possible because echoes corresponding to different subpulses (at each instant of time) arrive from different elevation angles. The separated impulse responses without delay compensation whose phase centres are located at the centre of Tx1/Rx1, at the centre of Tx2/Rx2 and midway between Tx1/Rx1 and Tx2/Rx2 are shown in Fig.6.7(c), Fig.6.7(d) and Fig.6.7(e), respectively.

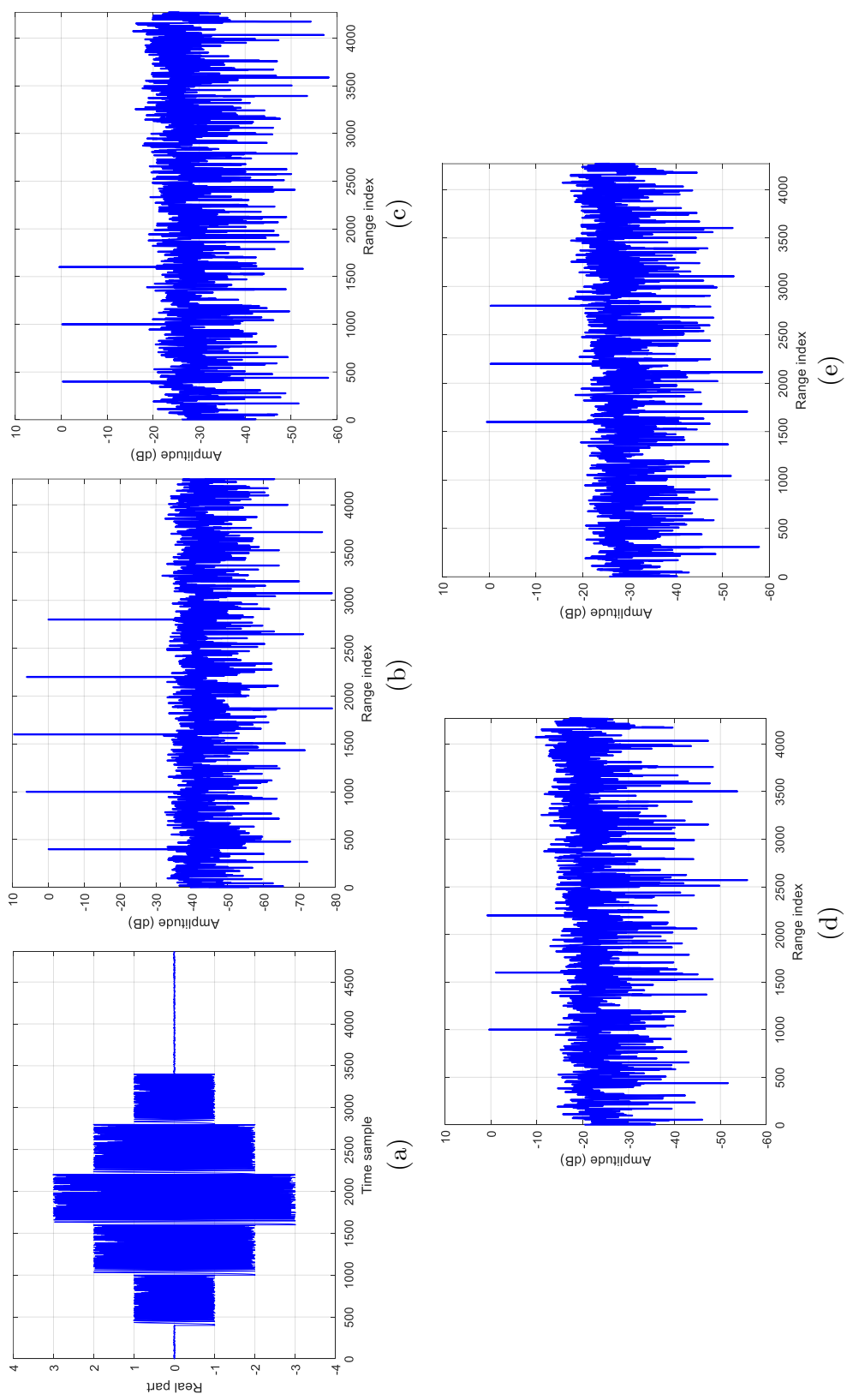

Figure 6.7: *One dimensional echo separation: (a)the real part of the received signal, (b)the estimated impulse response before DBF in elevation, (c)the separated impulse response whose phase centre is located at the centre of Tx1/Rx1, (d)the separated impulse response whose phase centre is located at the centre of Tx2/Rx2 and (e)the separated impulse response whose phase centre is located midway between Tx1/Rx1 and Tx2/Rx2.*

Parameter	Symbol	Value
Number of Tx (Rx)	M (N)	3
Min. distance to the swath centre	R_0	$20km$
Look angle	ϕ_r	45^o
Azimuth length of the conventional MIMO SAR beamformer	L_a	$1.5m$
Azimuth length of the proposed MIMO SAR beamformer	$L_{a,\text{prop}}$	$4.5m$
Distance between adjacent Tx/Rx in (proposed) MIMO SAR	(d_{prop}) d	$(4.5m)$ $1.5m$
Doppler bandwidth	B_d	$300Hz$
Pulse repetition frequency	f_p	$34Hz$
Platform Velocity	v_p	$225m/s$
Carrier Frequency	F_c	$4.5GHz$
Sampling Frequency	F_s	$200MS/s$
Single waveform Bandwidth	BW	$100MHz$
Number of elevation channels	N_{el}	20
Pulse width	τ	$2.5\mu s$

Table 6.1: *Simulation Parameters*

6.4.2 Azimuth Ambiguity Removal

Consider the simulation parameters listed in Table.6.1 and assume that there are two adjacent scatterers located at the swath centre. The transmitted waveform is an LFM waveform with a bandwidth of $100MHz$ and the timing diagram of the transmission is as shown in Fig.6.2. The azimuth and range cuts at the scatterers locations for the noiseless case are as shown in Fig.6.8 and Fig.6.9, respectively. It is clear from Fig.6.8 that there is no azimuth aliasing using our proposed MIMO configuration even though the PRF used is $B_d/(MN) = B_d/9 \approx 34Hz$ unlike the case of the conventional MIMO SAR in which the minimum PRF should satisfy the inequality $\text{PRF}_{min} \geq (B_d/K_p = B_d/5)$ where K_p is the number of independent phase centres which is equal to $(M + N - 1)$ when the same antenna arrays are used for both transmission and reception. Accordingly, our proposed MIMO configuration outperforms the conventional MIMO SAR. It should be noted that it has been assumed that the waveforms used in the conventional MIMO SAR are perfectly orthogonal.

6.4.3 Azimuth Ambiguity to Signal Ratio

The azimuth ambiguity characteristics of the proposed MIMO SAR configuration due to the sidelobes of the narrow beams is compared with the azimuth ambiguity of the conventional

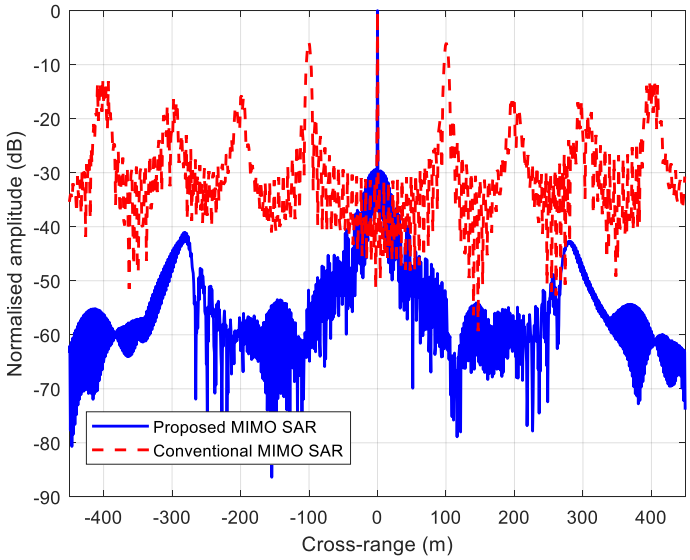

Figure 6.8: *Tha azimuth cut of a scatterer in the estimated scene using the proposed and conventional MIMO SAR.*

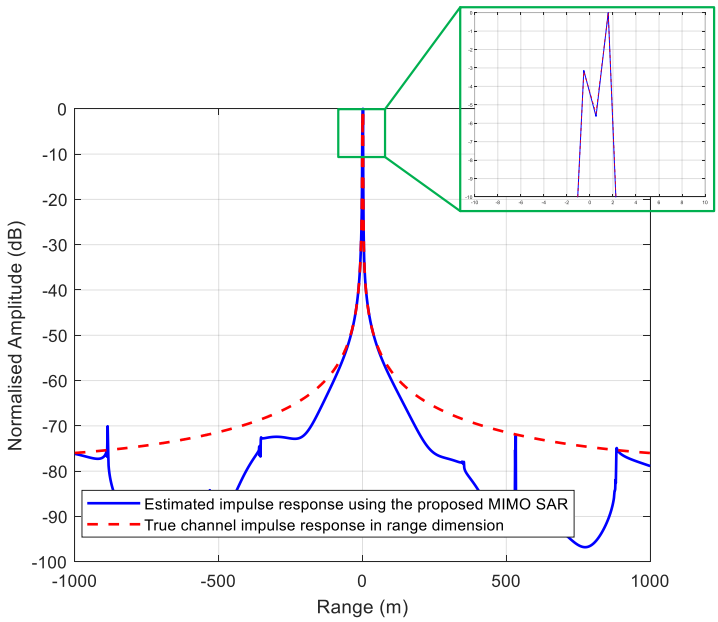

Figure 6.9: *The range cuts of the true channel impulse response (i.e. the original image at the true azimuth location) and the estimated one using the proposed configuration.*

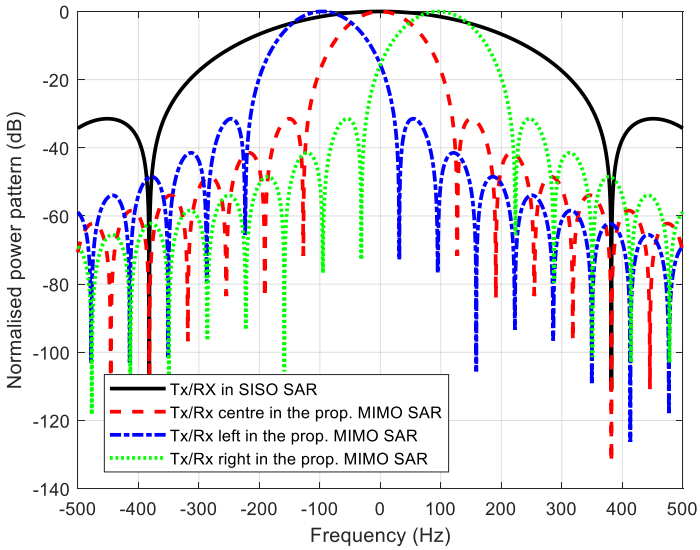

Figure 6.10: *Transmit and receive beam patterns of the proposed MIMO SAR and conventional SISO SAR as a function of frequency.*

SISO SAR based on AASR. Consider the beam patterns of the transmitters and receivers of the proposed MIMO SAR and conventional SISO SAR shown in Fig.6.10. The beam pattern of the conventional SISO SAR has been chosen in such a way that the cross-range resolution is the same as the one obtained in the proposed MIMO SAR.

The AASR as a function of PRF of the proposed MIMO SAR configuration with and without the use of short-term shift orthogonal waveforms (STSOW) is illustrated in Fig.6.11. Only one of the side beams is considered because the other side beam has the same azimuth ambiguity characteristics. The PRF in Fig.6.11 starts from $100Hz$ because it corresponds to the 3-dB Doppler bandwidth of one individual narrow beam (i.e. it is assumed that the aliasing of the Doppler spectrum of the individual narrow beams has been removed using the multi-aperture reconstruction algorithm described previously). The AASR of the conventional SISO SAR is shown in Fig.6.12.

One can see that the AASR in Fig.6.11 of the side beam is worse than that of the central beam because the power of desired signal component is lower than that of the central beam for the case when the same waveforms are used for transmission. In addition, the AASR of the central beam for the case of STSOW is the same as the one in the conventional SISO SAR.

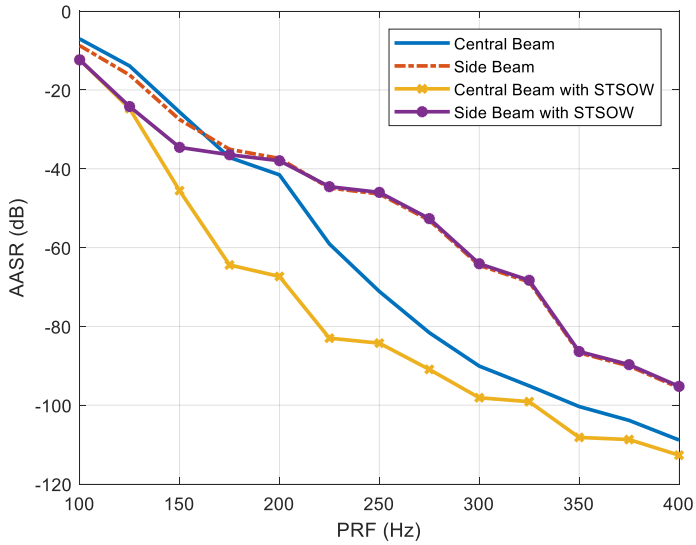

Figure 6.11: *Azimuth ambiguity characteristics of the proposed MIMO SAR with and without STSOW.*

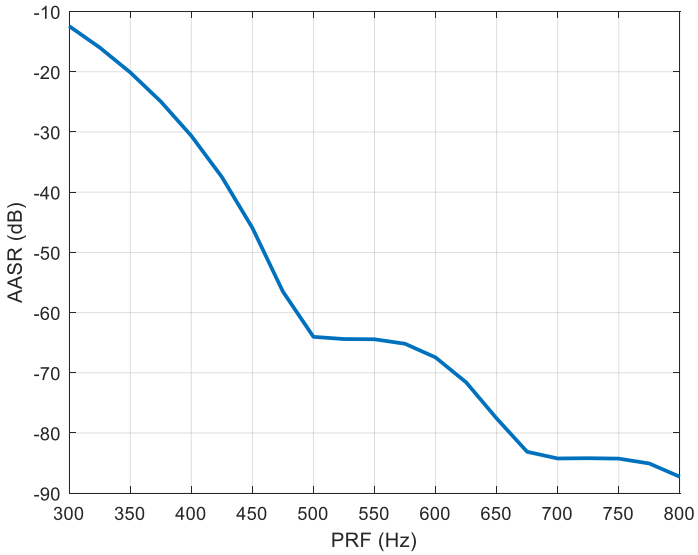

Figure 6.12: *Azimuth ambiguity characteristics of the conventional SISO SAR.*

6.4.4 Raw Data Simulation

A publicly available airborne SISO SAR data "Gotcha" [93] is used to construct MIMO SAR data to validate our proposed MIMO SAR configuration in a cluttered scene.

The process of constructing the raw data from the conventional SISO SAR raw data has been used in the literature [94]. Each receiver in the proposed MIMO SAR configuration occupies a portion of the total Doppler bandwidth. Therefore, the total azimuth angles are divided into N parts because each single azimuth angle corresponds to a single Doppler frequency. The following steps are performed on the received signals at the $n\mathrm{th}$ azimuth part which corresponds to the $n\mathrm{th}$ receiver to construct MIMO SAR data for the case when $M = N = 3$:

1. The data is transformed into Doppler domain and then multiplied by the corresponding slow time delay function to simulate the effective phase centre (EPC) and obtain the data received at the $n\mathrm{th}$ receiver when the signal is emitted by Tx1, Tx2 and Tx3.
2. The data that corresponds to each transmitter at the $n\mathrm{th}$ receiver are converted into the range-azimuth domain and convolved with the transmitted waveforms (i.e. the waveform transmitted by Tx2 and Tx3 are delayed versions of the one transmitted by Tx1).
3. Finally, the data at the $n\mathrm{th}$ receiver that corresponds to each transmitter are downsampled in the azimuth dimension by a factor of M to construct the MIMO SAR data received at the $n\mathrm{th}$ receiver.

It is assumed, for the sake of simplicity, that echoes correspond to each transmitter have been already separated at the receiver using DBF in elevation on receive as explained previously. In addition, the waveforms used in the conventional MIMO SAR are assumed to be perfectly orthogonal.

Consider the main system parameters listed in Table 6.2. It should be noted that the interbeams effect on the azimuth ambiguity is not considered here as it already has been addressed in Section 6.4.3. The formed images using a single receiver and all receivers of the proposed MIMO SAR configuration are shown in Fig.6.13 and Fig.6.14, respectively. The cross-range cuts of the indicated areas with red rectangles in the formed images are shown in Fig.6.15 where one can see that the formed image using all the receivers has better cross-range resolution than that of the formed image using a single receiver because only a portion of the Doppler bandwidth is utilised in the single receiver image.

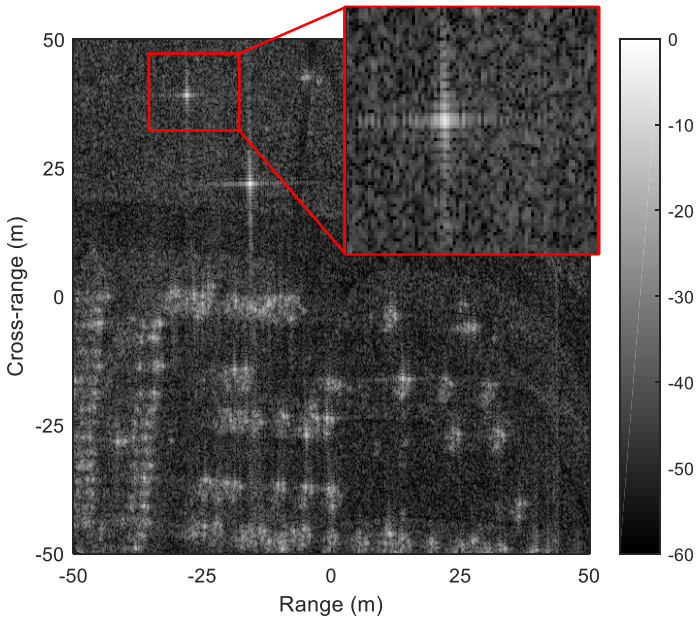

Figure 6.13: *Formed image using a single received data.*

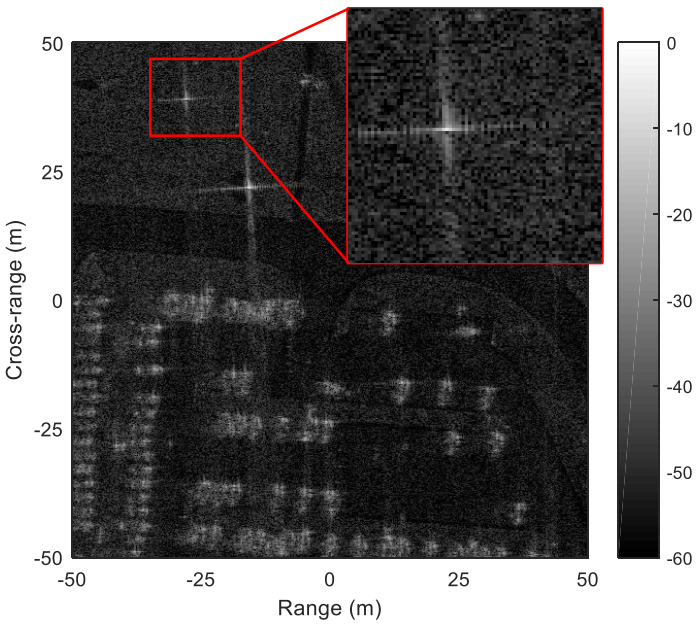

Figure 6.14: *Formed image using all received data in the proposed MIMO SAR.*

Parameter	Symbol	Value
Number of Tx (Rx)	$M(N)$	3
Min. distance to the swath centre	R_0	$10.158km$
3-dB width of a single receiver beamwidth in the proposed MIMO	θ_{BW}	2^o
3-dB width of a single receiver beamwidth in the conventional MIMO	$\theta_{BW,\text{conv}}$	6^o
distance between adjacent Tx/RX in the proposed MIMO	d	$4.5m$
distance between adjacent Tx/RX in the conventional MIMO	d_{conv}	$1.5m$
Carrier Frequency	F_c	$9.58GHz$
Single waveform Bandwidth	BW	$600MHz$

Table 6.2: *System Parameters*

Next, consider the case of the conventional MIMO SAR in which the sampling frequency across the azimuth dimension is the same as the one used in the proposed MIMO SAR configuration. The formed image of the conventional MIMO SAR is shown in Fig.6.16. It is clear from this figure that the image is completely aliased.

6.5 Conclusion

This chapter presents a new orthogonal waveform encoding MIMO SAR configuration with multiple contiguous azimuth beams to obtain high resolution wide swath imaging. The proposed configuration is independent of orthogonal waveforms used for transmission and it utilises all the phase centres including the overlapping ones which allows to use a lower operating PRF as compared with the conventional MIMO SAR. It is due to the multiple contiguous azimuth beams which makes the echoes, whose effective phase centres are overlapped, occupy different Doppler bandwidths. The waveforms used for transmission consist of a sequence of LFM waveforms which share the same bandwidth and have the same centre frequency. The use of conventional LFM waveforms simplifies implementations, hence, gains all the inherent benefits of this waveform (e.g. constant envelop and unity peak-to-average power ratio). Echoes corresponding to different phase centres are separated at the receiver using DBF on receive in elevation. Finally, simulation results of point targets and constructed raw data are used to validate the efficiency of the proposed configuration.

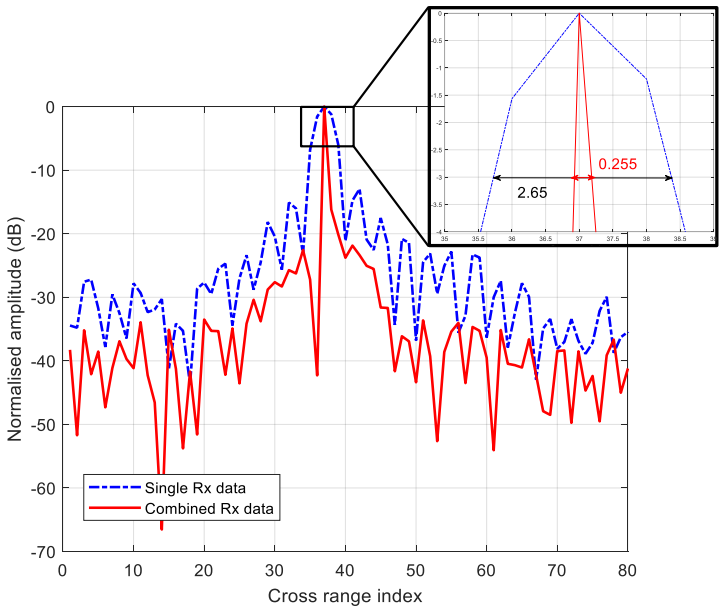

Figure 6.15: *Cross-range cuts of the indicated area with red rectangles in Fig.6.13 and Fig.6.14.*

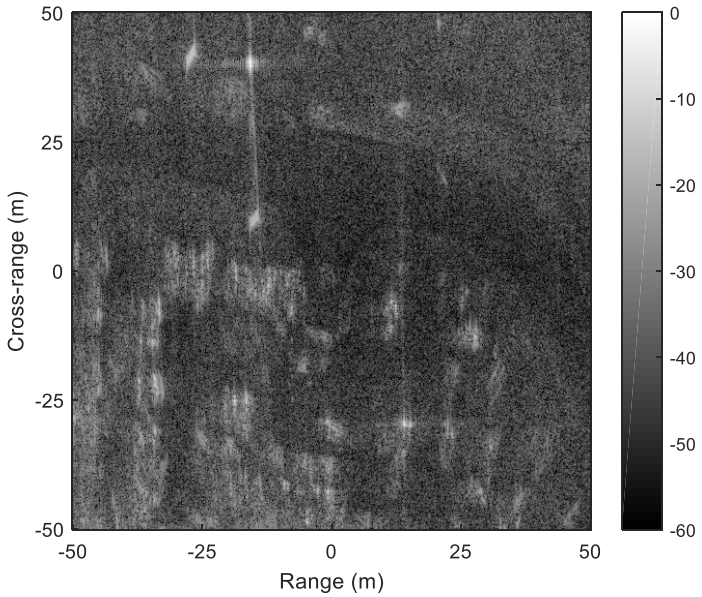

Figure 6.16: *Formed image using conventional MIMO SAR in which the azimuth sampling frequency is the same as the one used in the proposed MIMO SAR.*

Chapter 7
Conclusions

This thesis presents new configurations of two different MIMO SAR categories, namely, multiple subband MIMO SAR and orthogonal waveform encoding MIMO SAR.

In multiple subband MIMO SAR, the received signals in the proposed configurations are formulated as N MISO system identification problems using the principle of DPC, where N denotes the number of receivers. The echoes corresponding to all transmitted subband waveforms can be processed simultaneously without separating them at the receiver using a bank of BPFs (i.e. no guard bands are used among the spectra of the transmitted waveforms). As a result, the available bandwidth is utilised to maximum efficiency.

Each of the proposed multiple subband FDSI-MIMO SAR configurations has pros and cons. The main advantage of the BPF based FDSI-MIMO SAR over the conventional matched filter based MIMO SAR is the sidelobes minimisation of the estimated range profile because our proposed algorithm takes into account the fact that the spectrum of the combined subband waveforms is not flat unlike the case of the matched filter. The main advantages of the multiple-beam based FDSI-MIMO SAR over the BPF based FDSI-MIMO SAR are the full utilisation of the available bandwidth to maximum efficiency (i.e. no guard bands are used) and the improvement of the SNR due to the use of large transmit-receive antennas but these are the expense of the blind area enlargement and an increase of the system complexity due to the employment of DBF on receive in elevation for IBS. The FDSI-MIMO SAR proposed in Chapter 5 has an advantage over the multiple-beam based FDSI-MIMO SAR that no DBF in elevation on receive is required which simplifies the system complexity. Moreover, the blind area is smaller but this is at the expense of SNR because small transmit-receive antennas are used to illuminate the scene. In addition, The FDSI-MIMO SAR proposed in Chapter 5 has advantages over the BPF based FDSI-MIMO SAR that the available bandwidth is utilised to maximum efficiency and less computations are required for the azimuth ambiguity removal because the whole range bandwidth is processed at once unlike the case of the BPF based FDSI-MIMO SAR where each subband is processed individually. The pros and cons of the proposed multiple subband FDSI-MIMO SAR configurations are summarised in Table.7.1.

Configuration	Pros	Cons
BPF based FDSI-MIMO SAR (Chapter 3)	• Minimisation of range profile sidelobes. • No need for DBF on receive in elevation	• The need for guard bands • Small size transmit-receive antennas are required.
Multiple-beam based FDSI-MIMO SAR (Chapter 4)	• Minimisation of range profile sidelobes. • Improvement of SNR • Full bandwidth utilisation.	• Blind area enlargement. • Requirement of DBF in elevation.
FDSI-MIMO SAR (Chapter 5)	• Minimisation of range profile sidelobes. • No need for DBF on receive in elevation • Full bandwidth utilisation.	• Small size transmit-receive antennas are required

Table 7.1: *Pros and cons of the proposed multiple subband FDSI-MIMO SAR configurations*

The phase centres in conventional orthogonal waveform encoding MIMO SAR are not fully exploited as the spatially overlapping ones carry the same information (i.e. share the same Doppler bandwidth). As a result, only one of the overlapping phase centres can be used. In this thesis, a new configuration based on multiple contiguous azimuth beams is proposed which has the advantage that all of the phase centres, including the ones overlapped spatially, are forced to be independent (i.e. they carry different information) and, hence, all of them can be used to reduce the minimum required PRF to avoid aliasing in the azimuth dimension but this is at the expense of an increase of the complexity due to the use of DBF in elevation.

The received signals in all proposed configurations are processed as the solution to system identification problems using the principle of DPC which facilitates the use of LFM waveforms for transmission and, hence, gains all the inherent benefits of these waveforms. In addition, the impulse response in the range dimension is identified using an FDSI-based estimation algorithm instead of a matched filter and the length of the transmitted waveform is not a function of the channel impulse response length in the range dimension. This makes the proposed FDSI-algorithm suitable for stripmap SAR applications. Moreover, the estimated range profile using the proposed algorithm has the property of IRCI-free.

7.1 Recommendations and Future work

MIMO SAR provides a potential to HRWS imaging. The transmitting waveforms in orthogonal waveforms encoding MIMO SAR should be orthogonal which is similar to the case of a general MIMO radar but the mere use of orthogonal waveforms that share the same frequency bandwidth and time will only disperse (i.e. instead of suppressing) the ambiguous energy. As a result, the final image quality will be impaired by the cross-correlation noise. In addition, the waveforms used in general MIMO radars may not be suitable for the case of MIMO SAR which is generally placed in airplanes or satellites. One of the properties that MIMO SAR waveforms should have, in addition to the general MIMO radar waveforms properties, is a high average transmit power to reduce the required peak power requirement [96]. LFM-based waveforms with DBF in elevation on receive meet the requirements of MIMO SAR. However, the use of multiple channels in both azimuth and elevation increases the data rate and the system complexity. Furthermore, the heavy load and the wide bandwidth downlink may hinder the progress of MIMO SAR. These challenges will be resolved with the rapid development of electronic engineering and digital signal processing.

One possible direction of the future work is to extend the MIMO SAR configuration proposed in Chapter 6 to be applied in beam-space MIMO SAR to further exploit the availability of DBF in elevation and obtain an additional improvement in the swath width. This extension is appealing because the challenge of interbeams overlapping suppression is mitigated because of the way that beam-space MIMO SAR operates (i.e. different subswaths are illuminated by different subapertures in azimuth at a given subpulse).

Another potential direction of the future work is to investigate the possibility of using the proposed MIMO SAR configurations in ground moving target indication (GMTI) applications as only HRWS imaging applications are considered in the thesis. The configurations proposed in the thesis might outperform the conventional MIMO SAR configuration in GMTI applications because more phase centres can be utilised.

Throughout the thesis, the received signals of the proposed MIMO SAR configurations are formulated as system identification problems which are then used to estimate the impulse response in the range dimension using the proposed FDSI-based estimation algorithm. It is worthwhile to investigate the possibility to estimate the impulse response in the azimuth direction using an FDSI-based estimation algorithm. This might result in a two-dimensional IRCI-free estimated

impulse response.

Finally, only the colocated MIMO SAR is considered in this thesis. It is one of the potential directions of the future work to investigate the possibility of formulating the received signals of the distributed MIMO SAR which then can be used to identify the impulse response using the proposed FDSI-based algorithm. This might improve the formed image.

Appendix A

Proof of the Round Trip Distance of a Scatterer

Assume that the signal is transmitted by the $m\text{th}$ transmitter and received by the $n\text{th}$ receiver which is located at $y = 0$ (the platform is moving along the y axis). We will need to prove that the following equation holds:

$$R_{l,m}(\eta) + R_{l,n}(\eta) \approx 2R_{l,m}(\eta - \frac{\Delta y_{mn}}{2v_p})_{\theta=\theta_n} + \frac{\Delta y_{mn}^2}{4R_l} \tag{A.1}$$

$R_{l,m}$ and $R_{l,n}$ can be expressed using (2.68) as follows (it should be noted that the squint angle of the transmitter will be the same as the squint angle of the receiver):

$$R_{l,m}(\eta) \approx R_l - v_p \sin(\theta_n)(\eta + \frac{\Delta y_{mn}}{v_p}) + \frac{v_p^2 \cos^2(\theta_n)(\eta + \Delta y_{mn}/(v_p))^2}{2R_l} \tag{A.2}$$

$$R_{l,n}(\eta) \approx R_l - v_p \sin(\theta_n)(\eta) + \frac{v_p^2 \cos^2(\theta_n)(\eta)^2}{2R_l} \tag{A.3}$$

The round trip distance of the $l\text{th}$ scatterer can be expressed as follows:

$$\begin{aligned} f(\eta) =& R_{l,m}(\eta) + R_{l,n}(\eta) \\ =& 2R_l - 2v_p\eta \sin(\theta_n) - v_p \sin(\theta_n)(\Delta y_{mn}/v_p) + \\ & \frac{v_p^2 \cos^2(\theta_n)(\eta + \Delta y_{mn}/(v_p))^2}{2R_l} + \frac{v_p^2 \cos^2(\theta_n)(\eta)^2}{2R_l} \end{aligned} \tag{A.4}$$

Quadratic approximation of (A.4) can be expressed as follows:

$$f(\eta) \approx f(0) + \acute{f}(0)\eta + \frac{1}{2}\acute{\acute{f}}(0)\eta^2 \tag{A.5}$$

$$f(0) = 2R_l - v_p \sin(\theta_n)(\Delta y_{mn}/v_p) + \frac{v_p^2 \cos^2(\theta_n)(\Delta y_{mn}/v_p)^2}{2R_l} \tag{A.6}$$

$$\acute{f}(\eta) = -2v_p \sin(\theta_n) + \frac{2v_p^2 \cos^2(\theta_n)(\eta + \Delta y_{mn}/v_p)}{2R_l} + \frac{2v_p^2 \cos^2(\theta_n)\eta}{2R_l} \tag{A.7}$$

$$\acute{f}(0) = -2v_p \sin(\theta_n) + \frac{2v_p^2 \cos^2(\theta_n)(\Delta y_{mn}/v_p)}{2R_l} \tag{A.8}$$

$$\acute{\acute{f}}(\eta) = \frac{2v_p^2 \cos^2(\theta_n)}{R_l} = \acute{\acute{f}}(0) \tag{A.9}$$

Substituting (A.6)-(A.9) into (A.5)

$$\begin{aligned} f(\eta) \approx\ & 2R_l - v_p \sin(\theta_n)(\Delta y_{mn}/v_p) - 2v_p \eta \sin(\theta_n) \\ & + \frac{v_p^2 \cos^2(\theta_n)}{R_l}\left(\frac{1}{2}(\frac{\Delta y_{mn}}{v_p})^2 + (\frac{\Delta y_{mn}}{2v_p})^2 - (\frac{\Delta y_{mn}}{2v_p})^2 + 2(\frac{\Delta y_{mn}}{2v_p})\eta + \eta^2\right) \end{aligned} \tag{A.10}$$

$$\approx 2R_l - v_p \sin(\theta_n)(\Delta y_{mn}/v_p) - 2v_p \eta \sin(\theta_n) + \frac{v_p^2 \cos^2(\theta_n)}{R_l}(\frac{1}{4}(\frac{\Delta y_{mn}}{v_p})^2 + (\eta + \frac{\Delta y_{mn}}{2v_p})^2) \tag{A.11}$$

$$\approx 2R_{l,m}(\eta - \frac{\Delta y_{mn}}{2v_p})_{\theta=\theta_n} + \frac{(\Delta y_{mn}\cos(\theta_n))^2}{4R_l} \tag{A.12}$$

$$\approx 2R_{l,n}(\eta + \frac{\Delta y_{mn}}{2v_p})_{\theta=\theta_n} + \frac{(\Delta y_{mn}\cos(\theta_n))^2}{4R_l} \tag{A.13}$$

As the squint angles of the receivers are generally small, the following can be used:

$$\frac{(\Delta y_{mn}\cos(\theta_n))^2}{4R_l} \approx \frac{(\Delta y_{mn})^2}{4R_l} \tag{A.14}$$

Therefore,

$$\begin{aligned} f(\eta) =\ & R_{l,m}(\eta) + R_{l,n}(\eta) \\ \approx\ & 2R_{l,m}(\eta - \frac{\Delta y_{mn}}{2v_p})_{\theta=\theta_n} + \frac{(\Delta y_{mn})^2}{4R_l} \end{aligned} \tag{A.15}$$

$$\approx 2R_{l,n}(\eta + \frac{\Delta y_{mn}}{2v_p})_{\theta=\theta_n} + \frac{(\Delta y_{mn})^2}{4R_l} \tag{A.16}$$

Consider the geometry shown in Fig.4.1, the round trip distances can be expressed using (A.15) and (A.16) as follows:

$$R_{l,1}(\eta) + R_{l,2}(\eta) \approx 2R_{l,1}(\eta - \frac{d}{2v_p})_{\theta=\theta_{\mathrm{Rx}}} + \frac{(d)^2}{4R_l} \tag{A.17}$$

$$\approx 2R_{l,2}(\eta + \frac{d}{2v_p})_{\theta=\theta_{\mathrm{Rx}}} + \frac{(d)^2}{4R_l} \tag{A.18}$$

$$R_{l,2}(\eta) + R_{l,3}(\eta) \approx 2R_{l,2}(\eta - \frac{d}{2v_p})_{\theta=\theta_{\mathrm{Rx}}} + \frac{(d)^2}{4R_l} \tag{A.19}$$

$$\approx 2R_{l,3}(\eta + \frac{d}{2v_p})_{\theta=\theta_{\mathrm{Rx}}} + \frac{(d)^2}{4R_l} \tag{A.20}$$

$$R_{l,1}(\eta) + R_{l,3}(\eta) \approx 2R_{l,2}(\eta)_{\theta=\theta_{\mathrm{Rx}}} + \frac{(d)^2}{R_l} \tag{A.21}$$

References

[1] C. V. Jakowatz, D. E. Wahl, P. H. Eichel, D. C. Ghiglia, and P. A. Thompson, *Spotlight-Mode Synthetic Aperture Radar: A Signal Processing Approach*. 1996.

[2] T. Zhang and N. G. Xia, "OFDM Synthetic Aperture Radar Imaging with Sufficient Cyclic Prefix," *IEEE Transactions on Geoscience and Remote Sensing*, pp. 394–404, 2015.

[3] T. Zhang, X. G. Xia, and L. Kong, "IRCI Free Range Reconstruction for SAR Imaging with Arbitrary Length OFDM Pulse," *IEEE Transactions on Signal Processing*, pp. 4748–4759, 2014.

[4] Y. H. Cao and X. G. Xia, "IRCI-Free MIMO-OFDM SAR Using Circularly Shifted Zadoff-Chu Sequences," *IEEE Geoscience and Remote Sensing Letters*, vol. 12, no. 5, pp. 1126–1130, 2015.

[5] G. Min, W. Xiaoming, and H. Shunji, "Performance Improvements in MIMO SAR," in *2008 IEEE Radar Conference, RADAR 2008*, 2008.

[6] J. H. G. Ender and J. Klare, "System Architectures and Algorithms for Radar Imaging by MIMO-SAR," in *IEEE National Radar Conference - Proceedings*, 2009.

[7] W. Q. Wang, "Space-Time Coding MIMO-OFDM SAR for High-Resolution Imaging," *IEEE Transactions on Geoscience and Remote Sensing*, vol. 49, no. 8, pp. 3094–3104, 2011.

[8] X. Luo, R. Wang, Y. Deng, and W. Xu, "Influences of Channel Errors and Interference on The OFDM-MIMO SAR," in *2013 IEEE Radar Conference (RadarCon13)*, pp. 1–5, 2013.

[9] G. Jing, G. Sun, X. Xia, M. Xing, and Z. Bao, "A Novel Two-Step Approach of Error Estimation for Stepped-Frequency MIMO-SAR," *IEEE Geoscience and Remote Sensing Letters*, vol. 14, no. 12, pp. 2290–2294, 2017.

[10] G. Krieger, "MIMO-SAR: Opportunities and Pitfalls," *IEEE Transactions on Geoscience and Remote Sensing*, vol. 52, no. 5, pp. 2628–2645, 2014.

[11] W. Wang, "Near-Space Wide-Swath Radar Imaging With Multiaperture Antenna," *IEEE Antennas and Wireless Propagation Letters*, vol. 8, pp. 461–464, 2009.

[12] W. Wang, "Near-Space Vehicles: Supply a Gap Between Satellites and Airplanes for Remote Sensing," *IEEE Aerospace and Electronic Systems Magazine*, vol. 26, pp. 4–9, apr 2011.

[13] M. Alshaya, M. Yaghoobi, and B. Mulgrew, "Frequency Domain System Identification for High Resolution IRCI-Free Collocated MIMO Radar," in *The 15th European Radar Conference*, (Madrid), 2018.

[14] M. Alshaya, M. Yaghoobi, and B. Mulgrew, "Frequency Domain System Identification for Wide Swath High Resolution IRCI-Free MIMO SAR," in *2019 IEEE Radar Conference, RadarConf 2019*, 2019.

[15] M. Alshaya, M. Yaghoobi, and B. Mulgrew, "Stepped Frequency IRCI-free Sliding Spotlight MIMO SAR," in *EuRAD 2019 - 2019 16th European Radar Conference*, 2019.

[16] M. Alshaya, M. Yaghoobi, and B. Mulgrew, "Multiple-Beam IRCI-Free MIMO SAR," in *2019 International Radar Conference (Radar)*, (Toulon), 2019.

[17] M. Alshaya, M. Yaghoobi, and B. Mulgrew, "High-Resolution Wide-Swath IRCI-Free MIMO SAR," *IEEE Transactions on Geoscience and Remote Sensing*, pp. 1–13, 2019.

[18] M. AlShaya, M. Yaghoobi, and B. Mulgrew, "IRCI-Free Multiple-Subband MIMO SAR," in *IET Radar, Sonar & Navigation*, (Undergoing Review).

[19] M. Alshaya, M. Yaghoobi, and B. Mulgrew, "Resolution Enhancement in High Resolution Wide Swath MIMO SAR," in *2020 IEEE International Radar Conference*, (Washington DC), 2020.

[20] M. AlShaya, M. Yaghoobi, and B. Mulgrew, "Ultra High Resolution Wide Swath MIMO SAR," in *IEEE Journal of Selected Topics in Applied Earth Observations and Remote Sensing*, (Revised and Resubmitted).

[21] M. I. Skolnik, *Radar Handbook*. McGraw-Hill, 2008.

[22] M. AlShaya, *Spatiotemporal Arrayed MIMO Radar (MSc dissertation)*. Imperial College London, 2015.

[23] M. I. Skolnik, *Introduction to Radar Systems*. New York: McGraw-Hill, 3rd ed., 2002.

[24] D. Bliss and K. Forsythe, "Multiple-Input Multiple-Output (MIMO) Radar and Imaging: Degrees of Freedom and Resolution," *The Thrity-Seventh Asilomar Conference on Signals, Systems & Computers, 2003*, vol. 1, 2003.

[25] D. Rabideau and P. Parker, "Ubiquitous MIMO Multifunction Digital Array Radar," *The Thrity-Seventh Asilomar Conference on Signals, Systems & Computers, 2003*, vol. 1, 2003.

[26] A. M. Haimovich, R. S. Blum, and L. J. Cimini, "MIMO Radar with Widely Separated Antennas," *IEEE Signal Processing Magazine*, vol. 25, pp. 116–129, 2008.

[27] S. Gogineni and A. Nehorai, "Polarimetric MIMO Radar with Distributed Antennas for Target Detection," *IEEE Transactions on Signal Processing*, vol. 58, no. 3 PART 2, pp. 1689–1697, 2010.

[28] H. L. Van Trees, "Detection, Estimation, and Modulation Theory. Part 1 - Detection, Estimation, and Linear Modulation Theory.," *Most*, vol. 6, pp. 0–471, 1968.

[29] N. Levanon, *Radar Principles*. John Wiley & Sons, 1st ed., 1988.

[30] S. Imani, M. M. Nayebi, and S. A. Ghorashi, "Colocated MIMO Radar SINR Maximization Under ISL and PSL Constraints," *IEEE Signal Processing Letters*, vol. 25, pp. 422–426, mar 2018.

[31] L. Wu, P. Babu, and D. P. Palomar, "Transmit Waveform/Receive Filter Design for MIMO Radar With Multiple Waveform Constraints," *IEEE Transactions on Signal Processing*, vol. 66, pp. 1526–1540, mar 2018.

[32] J. Li and P. Stoica, "MIMO Radar - Diversity Means Superiority," in *MIMO Radar Signal Processing*, pp. 1–64, Wiley-IEEE Press, 2008.

[33] L. Xu, J. Li, and P. Stoica, "Adaptive Techniques for MIMO Radar," in *2006 IEEE Sensor Array and Multichannel Signal Processing Workshop Proceedings, SAM 2006*, pp. 258–262, 2006.

[34] P. Stoica, "Target Detection and Parameter Estimation for MIMO Radar Systems," *IEEE Transactions on Aerospace and Electronic Systems*, vol. 44, no. 3, pp. 927–939, 2008.

[35] K. W. Forsythe, D. W. Bliss, and G. S. Fawcett, "Multiple-Input Multiple-Output (MIMO) Radar: Performance Issues," *Conference Record of the ThirtyEighth Asilomar Conference on Signals Systems and Computers 2004*, vol. 1, pp. 310–315, 2004.

[36] W. Q. Wang and J. Cai, "Ground Moving Target Indication by MIMO SAR with Multi-Antenna in Azimuth," in *International Geoscience and Remote Sensing Symposium (IGARSS)*, pp. 1662–1665, 2011.

[37] W. Jian Li and Stoica, Petre and Luzhou Xu and Roberts, "On Parameter Identifiability of MIMO Radar," *Signal Processing Letters, IEEE*, vol. 14, pp. 968–971, 2007.

[38] I. Bekkerman and J. Tabrikian, "Spatially Coded Signal Model for Active Arrays," *2004 IEEE International Conference on Acoustics, Speech, and Signal Processing*, vol. 2, pp. 1–4, 2004.

[39] A. Manikas, *Differential Geometry in Array Processing*. London: Imperial College Presss, 2004.

[40] Y. H. Cao, X. G. Xia, and S. H. Wang, "IRCI Free Colocated MIMO Radar Based on Sufficient Cyclic Prefix OFDM Waveforms," *IEEE Transactions on Aerospace and Electronic Systems*, vol. 51, no. 3, pp. 2107–2120, 2015.

[41] W.-Q. Wang, *Multi-Antenna Synthetic Aperture Radar*. Boca Raton, FL, USA: CRC Press, Inc., 1st ed., 2017.

[42] C. Özdemir, *Inverse Synthetic Aperture Radar Imaging with MATLAB Algorithms*. John Wiley & Sons, 2012.

[43] N. Gebert, G. Krieger, and M. A. Moreira, "Digital Beamforming on Receive: Techniques and Optimization Strategies for High-Resolution Wide-Swath SAR Imaging," *IEEE Transactions on Aerospace and Electronic Systems*, vol. 45, no. 2, pp. 564–592, 2009.

[44] R. Yang, H. Li, S. Li, P. Zhang, L. Tan, X. Gao, and X. Kang, *High-Resolution Microwave Imaging*. Singapore: Springer, 2018.

[45] I. G. Cumming and W. F. H., *Digital Processing of Synthetic Aperture Radar Data: Algorithms and Implementation*. Boston: Artech House, 2005.

[46] A. Freeman, "On Ambiguities in SAR Design," in *EUSAR 2006: 6th European Conference on SAR, Germany*, 2006.

[47] D. P. Belcher and C. J. Baker, "High Resolution Processing of Hybrid Stripmap/Spotlight mode {SAR}," *IEE Proceedings Radar Sonar Navigation*, 1996.

[48] J. Mittermayer, R. Lord, and E. Borner, "Sliding Spotlight SAR Processing for TerraSAR-X Using a New Formulation of The Extended Chirp Scaling Algorithm," in *IGARSS 2003. 2003 IEEE International Geoscience and Remote Sensing Symposium. Proceedings (IEEE Cat. No.03CH37477)*, vol. 3, pp. 1462–1464, 2003.

[49] Y. Wang and D. Yao, "Analysis of Some Key Parameters in Sliding Spotlight SAR," in *2009 IET International Radar Conference*, pp. 1–4, 2009.

[50] Y. K. Chan and V. C. Koo, "An Introduction to Synthetic Aperture Radar (SAR)," *Progress In Electromagnetics Research B*, 2008.

[51] B. Mahafza, *Introduction to Radar Analysis*. New York: CRC Press, 1998.

[52] H. Mir, "Low-Rate Sampling Technique for Range-Windowed Radar/Sonar Using Nonlinear Frequency Modulation," *IEEE Transactions on Aerospace and Electronic Systems*, vol. 51, pp. 1972–1979, jul 2015.

[53] G. L. Turin, "An Introduction to Matched Filters," *IRE Transactions on Information Theory*, 1960.

[54] B. Mahafza, *Radar Systems Analysis and Design Using MATLAB*. CRC Press, 2000.

[55] J. Bergin and J. R. Guerci, *MIMO Radar: Theory and Application*. Boston: Artech House, 2018.

[56] T. Hwang, C. Yang, G. Wu, S. Li, and G. Y. Li, "OFDM and Its Wireless Applications: A Survey," *IEEE Transactions on Vehicular Technology*, 2009.

[57] D. Tse and V. Pramod, *Fundamentals of Wireless Communication*. 2005.

[58] C. Tierney, *Adaptive Waveform Design for SAR in a Crowded Spectrum*. PhD thesis, The University of Edinburgh, 2019.

[59] C. Tierney and B. Mulgrew, "Adaptive Waveform Design with Least-Squares System Identification for Interference Mitigation in SAR," in *2017 IEEE Radar Conference, RadarConf 2017*, pp. 0180–0185, 2017.

[60] C. Tierney and B. Mulgrew, "Adaptive waveform design for interference mitigation in SAR," *Signal Processing*, vol. 178, p. 107759, 2021.

[61] S. Sen and A. Nehorai, "Adaptive Design of OFDM Radar Signal With Improved Wideband Ambiguity Function," *IEEE Transactions on Signal Processing*, 2010.

[62] R. Bamler, "A Comparison of Range-Doppler and Wavenumber Domain SAR Focusing Algorithms," *IEEE Transactions on Geoscience and Remote Sensing*, 1992.

[63] A. Moreira, J. Mittermayer, and R. Scheiber, "Extended Chirp Scaling Algorithm for Air- and Spaceborne SAR Data Processing in Stripmap and ScanSAR Imaging Modes," *IEEE Transactions on Geoscience and Remote Sensing*, vol. 34, no. 5, pp. 1123–1136, 1996.

[64] W. Xu, Y. Deng, and R. Wang, "Multichannel Synthetic Aperture Radar Systems with a Planar Antenna for Future Spaceborne Microwave Remote Sensing," *IEEE Aerospace and Electronic Systems Magazine*, 2012.

[65] Harry L. Van Trees, *Optimum Array Processing: Part IV of Detection, Estimation, and Modulation Theory*. 2002.

[66] G. Krieger, N. Gebert, and A. Moreira, "Multidimensional Waveform Encoding: A New Digital Beamforming Technique for Synthetic Aperture Radar Remote Sensing," *IEEE Transactions on Geoscience and Remote Sensing*, 2008.

[67] M. Suess, B. Grafmueller, and R. Zahn, "A Novel High Resolution, Wide Swath SAR System," in *IGARSS 2001. Scanning the Present and Resolving the Future. Proceedings. IEEE 2001 International Geoscience and Remote Sensing Symposium (Cat. No.01CH37217)*, 2002.

[68] W. Xu, P. P Huang, and Y.-K. Deng, "Multi-channel SPCMB-Tops SAR for High-Resolution Wide-Swath Imaging," *Progress In Electromagnetics Research*, vol. 116, 2011.

[69] A. Grami, *Introduction to digital communications*. 2015.

[70] A. Currie and M. Brown, "Wide-Swath SAR," *IEE Proceedings F Radar and Signal Processing*, 2010.

[71] W. Xu, W. Xu, and Y. Deng, "Multichannel SAR With Reflector Antenna for High-Resolution Wide-Swath Imaging," *IEEE Antennas and Wireless Propagation Letters*, 2010.

[72] G. Krieger, N. Gebert, and A. Moreira, "High-Resolution Synthetic Aperture Side View Radar System Used by Means of Digital Beamforming," 2007.

[73] C. Cui, X. Liu, X. Dong, C. Hu, and Y. Li, "Moving target modelling and indication in MIMO GEO SAR," *The Journal of Engineering*, vol. 2019, no. 19, pp. 5529–5533, 2019.

[74] J. H. Kim, A. Ossowska, and W. Wiesbeck, "Experimental Investigation of Digital Beamforming SAR Performance Using a Ground-Based Demonstrator," in *International Geoscience and Remote Sensing Symposium (IGARSS)*, 2007.

[75] H. Dang, X. Zhang, Z. Liu, X. Zhang, and L. Zhou, "Research on Waveform Design and Imaging of MIMO-SAR," in *2019 IEEE International Conference on Signal, Information and Data Processing (ICSIDP)*, pp. 1–5, dec 2019.

[76] W. Q. Wang, "Mitigating Range Ambiguities in High-PRF SAR with OFDM Waveform Diversity," *IEEE Geoscience and Remote Sensing Letters*, vol. 10, no. 1, pp. 101–105, 2013.

[77] J. Wang, L. Chen, and X. Liang, "Orthogonal waveform separation based on echo compression for airborne MIMO-SAR systems," *The Journal of Engineering*, vol. 2019, no. 19, pp. 6336–6340, 2019.

[78] J. Wang, K. H. Zhu, L. N. Wang, X. D. Liang, and L. Y. Chen, "A novel orthogonal waveform separation scheme for airborne MIMO-SAR systems," *Sensors (Switzerland)*, 2018.

[79] F. Zhou, J. Ai, Z. Dong, J. Zhang, and M. Xing, "A novel MIMO–SAR solution based on azimuth phase coding waveforms and digital beamforming," *Sensors (Switzerland)*, 2018.

[80] H. Sun, F. Brigui, and M. Lesturgie, "Analysis and Comparison of MIMO Radar Waveforms," in *2014 International Radar Conference, Radar 2014*, 2014.

[81] J. P. Stralka, R. M. Thompson, J. Scanlan, and A. Jones, "MISO Radar Beamforming Demonstration," in *IEEE National Radar Conference - Proceedings*, 2011.

[82] P. P. Vaidyanathan and P. Pal, "MIMO Radar, SIMO Radar, and IFIR Radar: A Comparison," in *Conference Record - Asilomar Conference on Signals, Systems and Computers*, 2009.

[83] W. Wang, R. Wang, Y. Deng, L. Hou, W. Xu, and L. Guo, "A Processing Scheme for LFM-Based Waveform MIMO SAR with Digital Beam-Forming in Elevation," *Remote Sensing Letters*, vol. 6, no. 11, pp. 874–883, 2015.

[84] G. Krieger, M. Younis, S. Huber, F. Bordoni, A. Patyuchenko, J. Kim, P. Laskowski, M. Villano, T. Romme, P. Lopez-Dekker, and A. Moreira, "MIMO-SAR and The Orthogonality Confusion," in *International Geoscience and Remote Sensing Symposium (IGARSS)*, 2012.

[85] W. Xu, P. P Huang, and Y.-K. Deng, "MIMO-TOPS Mode for High-Resolution Ultra-Wide-Swath Full Polarimetric Imaging," *Progress In Electromagnetics Research*, vol. 121, 2011.

[86] Y. Sun, F. He, S. Zhou, F. Li, and Z. Tan, "Beam-Space Based MIMO SAR Digital Beamforming with Array-Fed Reflector Antennas," in *2018 19th International Radar Symposium (IRS)*, pp. 1–9, jun 2018.

[87] G. Jin, Y. Deng, W. Wang, R. Wang, Y. Zhang, and Y. Long, "Segmented Phase Code Waveforms: A Novel Radar Waveform for Spaceborne MIMO-SAR," *IEEE Transactions on Geoscience and Remote Sensing*, pp. 1–16, 2020.

[88] Z. M. Yang, M. D. Xing, G. C. Sun, and Z. Bao, "Joint multichannel motion compensation method for MIMO SAR 3D imaging," *International Journal of Antennas and Propagation*, 2015.

[89] J. Guo, J. Chen, C. Li, and W. Yang, "An Airborne Multi-Channel Sar Imaging Method with Motion Compensation," in *International Geoscience and Remote Sensing Symposium (IGARSS)*, 2019.

[90] F. Peng, H. Li, B. Cai, and D. Deng, "High resolution imaging with airborne MIMO-SAR," in *Proceedings of 2011 IEEE CIE International Conference on Radar*, vol. 1, pp. 862–866, oct 2011.

[91] X. Luo, Y. Deng, R. Wang, L. Guo, and M. Wang, "Correction of channel imbalance for MIMO SAR using stepped-frequency chirps," *International Journal of Antennas and Propagation*, 2014.

[92] N. Gebert, G. Krieger, and A. Moreira, "Multichannel Azimuth Processing in ScanSAR and TOPS Mode Operation," *IEEE Transactions on Geoscience and Remote Sensing*, 2010.

[93] "Gotcha Volumetric SAR Data Set, Version 1.0.."

[94] M. Xing, Z. Bao, F. Zhou, J. Zhang, and G. Sun, "An Efficient Signal Reconstruction Algorithm for Stepped Frequency MIMO-SAR in the Spotlight and Sliding Spotlight Modes," *International Journal of Antennas and Propagation*, 2014.

[95] A. Manikas, *Beamforming Sensor Signal Processing for Defence Applications*. London: Imperial College Presss, first ed., 2015.

[96] W. Q. Wang, "MIMO SAR imaging: Potential and challenges," *IEEE Aerospace and Electronic Systems Magazine*, 2013.